Metal-organic Nanosheets as Hole Transport Layer Additives for Enhancing Perovskite Solar Cells

Sanyou Xu

210169427

A thesis submitted to the University of Sheffield in partial fulfilment of the requirements for the Degree of Doctor of Philosophy

September 2025

The University of Sheffield

School of Mathematical and Physical Sciences

Abstract

Perovskite solar cells (PSCs) are at the forefront of next-generation photovoltaic research. However, achieving efficient, low-cost, and dopant-free hole transport layers (HTLs) remains a central challenge, especially when using poly(3-hexylthiophene) (P3HT), whose intrinsic charge mobility and energetic alignment constrain device performance. This thesis presents a systematic exploration of two-dimensional (2D) metal–organic nanosheets (MONs), ultrathin crystalline materials with high surface areas and tunable electronic properties as multifunctional additives within P3HT-based HTLs, establishing a rational design framework that bridges molecular structure with macroscopic photovoltaic performance.

Starting with porphyrin-derived Zn_2(ZnTCPP) MONs), their incorporation at a loading of 50 wt% relative to the P3HT mass led to a significant increase in power conversion efficiency (PCE) from 6.55±0.16 to 12.11±0.31%. Structural and spectroscopic characterizations revealed that these nanosheets enhanced lamellar ordering, improved π–π stacking and tuned the HOMO level to better match the perovskite absorber, thereby enabling efficient exciton dissociation and hole extraction.

Building on this platform, two additional porphyrinic systems—Cu_2(CuTCPP) and bimetallic Zn–Pd–TCPP—were developed. These systems exhibited altered electronic structures that facilitated more efficient hole extraction and reduced charge recombination, thereby improving long-range transport compared with pristine polymeric HTLs. This improvement in charge of transport consequently enhanced the device performance.

This study further incorporated intrinsically conductive 2D cMONs, specifically M–HHTP (M = Ni, Co, Cu) and M–HITP (M = Ni, Cu). Owing to their extended π–d conjugation, these frameworks are considered to possess intrinsic electrical

conductivity and enhanced charge delocalization. When hybridized with P3HT, the resulting composites exhibited improved molecular ordering and stronger interfacial interactions, among which Ni–HITP achieved a maximum power conversion efficiency (PCE) of 10.49%, ranking highest within the systems investigated in this work.

Acknowledgements

Reaching this stage after four years of study has not been easy. I am grateful for every ray of sunshine and every falling leaf in Sheffield, which have given me endless encouragement and strength, allowing me to cherish every moment of these four years. I would like to thank all those who have guided, supported, and accompanied me during this journey—not only in my research, but also in my daily life. Finally, I am deeply thankful to the University of Sheffield for granting me this great opportunity to complete my doctoral studies.

First and foremost, I would like to express my deepest gratitude to my supervisors, **Dr.**

Jonathan Foster and **Professor David Lidzey,** for their patience, invaluable guidance, and constant support throughout the course of my PhD. Their insight and encouragement, particularly during the formative first year, have been instrumental in shaping both my research and my development as an independent scientist.

I am equally grateful to the members of the **Foster group**—Dr. Ram Prasad R. R. Freya Cleasby, Michael Harris, Millie Wood, Benedict Smith, and Jiangtian Tan for their friendship, stimulating discussions, and support in both the laboratory and the office. When I leave, I also give huge thanks to Dr. Prioti Purba and Alana for their lovely help as well.

I also wish to thank all the members of Professor Lidzey's group. I am especially grateful to **Ibrahim A. Albariqi**, who patiently guided me through the procedures of solar cell fabrication and taught me how to carry out the relevant device characterization and performance testing. His expertise and encouragement were invaluable in helping me acquire both practical skills and confidence in experimental work. I would also like to thank **MirKazem Omrani** for his invaluable guidance on EQE measurements during the final stages of my research, which greatly improved the reliability and depth of my results. Finally, my heartfelt thanks go to **Timothy Thornber,** whose generous support, encouragement, and guidance extended far beyond the laboratory. His help has been indispensable, and I feel truly fortunate to have had his mentorship and friendship throughout this journey.

My sincere gratitude also goes to **Craig Robertson**, whose training and support in powder X-ray diffraction were essential in helping me to understand structural characterization and to reliably analyze my samples. I am equally thankful to **Deborah B. Hammond**, who provided invaluable guidance on ultraviolet photoelectron spectroscopy, patiently explaining both the experimental procedures and the interpretation of results, which proved critical for my energy-level studies. I also wish to acknowledge **Nik Reeves-McLaren** for his advice and assistance with Raman spectroscopy, whose expertise not only enabled me to conduct the measurements

successfully but also deepened my understanding of the structural and vibrational properties of the materials investigated in this thesis.

Finally, I would like to express my deepest gratitude to my parents for their unconditional love, encouragement, and sacrifices. Their unwavering support has been my greatest source of strength throughout this journey. Without their constant belief in me and their patience through all the challenges, this thesis would not have been possible. This achievement is as much theirs as it is mine.

Table of content

Section 1 – Introduction and aims

1.1 Global energy background and the imperative for renewable technologies

The unprecedented global demand for energy, propelled by sustained population growth, industrial expansion, and accelerating urbanization, exerts significant pressure on finite natural resources while intensifying environmental degradation. [1–3] Concurrently, anthropogenic greenhouse gas emissions—chiefly from fossil fuel combustion—are the

principal driver of climate change, with wide-ranging socio-economic and ecological consequences. [4,5] The energy sector alone accounts for approximately 73% of global GHG emissions, [6] making it the primary target for mitigation policies.

Among the renewable options, solar energy is particularly compelling due to its vast abundance—delivering an estimated 173,000 TW of power to the Earth's surface annually, far exceeding global energy consumption needs.[7,8] Moreover, its geographical ubiquity and declining levelized cost of electricity which fell by 85% for utility-scale PV between 2010 and 2022 [9]—position it as a cornerstone of the clean energy transition.

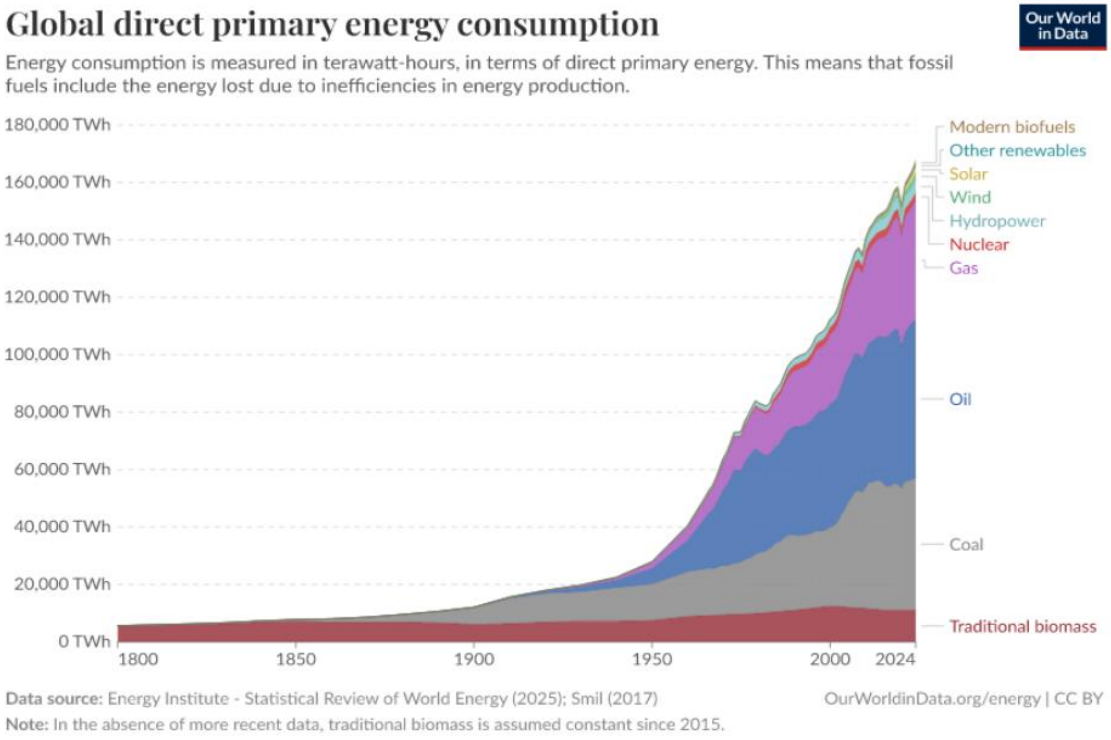

Figure 1.1 Global primary energy consumption by source (2000–2024), highlighting the growth of renewable energy. Data source: Our World in Data, based on International Energy Agency (IEA) statistics. [10]

1.2 Overview of solar cell technologies photovoltaic

Photovoltaic (PV) devices, which directly convert sunlight into electrical energy, have evolved through three broadly defined technological generations. [11] The first generation comprises crystalline silicon (c-Si) solar cells, which currently dominate over 90% of the PV market. [12] Monocrystalline c-Si modules have achieved commercial efficiencies

exceeding 25%,[13] with operational lifetimes surpassing 25 years. Despite these strengths, c-Si technology is approaching its theoretical Shockley–Queisser efficiency limit (~33%) [14] and relies on high-temperature, energy-intensive manufacturing processes that increase environmental and economic costs.[15]

The second generation includes thin-film technologies such as cadmium telluride (CdTe) and copper indium gallium selenide (CIGS), which reduce material usage and enable flexible form factors.[16,17] However, their adoption is constrained by the scarcity and/or toxicity of constituent elements (e.g., tellurium, indium, cadmium) and the complexities of achieving large-scale, defect-free deposition.[18,19]

The third generation encompasses emerging PV technologies aiming to overcome the efficiency–cost trade-off of earlier generations. This category includes dye-sensitized solar cells (DSSCs), organic photovoltaics (OPVs), quantum dot solar cells, and metal halide perovskite solar cells (PSCs).[20,21] These technologies offer the promise of low-temperature, solution-based fabrication, mechanical flexibility, and tunable optoelectronic properties. Among them, PSCs have attracted extraordinary research interest due to their unprecedented rate of efficiency improvement and compatibility with scalable processing methods.

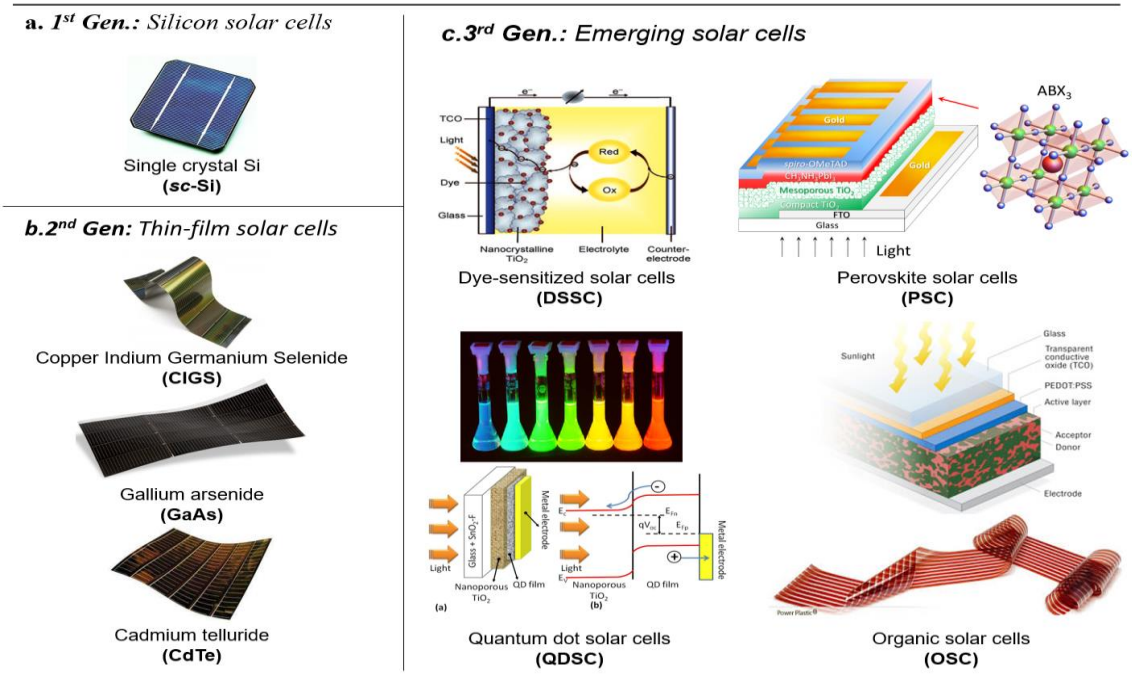

Figure 1.2 Schematic representation of the different solar cell technologies; a.1st generation silicon solar cell; b. 2nd generation thin solar cells; c.3rd generation solar cells.[22,23,24]

1.3 Rationale for focusing on perovskite solar cells

Since their first demonstration in 2009 with a PCE of just 3.8%,[25] PSCs have undergone a meteoric rise, reaching certified efficiencies of 26.1% in single-junction devices and 33.9% in tandem configurations with silicon by 2024.[26,27,28] This trajectory is unparalleled in PV history, driven by the remarkable optoelectronic properties of metal halide perovskites: High absorption coefficients (>10^5 cm^{-1})[29] enable thin active layers to harvest most incident light. Tunable direct bandgaps (1.2–2.3 eV) [30] facilitate spectral matching for tandem architectures. Long carrier diffusion lengths (>1 μm) [31] and low exciton binding energies (~10–50 meV) [32] support efficient charge separation. Defect tolerance mitigates non-radiative recombination losses.[33] Equally important, PSCs can be fabricated using low-cost, solution-based techniques such as spin-coating, blade-coating, slot-die coating, and inkjet printing. [34,35] These processes are compatible with flexible substrates and roll-to-roll manufacturing, offering a path toward high-throughput production. However, PSCs face persistent barriers to commercialization, including instability under moisture, oxygen, heat, and illumination; hysteresis effects; and challenges in scaling up while maintaining high efficiency. [36,37] Among these, interfacial engineering—particularly at the hole transport layer (HTL)is critical for improving both performance and stability.

1.4 Crystal structure and photophysical properties of perovskites

Metal halide perovskites typically adopt the general formula ABX_3, where the A-site is occupied by a monovalent cation, the B-site by a divalent metal cation, and the X-site by a halide anion (Figure 1.3). In high-performance photovoltaic compositions, A may be an organic cation such as methylammonium (MA^+, $CH_3NH_3^+$) or formamidine (FA^+, $CH(NH_2)_2^+$), or an inorganic cation such as Cs^+.[38] The B site is usually occupied

by Pb^{2+}, Sn^{2+}, or occasionally Ge^{2+}, located at the body center of the cubic lattice. The X sites, at the face centers, are generally halide anions such as Cl^{-}, Br^{-}, or I^{-}.[39]

The three-dimensional network formed by corner-sharing $[BX_6]^{4-}$ octahedra imparts strong light absorption, high carrier mobility, and long diffusion lengths. A large static dielectric constant and low exciton binding energy enable efficient exciton dissociation at room temperature, facilitating free-carrier generation upon photoexcitation.[40] For optimum solar harvesting, perovskites should possess direct bandgaps in the ideal range of 1.2–1.6 eV; for example, $MAPbI_3$ exhibits a direct bandgap around 1.55 eV.[41]

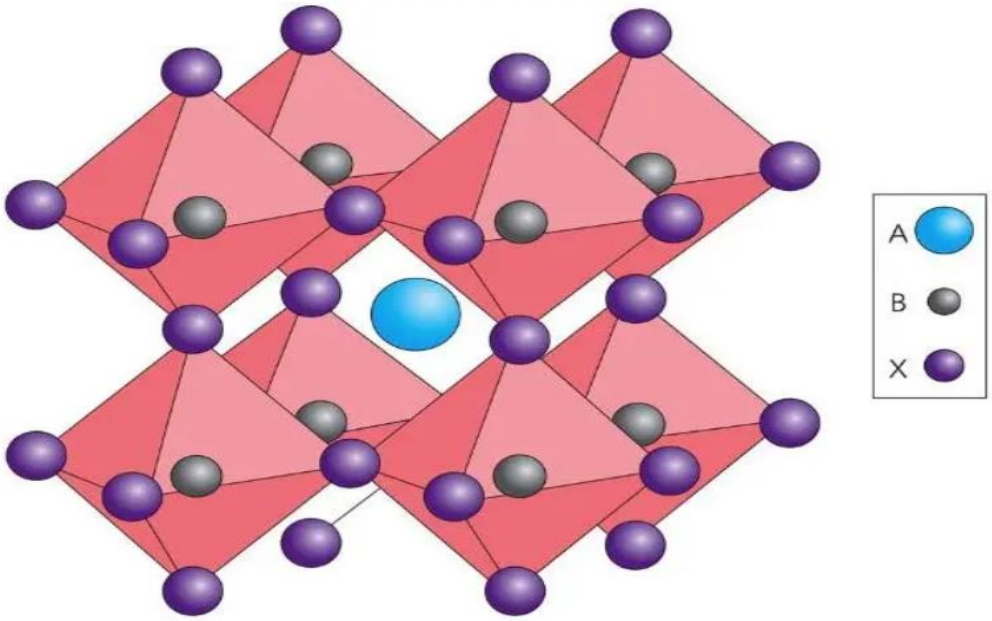

Figure 1.3 Crystal structure of an ABX_3 perovskite, where A is a monovalent cation, B is a divalent metal cation, and X is a halide anion.[42]

1.5 Fundamentals of perovskite solar cells structure and operation

PSCs are typically fabricated in either the n–i–p (ELT first) or p–i–n (HTL first) configuration.[43] In the widely adopted n–i–p planar architecture, the device stack comprises several functional layers, each playing a distinct role in determining overall performance.

At the front of the device lies the transparent conductive oxide (TCO), such as indium tin oxide (ITO) or fluorine-doped tin oxide (FTO), which provides both optical transparency and electrical conductivity, enabling efficient light transmission while serving as the anode contact.[44] This is followed by the electron transport layer (ETL), which selectively extracts photogenerated electrons while blocking holes. Common ETL materials include titanium dioxide (TiO_2), tin dioxide (SnO_2), and fullerene derivatives, chosen for their suitable energy-level alignment and high electron mobility.[41]

Next is the perovskite layer, which serves as the light-harvesting medium. Its composition and microstructure critically influence optoelectronic properties such as absorption coefficient, carrier lifetime, and defect density.[45] Upon photon absorption, electron–hole pairs are generated, which then dissociate into free carriers.

The HTL is physically positioned above the perovskite to facilitate selective hole extraction and block electrons. Typical HTL candidates include small-molecule semiconductors (e.g., spiro-OMeTAD), conjugated polymers (e.g., PTAA, P3HT), and inorganic materials (e.g., NiO_x, CuSCN), each offering distinct advantages in terms of stability, cost, and conductivity. [46,47]

Finally, the metal electrode, most commonly gold (Au) or silver (Ag) collects holes and completes the circuit. [48] The interplay between these layers determines the photovoltaic performance, with factors such as energy-level alignment, carrier mobility, defect passivation, and suppression of interfacial recombination being crucial for achieving high power conversion efficiency.

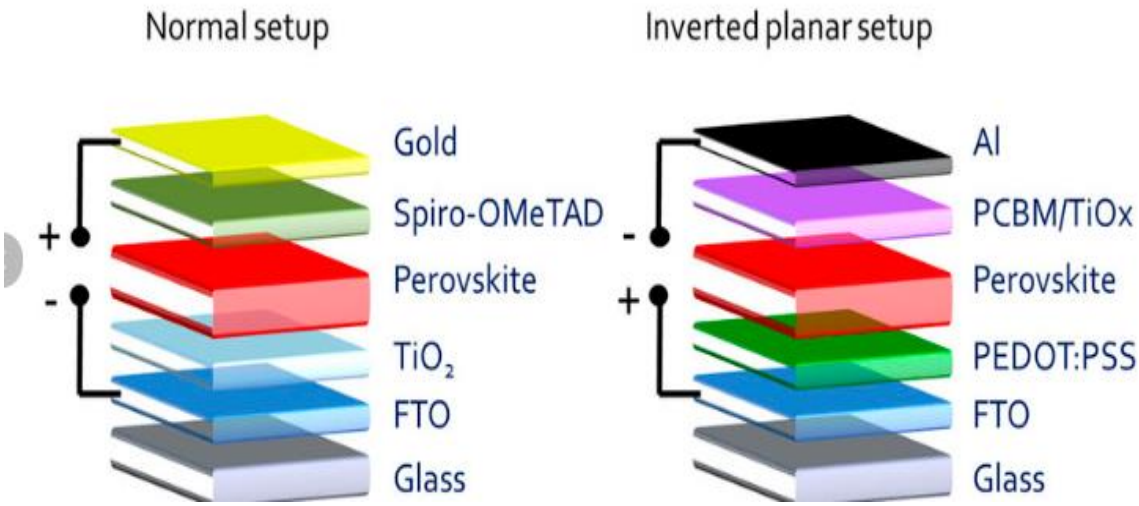

Figure 1.4 Structure of a normal or n-i-p PSC (left) and an inverted or p-i-n PSC (right).[49]

1.6 Challenges in Hole transport layers

The HTL plays a crucial role in PSC performance, influencing not only PCE but also stability and reproducibility. [50,51] Suboptimal Highest Occupied Molecular Orbital (HOMO) alignment between the HTL and perovskite valence band can create energy barriers, reducing open-circuit voltage (Voc) and fill factor (FF). [52] Furthermore, many widely used HTLs, such as spiro-OMeTAD and PTAA, require dopants (e.g., Li-TFSI, tBP) to improve conductivity, but these can exacerbate instability by promoting ion migration and moisture ingress. [53]

Poly(3-hexylthiophene) (P3HT) has been explored as a dopant-free alternative, offering better environmental stability and lower cost. [54] Its hydrophobic nature can enhance device moisture resistance. However, pristine P3HT suffers from relatively low hole mobility (~10^{-4}–10^{-3} cm^2 V^{-1} s^{-1}) and imperfect energy-level matching with perovskite absorbers, limiting device performance. [55] This has motivated research into HTL modification strategies, particularly the incorporation of nanostructured materials to enhance charge transport and tune interfacial energetics.

1.7 Working Principles of PSCs

Figure 1.5 schematically illustrates the fundamental working principle of PSCs. Their photovoltaic conversion can be broadly divided into three sequential stages: (i) photon absorption and exciton generation, (ii) charge separation and transport, and (iii) charge extraction and collection. [56]

At the initial stage, the perovskite absorber layer serves as the primary light-harvesting medium. Hybrid halide perovskites typically exhibit a direct bandgap of approximately 1.55 eV, which falls within the Shockley–Queisser optimal range (1.2–1.6 eV) for single-junction solar energy conversion. [57] In this work, we employ a mixed-cation mixed-halide perovskite system derived from $PbCl_2$, PbI_2, FAI, and CsI precursors, which enables effective bandgap(1.55eV) tuning and improved film quality through compositional engineering.

Under AM 1.5G illumination, incident photons with energies above the bandgap are absorbed to generate excitons. Unlike organic semiconductors, where exciton binding energies often exceed 0.3 eV, halide perovskites possess relatively low binding energies (10–50 meV), comparable to the thermal energy at room temperature ($k_BT \approx$ 25 meV). Consequently, photogenerated excitons readily dissociate into free carriers without requiring an additional driving force from heterojunction interfaces. [58]

Following exciton dissociation, charge transport occurs within the perovskite bulk. The favorable optoelectronic properties of perovskites—such as high absorption coefficients ($>10^5$ cm^{-1}), long carrier lifetimes (in the microsecond range), and diffusion lengths extending to micrometer scales—facilitate efficient carrier transport and collection even in thin absorber layers (~300–600 nm). Moreover, the so-called defect tolerance of perovskites, arising from their electronic band structure dominated by shallow defect states, minimizes non-radiative recombination and sustains high quasi-Fermi level splitting. [59]

Subsequently, selective charge transport layers direct electrons and holes toward their

respective electrodes. Electrons are injected into the ETL, commonly SnO_2 or TiO_2, which provides efficient electron extraction while blocking holes. In parallel, holes migrate through the HTL, which may include organic semiconductors (e.g., P3HT, Spiro-OMeTAD) or inorganic materials (e.g., NiO_x, CuSCN). The energy-level alignment at these interfaces is critical in minimizing energy losses and enhancing the open-circuit voltage. Interfacial engineering, such as doping and molecular passivation, is often required to suppress interfacial recombination. [60]

Finally, charge carriers are extracted at the electrodes: electrons are collected at the transparent conducting oxide (ITO or FTO), while holes are transferred to the metallic counter electrode (typically Au or Ag). These interfaces not only serve as collection sites but also influence device stability and hysteresis. For instance, ion migration and interfacial band bending can dynamically modulate extraction efficiency, thereby affecting long-term operational stability. Recent advances, including interfacial passive action and carbon-based electrodes, aim to mitigate such challenges. [61]

In summary, the superior performance of PSCs stems from the synergistic efficiency of light absorption, exciton dissociation, long-range carrier transport, and selective charge extraction. These mechanisms have enabled single-junction PSCs to reach certified power conversion efficiencies above 26% within little more than a decade of research, positioning them as a compelling alternative and complement to established silicon photovoltaics. [62]

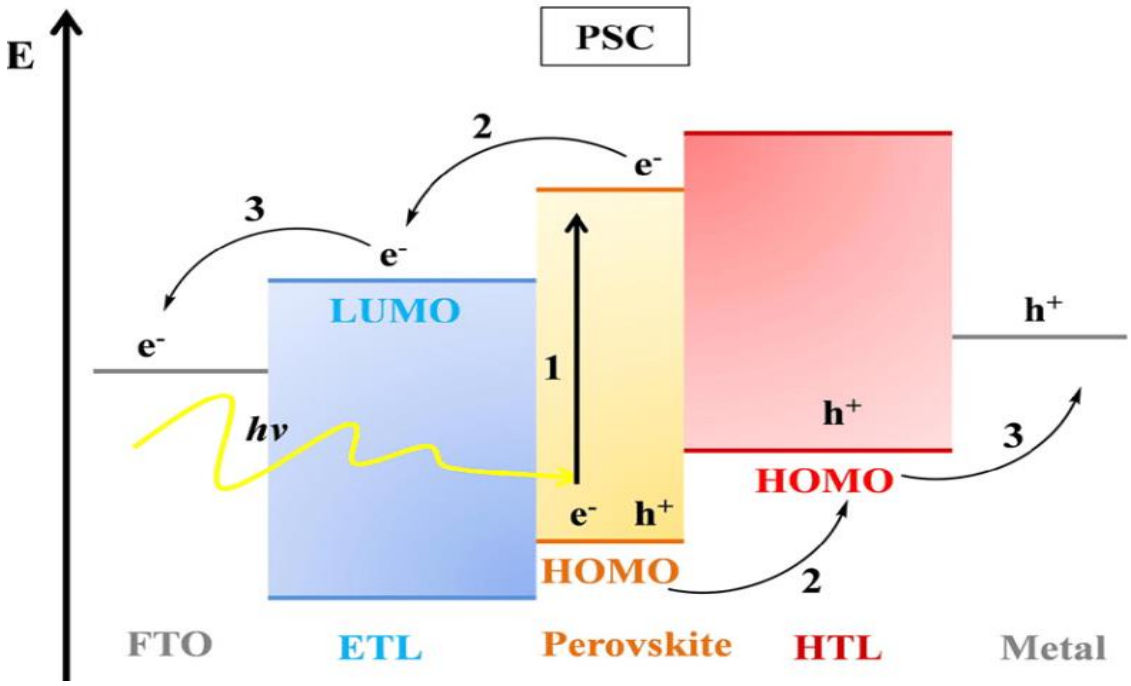

Figure 1.5 Working principle of PSCs

1.8 Parameters of perovskite solar cells

A photovoltaic device in the dark behaves analogously to a diode, and its current–voltage (J–V) relationship can be modelled using the Shockley ideal diode equation (Equation 1) together with the solar cell equivalent circuit.

$$J_D(V) = J_0\left[EXP\left(\frac{eV}{K_BT}\right) - 1\right] \quad \text{Equation 1}$$

Where

J_D = current through the diode,

J_0 = dark saturation current density,

e= elementary charge,

V = applied diode voltage,

K_B = Boltzmann constant,

T = absolute temperature of the device.

In PSCs, the dark saturation current density J_0 is strongly influenced by trap-assisted recombination and interfacial defects, which distinguishes them from traditional silicon diodes. [63]

1.8.1 Current–voltage characteristics

The J–V sweep under illumination is the primary method to evaluate PSC performance. The illuminated diode equation can be written as:

$$J(V) = J_0 \left[EXP\left(\frac{eV}{nK_BT}\right) - 1 \right] - Jsc \qquad \textbf{\textit{Equation 2}}$$

where n is the diode ideality factor. For PSCs, hysteresis effects arising from ion migration and ferroelectric-like polarization may distort J–V measurements, requiring stabilized power output tracking for accurate efficiency determination. [64]

1.8.2 Short-circuit current density (Jsc)

Jsc is defined as the photocurrent per unit area (mA cm^{-2}) when V = 0. It depends on optical absorption, carrier generation, and collection efficiency. Due to high absorption coefficients (>10^5 cm^{-1}) and long diffusion lengths, PSCs routinely achieve Jsc values above 24 mA cm^{-2}. However, parasitic absorption in transport layers and non-radiative recombination at grain boundaries may reduce Jsc. [65]

1.8.3 Open-circuit voltage (Voc)

Voc is the potential at which the net current is zero. In PSCs, Voc is determined by the quasi-Fermi level splitting in the perovskite absorber and is affected by energy-level alignment with charge transport layers and recombination losses. High-quality PSCs exhibit Voc values up to ~1.2 V for bandgaps around 1.55 eV, but typical losses of 0.3–0.4 V remain due to non-radiative pathways. [66]

1.8.4 Fill Factor (FF)

The fill factor measures the "squareness" of the J–V curve and is given by:

$$FF = \frac{J_{mp} * V_{mp}}{J_{sc} * V_{oc}} \qquad \textit{Equation 3}$$

where J_{mp} and V_{mp} are the current density and voltage at the maximum power point. In PSCs, FF values exceeding 80% are achievable with efficient charge transport layers and minimal hysteresis. High FF is often hindered by poor interface quality and unoptimized series/shunt resistances. [67]

1.8.5 Power conversion efficiency (PCE)

The PCE is the most important figure-of-merit, defined as:

$$\eta = \frac{V_{oc} * J_{sc} * FF}{P_{in}} \qquad \textit{Equation 4}$$

where P_{in} is the incident illumination power (typically 100 mW cm^{-2} under AM 1.5G). PSCs have achieved certified efficiencies above 26%, rivalling crystalline silicon. [68]

Section 2. Metal–organic nanosheets (MONs): emerging two-dimensional materials for photovoltaics

Despite the unprecedented progress of PSCs over the past decade, with PCEs now exceeding 26%, their further advancement remains constrained by interface-related losses and stability challenges. In particular, the HTL and its contact with the perovskite absorber represent a persistent bottleneck: conventional HTL materials such as spiro-OMeTAD and P3HT, while enabling high initial efficiencies, often suffer from poor

energy-level alignment, dopant dependence, and limited stability, resulting in significant VOC losses, restricted charge mobility, and accelerated environmental degradation. [69,70] This indicates that, even if the bulk perovskite layer possesses outstanding optoelectronic properties, unresolved interfacial issues continue to limit both device performance and operational lifetime.

To address this challenge, researchers have attempted to introduce a variety of two-dimensional (2D) materials for interfacial engineering.

Graphene and its derivatives, owing to their excellent conductivity (10^4–10^5 S cm^{-1} at room temperature) and chemical stability, have been employed to improve HTL conductivity and reduce series resistance. For example, Li et al. [71] demonstrated that incorporating graphene oxide (GO) as an interfacial additive in PSCs enhanced the fill factor by ~10% and increased the initial PCE by 2–3%. However, graphene's intrinsic zero bandgap prevents effective tuning of energy levels, leading to limited hole selectivity and sometimes higher recombination currents. [72] Furthermore, aggregation during solution processing often hampers uniform coverage, which is particularly problematic for large-area PSC modules.

Transition metal dichalcogenides (TMDs) such as MoS_2, WS_2, and WSe_2 have also been investigated, leveraging their layered structure and direct bandgaps (1–2 eV) to provide selective charge extraction. Studies have shown that MoS_2 nanosheet interlayers can suppress non-radiative recombination, thereby improving VOC by 40–60 mV. [73] Nonetheless, the relatively high defect density (e.g., sulfur vacancies) frequently introduces trap states that limit charge transport. [74] Moreover, the fabrication of TMDs still relies heavily on either mechanical exfoliation, which produces small flakes with low yield, or chemical vapor deposition (CVD), which requires high temperature (>600 °C) and vacuum conditions—both incompatible with the low-temperature solution processing typically used in PSC fabrication. Thus, while TMDs have demonstrated promising interfacial effects in laboratory settings, their scalability and reproducibility remain major obstacles to practical application.

Covalent organic frameworks (COFs), as a class of crystalline 2D polymers, have also attracted attention due to their modularity and tunable optoelectronic properties. By rationally designing organic linkers, COFs can in principle offer adjustable frontier orbital levels, with reported HOMO values tunable between –5.0 and –5.4 eV, close to the valence band of perovskites. [75] However, most COFs suffer from poor crystallinity, low charge carrier mobilities (10^{-7}–10^{-5} cm^2 V^{-1} s^{-1}), and difficulties in obtaining stable few-layer nanosheets by liquid exfoliation. As a result, although COFs possess attractive chemical designability, their limited charge transport and uncertain processing compatibility hinder their broader adoption in PSCs.

Taking together, these classes of 2D materials each demonstrate unique advantages in conductivity and stability, TMDs in bandgap-derived selectivity, and COFs in molecular design flexibility. Yet, their inability to simultaneously achieve tunable energetic, scalable processability, and long-term stability has prevented them from delivering comprehensive and sustainable improvements in PSC interfaces. This situation highlights the need for alternative 2D platforms capable of addressing multiple interfacial challenges in a unified manner.

Against this backdrop, MONs have recently emerged as a promising direction for PSC interfacial engineering. Structurally derived from layered metal–organic frameworks, MONs combines molecular-level programmability with the intrinsic advantages of 2D layered morphologies. Unlike traditional inorganic 2D materials, MONs offers several distinctive benefits. First, their tunable electronic structure allows precise adjustment of HOMO/ Lowest Unoccupied Molecular Orbital (LUMO) levels via the choice of metal centers and organic ligands, enabling better energy-level alignment with perovskite absorbers. [76,77] Second, MONs exhibits excellent processability, being dispersible in solution and compatible with low-temperature deposition techniques such as spin coating or inkjet printing, which are essential for scalable PSC fabrication.[72] Third, the structural templating effect of MONs, arising from their periodic frameworks and π–π interactions, can induce favorable perovskite grain orientation, thereby

reducing grain boundary defects. [78] Fourth, their surfaces provide abundant coordination sites that can chemically interact with under-coordinated ions at the perovskite surface, enabling defect passivation and improved device stability. [79] Finally, MONs stands out for their multi-functionality: within a single material system, they can simultaneously achieve energy-level alignment, morphological control, and defect passive action.

As such, MONs is not merely complementary to existing 2D materials but represent a fundamentally distinct platform with "all-in-one" functionality. By integrating energy-level engineering, morphological templating, and interfacial stabilization within a single framework, MONs offers a new pathway to overcome the persistent interfacial bottlenecks in PSCs, thereby enabling the synergistic improvement of both efficiency and long-term stability.

2.1 Definition and structural features of MONs

Ultrathin two-dimensional nanosheets exhibit unique structural and physical characteristics that arise from their confined dimensionality. Monolayer or few-layer nanosheets typically lack significant interlayer interactions, which results in electron confinement within two dimensions and leads to compelling electronic properties such as size-dependent band structures and enhanced charge mobility. [80] Furthermore, owing to their atomic- or near-atomic thickness, such nanosheets possess exceptional mechanical flexibility and optical transparency, features that make them particularly attractive for incorporation into next-generation flexible optoelectronic devices, including OSCs and PSCs. Finally, their large lateral dimensions coupled with ultrathin thicknesses endow them with an extremely high specific surface area, rendering them especially suitable for interfacial and surface-active applications, such as charge extraction, defect passive action, or catalytic processes. [81]

Building on these advantages, a new class of ultrathin 2D materials has been developed that combines the structural diversity of metal–organic frameworks (MOFs) with the

morphological features of nanosheets, namely metal–organic nanosheets (MONs). MONs inherits the reticular chemistry of MOFs, being composed of metal nodes interconnected by organic ligands, but differ fundamentally in their dimensionality and anisotropy. Whereas conventional three-dimensional MOFs extend isotropically in all directions, MONs is characterized by strong in-plane coordination bonding and only weak out-of-plane interactions (hydrogen bonding, π–π stacking or van der Waals forces). [76] This structural anisotropy renders MONs readily exfoliable into ultrathin layers via external forces such as ultrasonication, mechanical shearing, or chemical delamination, thereby exposing more active sites and enhancing interfacial accessibility. [82,83]

The choice of organic ligands and secondary building units (SBUs) plays a decisive role in the formation of MONs. Polycarboxylates are among the most widely used ligands because of their strong directional coordination ability and commercial availability. [84] The archetypal SBU is the paddlewheel unit, which consists of two metal cations bridged by four carboxylate ligands in a square-planar configuration. This geometry naturally propagates into 2D planar sheets with axial positions that can accommodate additional ligands, thus facilitating the construction of extended nanosheet frameworks. [85] Beyond carboxylates, a wide range of ligands—such as azolates, porphyrins, and heteroaromatic systems—have also been employed to impart specific electronic or chemical functionalities. [86,87]

From a broader perspective, MONs combines the intrinsic advantages of 2D morphology with the molecular programmability of MOFs. Their nanosheet geometry ensures high aspect ratios, dispersibility in solution, and compatibility with low-temperature thin-film processing. Simultaneously, their tunable chemistry allows precise control over energy-level alignment, frontier orbital positions (HOMO/LUMO), and surface polarity. [88,89] These combined features make MONs not merely derivatives of MOFs but a distinct class of hybrid 2D materials that merge crystallographic order, functional versatility, and interfacial advantages into one integrated platform.[90]

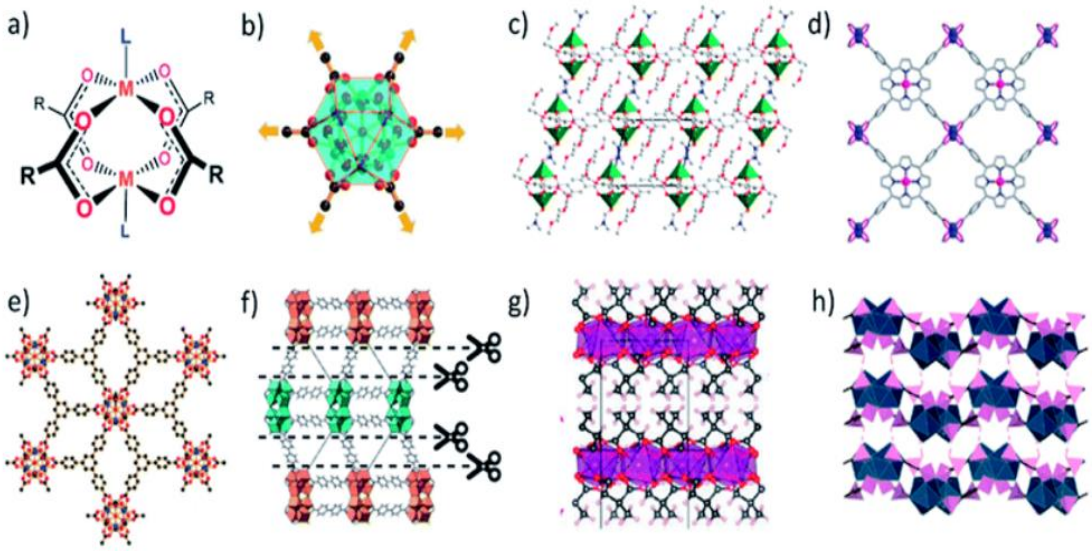

Figure 1.6 typical structure of Mons. a. PW structure of MONs. b. M6L6 secondary building units. c-h. example crystal structures showing diversity of carboxylic acid-based linkers and secondary building units. (Ashworth and Foster 2018) [91]

2.2 Structural design principles of MONs

The rational design of MONs is intrinsically linked to the tunability of their building blocks. Unlike conventional inorganic 2D materials, the modular architecture of MONs provides a powerful toolkit for tailoring electronic, chemical, and morphological properties at the molecular scale. The primary levers of design are the choice of metal centers, organic ligands, SBUs, and subsequent post-synthetic modification strategies.

The selection of metal ions dictates not only the coordination geometry but also the electronic properties of MONs. Transition metals such as Ni^{2+}, Cu^{2+}, and Co^{2+} often give rise to electrically conductive nanosheets due to partially filled d-orbitals that enable charge delocalization through metal–ligand interactions. [92,93] For instance, $Ni_3(HITP)_2$ has been reported to exhibit conductivities from ~2 up to ~40 S cm^{-1} depending on its form and structure, while $Cu_3(HHTP)_2$ shows in-plane conductivities on the order of 0.1–0.3 S cm^{-1} in thin-film measurements. These values suggest that such nanosheets are promising candidates for hole transport in photovoltaic devices. [88,89] In contrast,

Zn^{2+} or Mg^{2+} based MONs, while typically insulating, provide favorable band alignment and chemical stability, making them attractive as interfacial passivation layers.[94] By varying the oxidation state and ionic radius of the metal center, one can finely modulate the HOMO/LUMO positions of MONs, thereby optimizing energy-level matching with perovskite absorbers.

The ligand framework plays an equally crucial role in defining the electronic structure and surface chemistry of MONs. π-conjugated ligands such as hexa-hydroxytriphenylene (HHTP), hexaiminotriphenylene (HITP), porphyrins, and phthalocyanines promote extended charge delocalization across the nanosheet, leading to enhanced in-plane carrier mobility (Figure 1.7). [95,96] Moreover, chemical functionalization of ligands offers a straightforward means of tuning frontier orbital levels: electron-donating substituents (e.g., –OMe, $–NH_2$) can raise HOMO energies, while electron-withdrawing groups (e.g., $–NO_2$, –CN) lower them, thus enabling energy-level engineering to match the perovskite valence band. [97]

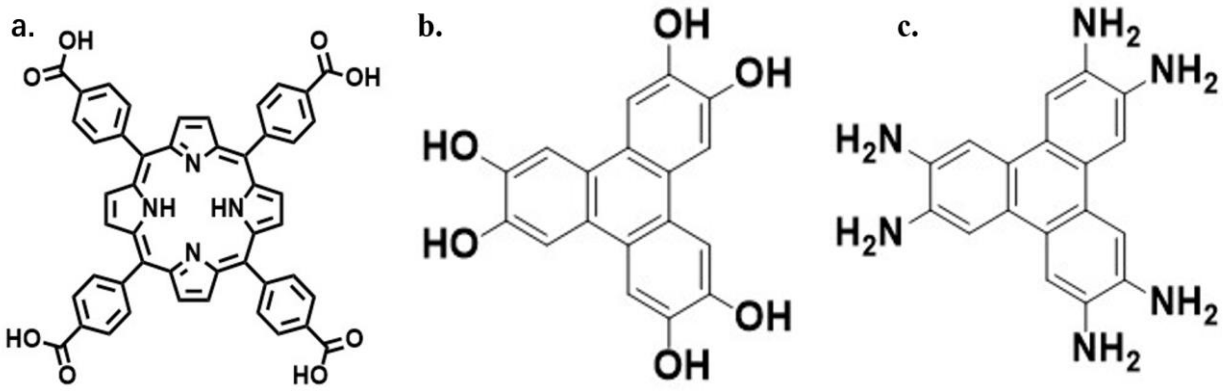

Figure 1.7 Structure of a.TCPP, b.HHTP and c. HITP

Beyond electronic tuning, ligands can impart surface polarity and hydrophilicity/hydrophobicity, which directly influence film morphology and compatibility with solution processing. [98]

The geometric arrangement of SBUs governs the overall topology of MONs. The

paddlewheel SBU, composed of two metal centers bridged by four carboxylates, remains the most widely employed motif due to its ability to generate planar, extended 2D sheets. [99] Alternative SBUs, such as triangular or square-planar motifs derived from azelates and porphyrins, expand the design space, enabling nanosheets with tailored pore sizes and electronic anisotropy. [100] Control over SBU symmetry is particularly important in applications requiring oriented charge transport or selective ion diffusion.

Post-synthetic modifications. In addition to design at the assembly stage, MONs can be further functionalized through post-synthetic modification (PSM). Strategies include covalent grafting of functional moieties, metal-ion exchange, or coordination of guest molecules.[101] Such modifications enable fine-tuning of energy-level alignment, defect passivation, and interfacial wettability, which are critical for enhancing the stability and efficiency of PSCs. [102] For example, incorporation of electron-rich amine groups at MON surfaces has been shown to improve interfacial hole extraction and suppress trap-assisted recombination. [103]

Taken together, these design strategies highlight the multidimensional tunability of MONs. By rationally selecting metals, ligands, and SBUs, and by applying targeted PSM, it becomes possible to engineer nanosheets with specific functionalities, ranging from conductivity enhancement to defect passivation. This rational design framework is what distinguishes MONs from other 2D materials and positions them as highly adaptable candidates for interfacial engineering in PSCs.

2.3 Synthetic strategies for MONs

Top-Down and Bottom-Up are the two commonly used methods for synthesizing 2D MONs. Top-Down involves splitting (i.e., Ultrasound, Mechanical exfoliation) the layered MOFs the Bottom-Up is generally used to synthesize 2D MONs in one step. The top-down approach is simple because the use of ultrasound or vibration is sufficient to break down the weak interlayer interactions in MOFs. [104] Unlike the top-down method, the Bottom-up approach generally uses metal ions and organic ligands to

synthesize 2D MONs directly but requires a different approach to limit the growth of MOF to get different thickness 2D MONs.

3D MOFs are connected by very strong coordination bonds within a single planar layer, but different layers are generally connected by van der Waals forces or hydrogen bonds. [105] This weak interlayer interaction can be easily overcome by the Top-Down method, which leads to the exfoliation of layered MOFs to form 2D MONs. Liquid exfoliation by ultrasonic treatment is the most widely used method for MOF stripping. The ultrasonic treatment process breaks the intra-layer as well as inter-layer bonding, leading to smaller grain fragments, resulting in a wider particle size distribution and smaller MON size than the Bottom-Up morphology.

Mechanical exfoliation is another Top-Down method by which Cu(μ-pym$_2$S$_2$) (μCl)-nH_2O 2D MONs can be prepared. The size of the MONs can be controlled by soaking in water for different times. Usually, ultra-thin MONs with a thickness of about 2 nm can be obtained when the soaking time is 4 days. [106]

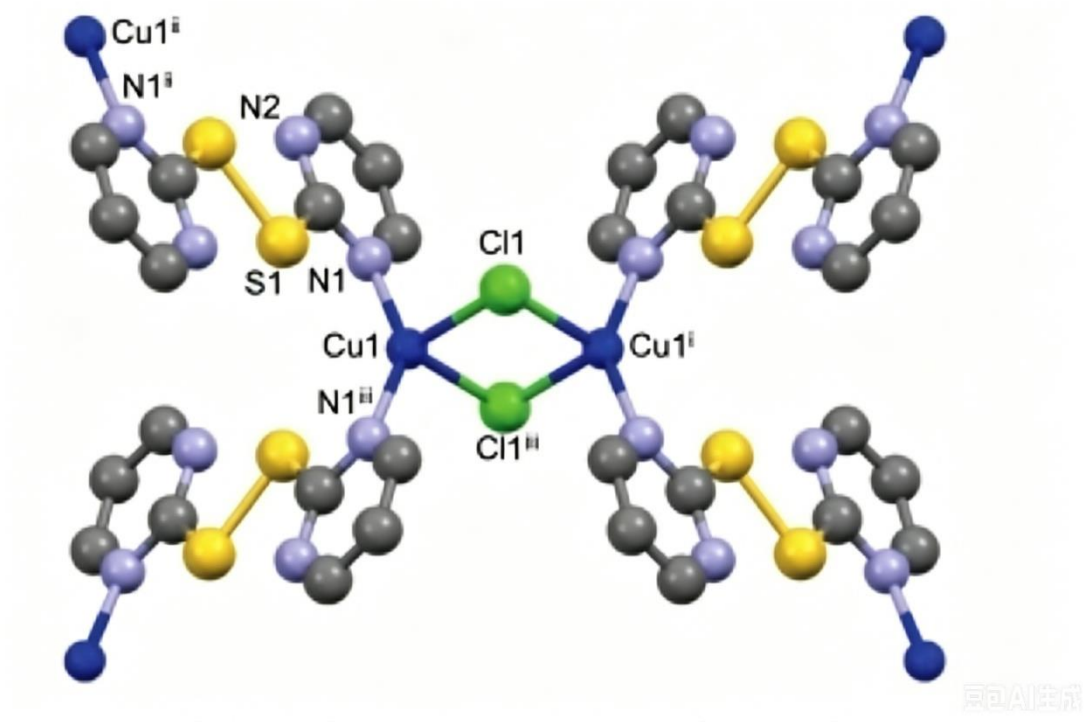

Figure 1.8 Structure of Cu(μ-pym$_2$S$_2$) (μCl)-nH_2O[106]

Another method is “freeze-thaw”. In this exfoliation process, the layered MOF is first dispersed in a solvent. In general, these solutions containing MOF will be frozen in liquid nitrogen (-196℃) and then thawed in hot water (80℃). The shear forces generated during the volume change of the solvent between the solid and liquid states are applied to the suspended 3D MOF crystals, causing them to exfoliate into separate nanosheets.[102]Unfortunately, Top-Down method is not suitable for the preparation of 2D MONs in homogeneous and high yields (typically obtained yields <15%). [107]

The use of interfacial effects to limit the growth of MOF nanosheets is the first Bottom-up method. In this method, the synthesis process occurs at the solvent interface surface to ensure good control of MOF growth. For example, Co-TCPP MONs were successfully synthesized by dispersing TCPP and Co^{2+} in chloroform/methanol as another interface using an aqueous solution of $CuCl_2$-$2H_2O$ as an interface. The formed 2D MOFs were then deposited on Si substrates and stacked by layer-by-layer growth method to produce 2D MONs of any thickness. [108]

Since interfacial synthesis occurs at the interfacial surface, the yield of the resulting 2D MONs is highly dependent on the area of the interfacial surface. Therefore, large-scale synthesis of MONs using this method has major limitations. The second method uses a simple surfactant-assisted synthesis method.

The surfactant limited the stacking of MOF along the vertical direction and helped to disperse the synthesized MOF nanosheets. 7.6±2.6 nm thick Zn-TCPP MONS were successfully synthesized using PVP surfactant. [109]

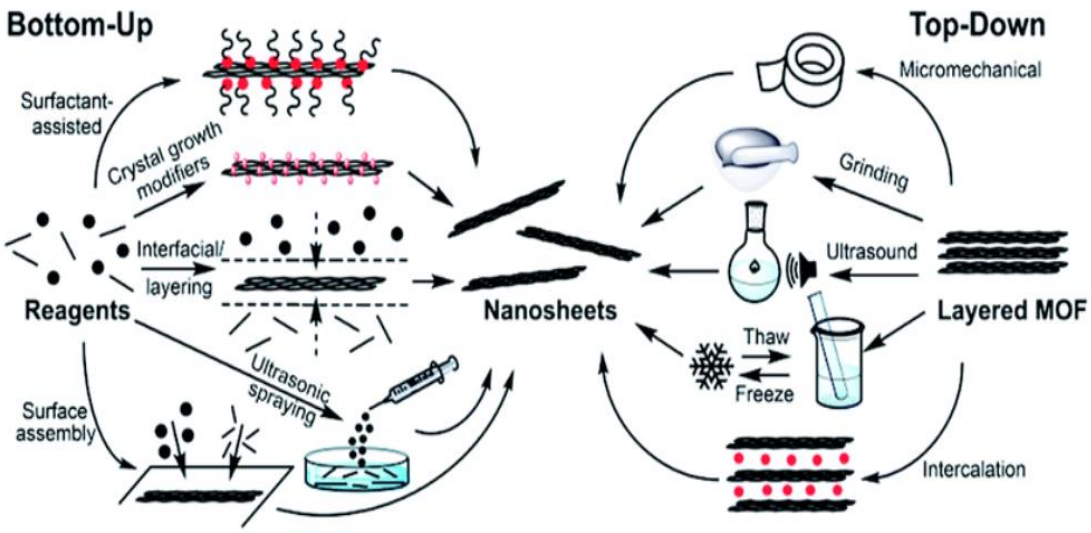

Figure 1.9 Scheme showing different Bottom-Up and top-down methodologies used to produce MONs. (Ashworth and Foster 2018) [86]

Section 3. MONs used in photovoltaics

The use of MONs in photovoltaic devices has gained momentum in recent years, driven by the demand for interfacial and active materials that combine high charge carrier mobility, tunable band structures, and compatibility with low-temperature solution processing. In organic and PSCs alike, interfacial engineering plays a decisive role in determining charge extraction efficiency and operational stability. While conventional

two-dimensional materials such as graphene or TMDs exhibit excellent conductivity and optoelectronic properties, their limited band tunability, difficulties in thickness control, and challenges in scalable production restrict their broader deployment. [106] In this context, MONs emerges as attractive alternatives, offering the structural programmability of MOFs while maintaining the advantageous features of 2D layered materials.

3.1 MONs used in solar cells as electrode

Transparent conductive electrodes are indispensable in both OSCs and PSCs, where they must simultaneously ensure high conductivity, optical transparency, and mechanical flexibility. Traditionally, indium tin oxide (ITO) has dominated this role, but its brittleness, scarcity of indium, and incompatibility with flexible substrates have prompted extensive searches for alternatives. Materials such as carbon nanotubes, silver nanowires, conductive polymers, and graphene have all been explored.[110]

Recently, a highly conductive MON—copper bis(dithiolene) (Cu-BHT, $[Cu_3(C_6S_6)]n$)—was introduced as a potential ITO replacement. Thin Cu-BHT films (20 nm) exhibited conductivity as high as 2500 S cm^{-1} with optical transparency up to 82%, comparable to commercial ITO glass. [111] When incorporated into three types of photovoltaic devices—PSCs, quantum dot solar cells (QDSCs), and polymer-based bulk heterojunction (BHJ) OPVs—the Cu-BHT electrode delivered device performances nearly identical to ITO-based counterparts (Table 1). For instance, PSCs fabricated with Cu-BHT electrodes achieved a PCE of 14.13±1.24%, virtually indistinguishable from 14.26±0.87% for ITO. This party demonstrates that MON-based electrodes can not only match the electrical and optical benchmarks of ITO but also offer superior mechanical flexibility and structural tunability, which are advantageous for next-generation flexible photovoltaics.

Nevertheless, scalability and long-term stability under operational stress remain unresolved. Future work must address whether MON-based electrodes can retain high

conductivity and transparency under bending, thermal cycling, and exposure to humid environments.

Table 1. Performance of photovoltaic equipment

Type	Substrate	V_{oc}(V)	J_{sc} (mA/cm^2)	FF (%)	PCE (%)
PSC	ITO	0.989±0.015	20.33±0.45	70.9±1.2	14.26±0.87
	Cu-BHT	0.985±0.023	20.47±0.65	70.1±2.4	14.13±1.24
QDs solar cells	ITO	0.581±0.005	23.47±0.32	60.8±1.1	8.29 ±0.25
	Cu-BHT	0.591±0.019	23.87±0.63	58.5±0.8	8.25 ±0.46
PTB7: PCBM solar cells	ITO	0.737±0.009	14.96±0.51	67.0±0.9	7.39±0.43
	Cu-BHT	0.744±0.021	15.02±0.95	65.8±1.8	7.35±0.35

3.2 MONs used in solar cells in active layer

Beyond electrodes, MONs has also been investigated as active materials or additives in the light-absorbing layer. Early studies employed porphyrin-based MON thin films on C_{60}-impregnated ITO substrates to fabricate liquid-junction solar cells, though the resulting PCEs were below 0.1%.[109] Despite the extremely low efficiencies, these attempts were significant in demonstrating the feasibility of using 2D coordination nanosheets in active optoelectronic layers.

Building on this, Sasitharan and co-workers incorporated the same porphyrin-based MONs into bulk heterojunction OPVs as active components. [112] More promising results were achieved by introducing Zn_2(ZnTCPP) MONs into P3HT: PCBM blends. Due to

their bandgap of ~1.8 eV, which complements the 2.0 eV gap of P3HT:PCBM, Zn_2(ZnTCPP) MONs facilitated improved molecular ordering of both polymer and fullerene domains. Morphological studies confirmed that MON doping suppressed phase overgrowth, yielding more favorable nanoscale morphology. Devices with 20 wt% MONs achieved PCEs of 5.2%, nearly double that of pristine control (2.67%). [113]The underlying mechanism can be attributed to the templating role of nanosheets. P3HT, being a semi-crystalline polymer, exhibited an increased crystalline fraction in the presence of MONs. The nanosheets act as structural templates that promote ordered π–π stacking and enhance the crystallization of P3HT chains, thereby improving charge percolation pathways and hole mobility. In addition, the incorporation of MONs suppresses excessive phase aggregation and enhances optical absorption, jointly contributing to the observed improvement in photovoltaic performance.

Although the absolute efficiencies remain low relative to state-of-the-art OPVs, these findings provide a proof-of-concept that MONs can modulate the nanoscale morphology of donor–acceptor blends and improve charge separation. This suggests that MONs could serve as multifunctional additives that simultaneously contribute to light absorption, morphology regulation, and interfacial passivation.

Subsequent studies extended this concept to more advanced semi-crystalline polymer systems. Sasitharan et al.[114] demonstrated that porphyrin-based MONs can act as highly effective templating agents in PffBT4T2OD:PCBM blends, where they promoted a higher fraction of *face-on* polymer crystallites, enhanced π–π stacking coherence, and optimized domain size distribution. As a result, devices incorporating MONs achieved efficiencies up to 12.3%, one of the highest values reported for fullerene-based OPVs at the time. This work provided compelling evidence that MONs are not only passive fillers but can actively direct molecular ordering and charge transport pathways, thereby broadening their potential applications in next-generation photovoltaic architectures.

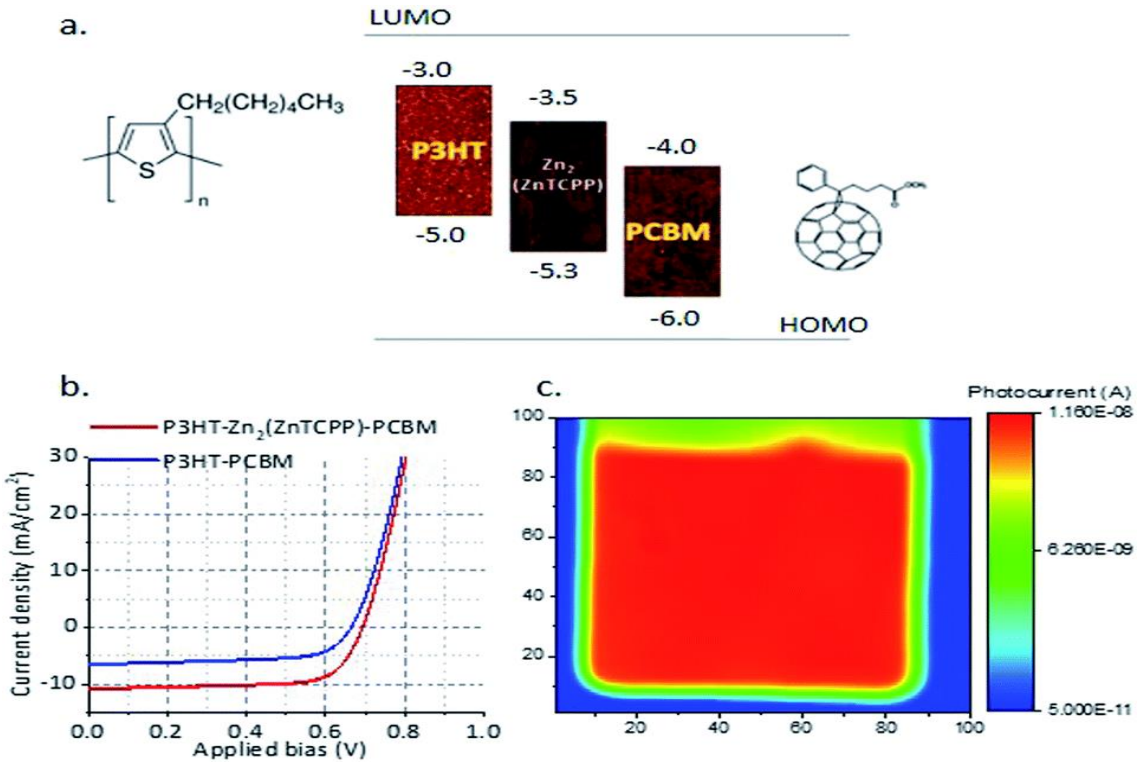

Figure 1.9 Device performance. a. energy level of Ternary system. b, JV curve of devices with/without MONs. C. high resolution LBIC mapping of the P3HT–MON–PCBM devices.[113]

3.3 MONs as addictive materials in ETL

ETL is another critical interface in PSCs, where stability and ion migration are major concerns. Leakage of Pb^{2+} and halide ions from the perovskite absorber into adjacent layers accelerates device degradation. To address this, Zhu and co-workers designed Zr-based MONs (ZrL_3) as ETL additives. [114] Owing to the selective coordination of Zr(IV) with carboxylate ligands, ZrL_3 nanosheets exhibited electron mobilities of 2.81 $\times 10^{-7}$ m^2 V^{-1} s^{-1} and efficient hole-blocking capabilities.

In PSC devices, incorporation of ZrL_3 MONs at the perovskite/ETL interface led to marked performance gains.FF improved from 71.21±1.333% to 76.42±1.150%, while PCE increased from 18.80±0.556% to 20.34±0.585%. The improved performance was attributed to enhanced electron extraction, reduced recombination at the interface, and effective suppression of ion leakage. Importantly, the devices with ZrL_3 layers retained

their performance over extended operation, highlighting the stabilizing role of MON-based ETL modifiers.

These findings confirm that MONs can serve not only as active or electrode materials but also as functional interfacial regulators, with a unique ability to combine electron transport with chemical stabilization of sensitive perovskite surfaces.

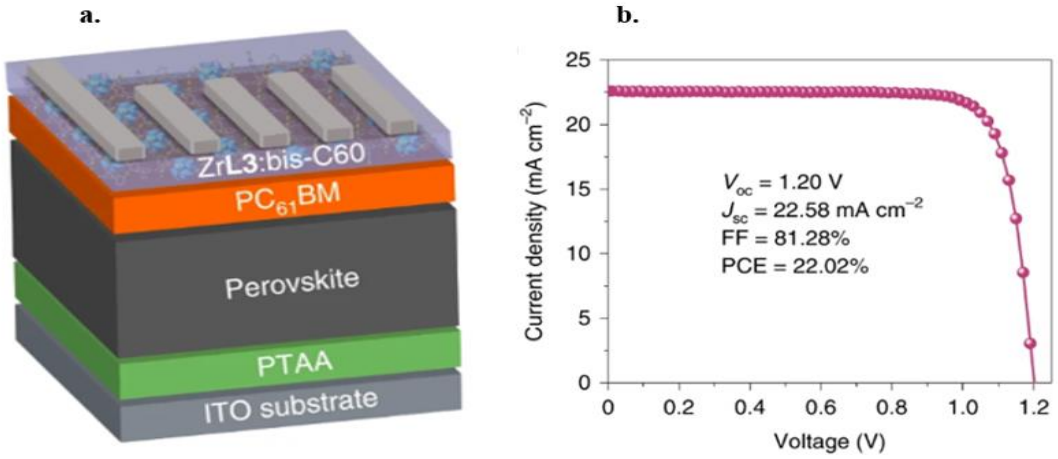

Figure 1.10 a. structure of the PSC. b. performance of the PSC.[114]

The PSCs with MONs as ETL showed higher performance (76.42% FF and 20.34% PCE) while without ZrL_3, the devices had only 71.21% FF and 18.80% PCE. This demonstrates that ZrL3 MONs can enhance the electron extraction and hole blocking ability of PSCs.

Section 4 Thesis aims

The existing literature demonstrates an increasing interest in incorporating MONs into PSCs. The introduction of ultrathin and tunable MONs into PSCs provides an opportunity to study their structural, optical, and electronic contributions in greater depth. Attention needs to be paid to how molecular packing, surface morphology, and

energy-level alignment of MONs affect charge extraction and recombination. Moreover, variations in synthetic routes and processing conditions can significantly alter the thickness, crystallinity, and interfacial compatibility of MONs. Understanding these differences is therefore essential for their reliable implementation in photovoltaic devices.

The specific aims of this thesis are as follows:

1. To explore, for the first time, the incorporation of metal–organic nanosheets (MONs) as additives in hole transport layers (HTLs) for perovskite solar cells (PSCs), and to establish their potential for enhancing device performance. (Chapter 2–6)

2. To investigate the structural and optical properties of Zn_2(ZnTCPP) MONs incorporated into P3HT-based HTLs, with particular focus on optical absorption, exciton quenching, and energy-level coupling. (Chapter 3)

3. To systematically compare how different metal centers (Cu and Zn–Pd) in MONs regulate the film morphology, crystallinity, and molecular packing of P3HT HTLs, and to elucidate the structure–property relationships governing charge transport performance. (Chapter 4)

4. To explore the application of conductive two-dimensional metal–organic nanosheets (2D cMONs) in P3HT thin films, and to evaluate their advantages in improving hole mobility, interfacial energy-level alignment, and suppression of charge recombination. (Chapter 5)

Chapter 2 introduces the main characterization techniques employed in this work, including X-ray diffraction (XRD), ultraviolet–visible absorption spectroscopy (UV–Vis), photoluminescence (PL), grazing-incidence wide-angle X-ray scattering (GIWAXS), current–voltage (J–V) analysis, and external quantum efficiency (EQE). By outlining the principles and applications of these methods, this chapter provides the

theoretical foundation for the subsequent experimental studies.

Chapter 3 investigates the structural and optical properties of Zn_2(ZnTCPP) MONs incorporated into P3HT thin films used as HTLs within P3HT based PSCs. Changes in optical absorption, exciton quenching, and energy-level coupling were investigated. By combining morphological and electronic characterization, this chapter explores how Zn_2(ZnTCPP) improves the film quality and charge transport capability of P3HT.

Chapter 4 extends this approach by varying the metal center, synthesizing Cu_2(CuTCPP) and Zn–Pd-TCPP MONs and incorporating them into P3HT HTLs. Using atomic force microscopy (AFM), scanning electron microscopy (SEM), and GIWAXS, this chapter systematically compares how different metal centers regulate film morphology, crystallinity, and molecular packing. The results reveal structure–property relationships that highlight the dependence of charge transport performance on the choice of metal center.

Chapter 5 explores the application of conductive two-dimensional metal–organic nanosheets (2D cMONs) in P3HT thin films. In comparison to conventional MONs, cMONs provide more efficient transport channels and lower energetic barriers. Through ultraviolet photoelectron spectroscopy (UPS) and electrical performance measurements, this chapter analyses their potential advantages in improving hole mobility, interfacial energy-level alignment, and suppression of charge recombination. This work offers a new perspective on introducing conductive 2D materials into organic–perovskite hybrid systems.

Finally, Chapter 6 concludes this work by summarizing the key outcomes and recommending future directions for research.

References

1. World Economic Forum, *Fostering Effective Energy Transition 2025*, World Economic Forum, Geneva, 2025.
2. World Nuclear Association, *World Energy Needs and Nuclear Power*, World Nuclear Association, London, 2025.
3. Exploiting Natural Resources, *Exploration of Natural Resources*, The Stimson Center, Washington, 2009.

4. Intergovernmental Panel on Climate Change (IPCC), *Climate Change 2021: The Physical Science Basis – Contribution of Working Group I to the Sixth Assessment Report of the IPCC*, Cambridge University Press, Cambridge, UK, 2021, ch. 6.
5. Intergovernmental Panel on Climate Change (IPCC), *Climate Change 2022: Impacts, Adaptation and Vulnerability – Contribution of Working Group II to the Sixth Assessment Report of the IPCC*, Cambridge University Press, Cambridge, UK, 2022, Summary for Policymakers.
6. International Energy Agency, *Greenhouse Gas Emissions from Energy Data Explorer*, International Energy Agency, Paris, 2024.
7. W. Taylor, *Shining Brightly*, MIT Energy Initiative, Massachusetts Institute of Technology, Cambridge, MA, USA, 2011.
8. Center for Sustainable Systems, University of Michigan, *Solar Photovoltaic Energy Factsheet (CSS15-15)*, Ann Arbor, MI, USA, 2024.
9. International Renewable Energy Agency, *Renewable Power Generation Costs in 2022*, International Renewable Energy Agency, Abu Dhabi, 2023.
10. International Energy Agency, *World Energy Balances 2024*, International Energy Agency, Paris, 2024.
11. M. A. Green, *Prog. Photovolt: Res. Appl.*, 2001, 9, 123–135.
12. International Energy Agency, *Trends in Photovoltaic Applications 2024*, IEA PVPS, Paris, 2024.
13. International Energy Agency, *Trends in Photovoltaic Applications 2024*, IEA PVPS, Paris, 2024
14. W. Shockley and H. J. Queisser, *J. Appl. Phys.*, 1961, 32, 510–519.
15. V. M. Fthenakis and H. C. Kim, *Prog. Photovolt. Res. Appl.*, 2011, 19, 144–152.
16. A. Romeo, A. Terheggen, D. Abou-Ras, D. L. Bätzner, F.-J. Haug, M. Kälin, D. Rudmann and A. N. Tiwari, *Prog. Photovolt. Res. Appl.*, 2004, 12, 93–111.
17. J. Britt and C. Ferekides, *Appl. Phys. Lett.*, 1993, 62, 2851–2852.
18. V. M. Fthenakis, *Renew. Sust. Energy Rev.*, 2009, 13, 2746–2750.

19. J. Poortmans and V. Arkhipov (eds.), *Thin Film Solar Cells: Fabrication, Characterization and Applications*, John Wiley & Sons, Chichester, UK, 2006.
20. M. A. Green, E. D. Dunlop, J. Hohl-Ebinger, M. Yoshita, N. Kopidakis and X. Hao, *Prog. Photovolt. Res. Appl.*, 2024, 32, 3–28.
21. A. Kojima, K. Teshima, Y. Shirai and T. Miyasaka, *J. Am. Chem. Soc.*, 2009, 131, 6050–6051.
22. Wikipedia contributors, Solar cell, Wikipedia, https://en.wikipedia.org/wiki/Solar_cell, (accessed June 18, 2026).
23. Goldstein H, Jackson K, Types of PV Panels, Lafayette College, https://sites.lafayette.edu/egrs352-sp15-pv/how-do-solar-pv-panels-work/types-of-pv-panels/, (accessed June 18, 2026)
24. A. Mishra, M. K. R. Fischer and P. Buerle, Angew. Chem. Int. Ed., 2009, 48, 2474.
25. F. Ma, Y. Zhao, Z. Qu and J. You, *Acc. Mater. Res.*, 2023, 4(8), 716–725.
26. F. Pei, Y. Chen, Q. Wang, L. Li, Y. Ma, H. Liu, Y. Duan, T. Song, H. Xie, G. Liu and N. Yang, *Nat. Commun.*, 2024, 15(1), 7024.
27. N. Rolston, A. Bush, M. D. McGehee and R. H. Dauskardt, *Nat. Energy*, 2022, 7, 341–351.
28. A. Al-Ashouri, E. Köhnen, B. Li, A. Magomedov, H. Hempel, P. Caprioglio and S. Albrecht, *Science*, 2020, 370, 1300–1309.
29. Q. Dong, Y. Fang, Y. Shao, P. Mulligan, J. Qiu, L. Cao and J. Huang, *Science*, 2015, 347, 967–970.
30. W. S. Yang, B.-W. Park, E. H. Jung, N. J. Jeon, Y. C. Kim, D. U. Lee and S. I. Seok, *Science*, 2017, 356, 1376–1379.
31. G. Xing, N. Mathews, S. Sun, S. S. Lim, Y. M. Lam, M. Grätzel, S. Mhaisalkar and T. C. Sum, *Science*, 2013, 342, 344–347.
32. S. D. Stranks and H. J. Snaith, *Nat. Nanotechnol.*, 2015, 10, 391–402.
33. J.-P. Correa-Baena, A. Abate, M. Saliba, W. Tress, T. J. Jacobsson, M. Grätzel and A. Hagfeldt, *Energy Environ. Sci.*, 2017, 10, 710–727.
34. M. Saliba, T. Matsui, J.-Y. Seo, K. Domanski, J.-P. Correa-Baena, M. K. Nazeeruddin, S. M. Zakeeruddin, W. Tress, A. Abate, A. Hagfeldt and M. Grätzel, *Energy Environ. Sci.*, 2016, 9, 1989–1997.

35. J. Seo, S. Park, Y. C. Kim, N. J. Jeon, J. H. Noh and S. I. Seok, *Adv. Mater.*, 2014, 26, 4360–4364.
36. T. A. Berhe, W.-N. Su, C.-H. Chen, C.-J. Pan, J.-H. Cheng, H.-M. Chen, M.-C. Tsai, L.-Y. Chen, A. A. Dubale and B.-J. Hwang, *Energy Environ. Sci.*, 2016, 9, 323–356.
37. Y. Zhao and K. Zhu, *Chem. Soc. Rev.*, 2016, 45, 655–689.
38. C. C. Stoumpos and M. G. Kanatzidis, *Acc. Chem. Res.*, 2015, 48, 2791–2802.
39. M. Pazoki *et al.*, *Energy Environ. Sci.*, 2018, 11, 246–264.
40. A. Miyata, A. Mitioglu, P. Plochocka, J. T.-W. Wang, S. D. Stranks, H. J. Snaith and R. J. Nicholas, *Nat. Phys.*, 2015, 11, 582–587.
41. F. F. Targhi *et al.*, *J. Energy Chem.*, 2018, 27, 515–523.
42. Overview of Solar Cells, Huake Technology, https://www.huake-tek.com/gaikuangtaiyangnengdianchi.html, (accessed June 18, 2026).
43. J. Warby, F. Zu, S. Zeiske, E. Gutierrez-Partida, L. Frohloff, S. Kahmann, K. Frohna, E. Mosconi, E. Radicchi, F. Lang and S. Shah, *Adv. Energy Mater.*, 2022, 12(12), 2103567.
44. N. J. Jeon, J. H. Noh, Y. C. Kim, W. S. Yang, S. Ryu and S. I. Seok, *Nat. Mater.*, 2014, 13, 897–903.
45. M. Dkhili, G. Lucarelli, F. De Rossi, B. Taheri, K. Hammedi, H. Ezzaouia, F. Brunetti and T. M. Brown, *ACS Appl. Energy Mater.*, 2022, 5(4), 4096–4107.
46. H. Zhang, M. K. Nazeeruddin and W. C. H. Choy, *Adv. Mater.*, 2019, 31, 1805702.
47. Q. Wang, Z. Lin, J. Su, Z. Hu, J. Chang and Y. Hao, *Nano Sel.*, 2021, *2*(6), 1055–1080.
48. J. Burschka, N. Pellet, S.-J. Moon, R. Humphry-Baker, P. Gao, M. K. Nazeeruddin and M. Grätzel, *Nature*, 2013, 499, 316–319.
49. A. Siphelo Ngqoloda, C. J. Arendse, T. F. G. Muller and M. D. Malevu, *Solar Energy*, 2021, 215, 179.
50. F. M. Rombach, *Energy Environ. Sci.*, 2021, 14, 3776–3794.
51. Afre, R. A. and D. Pugliese, *Micromachines*, 2024, 15(2), 192.

52. X. Shi, K. Xu, Y. He, Z. Peng, X. Meng, F. Wan, Y. Zhang, Q. Guo and Y. Chen, *Nano-Micro Lett.*, 2025, 17(1), 313.
53. T. A. Chowdhury, M. A. B. Zafar, M. S. U. Islam, M. Shahinuzzaman, M. A. Islam and M. U. Khandaker, *RSC Adv.*, 2023, 13, 1787–1810.
54. P. Zhou, T. Bu, S. Shi, L. Li, Y. Zhang, Z. Ku, Y. Peng, J. Zhong, Y.-B. Cheng and F. Huang, *J. Mater. Chem. C*, 2018, 6, 5733–5737.
55. W. M. Gu, K. J. Jiang, F. Li, G. H. Yu, Y. Xu, X. H. Fan, C. Y. Gao, L. M. Yang and Y. Song, *Chem. Eng. J.*, 2022, 444, 136644.
56. M. A. Green, A. Ho-Baillie and H. J. Snaith, *Nat. Photonics*, 2014, 8, 506–514.
57. N. S. Kumar and K. C. B. Naidu, *J. Materiomics*, 2021, *7*(5), 940–956.
58. V. D'Innocenzo, G. Grancini, M. J. P. Alcocer, A. R. S. Kandada, S. D. Stranks, M. M. Lee, G. Lanzani, H. J. Snaith and A. Petrozza, *Nat. Commun.*, 2014, 5, 3586.
59. J. Shi, Y. Li, Y. Li, D. Li, Y. Luo, H. Wu and Q. Meng, *Joule*, 2018, *2*(5), 879–901.
60. B. Das, Z. Liu, I. Aguilera, U. Rau and T. Kirchartz, *Mater. Adv.*, 2021, *2*(11), 3655–3670.
61. Z. Iqbal, F. Zu, A. Musiienko, E. Gutierrez-Partida, H. Köbler, T. W. Gries, G. V. Sannino, L. Canil, N. Koch, M. Stolterfoht and D. Neher, *ACS Energy Lett.*, 2023, 8, 4304–4314.
62. W. Tress, *Adv. Energy Mater.*, 2017, 7, 1602358.
63. S. De Wolf, J. Holovsky, S.-J. Moon, P. Löper, B. Niesen, M. Ledinsky, F.-J. Haug, J.-H. Yum and C. Ballif, *J. Phys. Chem. Lett.*, 2014, 5, 1035–1039.
64. A. Abate, T. Leijtens, S. Pathak, J. Teuscher, R. Avolio, M. E. Errico, J. Kirkpatrik, J. M. Ball, P. Docampo, I. McPherson and H. J. Snaith, *Phys. Chem. Chem. Phys.*, 2013, 15, 2572–2579.
65. C. Ma and N.-G. Park, *Chem*, 2020, *6*(6), 1254–1264.

66. R. D. Oliver, P. Caprioglio, F. Peña-Camargo, L. R. Buizza, F. Zu, A. J. Ramadan, S. G. Motti, S. Mahesh, M. M. McCarthy, J. H. Warby and Y. H. Lin, *Energy Environ. Sci.*, 2022, *15*(2), 714–726.
67. N. Arora, M. I. Dar, A. Hinderhofer, N. Pellet, F. Schreiber, S. M. Zakeeruddin and M. Grätzel, *Science*, 2017, *358*, 768–771.
68. D. Zhang, D. Li, Y. Yang, W. Wang and G. Xing, *Commun. Mater.*, 2022, *3*, 58.
69. Y. J. Chang, N. H. Chen, T. Y. Chen, Y. M. Shuang and Y. S. Yen, *ACS Appl. Energy Mater.*, 2024, *7*(3), 1287–1297.
70. F. Bonaccorso, Z. Sun, T. Hasan and A. C. Ferrari, *Nat. Photonics*, 2010, *4*, 611–622.
71. K. S. Novoselov, A. K. Geim, S. V. Morozov, D. Jiang, Y. Zhang, S. V. Dubonos, I. V. Grigorieva and A. A. Firsov, *Science*, 2004, *306*, 666–669.
72. Q. H. Wang, K. Kalantar-Zadeh, A. Kis, J. N. Coleman and M. S. Strano, *Nat. Nanotechnol.*, 2012, *7*, 699–712.
73. M. Chhowalla, H. S. Shin, G. Eda, L. J. Li, K. P. Loh and H. Zhang, *Nat. Chem.*, 2013, *5*, 263–275.
74. C. S. Diercks and O. M. Yaghi, *Science*, 2017, *355,* eaal1585.
75. S. Y. Ding and W. Wang, *Chem. Soc. Rev.*, 2013, *42*, 548–568.
76. P. Apostol, S. M. Gali, A. Su, D. Tie, Y. Zhang, S. Pal, X. Lin, V. R. Bakuru, D. Rambabu, D. Beljonne and M. Dincă, *J. Am. Chem. Soc.*, 2023, *145*(45), 24669–24677.
77. T. Rodenas, I. Luz, G. Prieto, B. Seoane, H. Miro, A. Corma, F. Kapteijn, F. X. Llabrés i Xamena and J. Gascon, *Nat. Mater.*, 2014, *14*, 48–55.
78. H. Lyu, W. Zhou, Y. Guo, Q. Zhang, W. Wu, H. Yu and Y. Zhao, *Adv. Mater.*, 2020, *32*, 1907310.
79. J. Ji, X. Meng, S. Wu, T. Hu, W. Wang and Y. Chen, *Cell Rep. Phys. Sci.*, 2021, *2*, 100515.
80. S. Yang, Y. Li, X. Cheng, L. Wang, J. Liu, H. Yu and W. Huang, *Adv. Funct. Mater.*, 2022, *32*, 2201710.

81. G. Chakraborty, I. H. Park, R. Medishetty and J. J. Vittal, *Chem. Rev.*, 2021, *121*(7), 3751–3891.
82. S. Kitagawa, R. Kitaura and S. Noro, *Angew. Chem. Int. Ed.*, 2004, *43*, 2334–2375.
83. S. Khan and M. Shahid, *Mater. Adv.*, 2021, *2*(15), 4914–4944.
84. H. Ma, H. Ren, X. Meng, H. Sun, L. Yan and G. Zhu, *Chem. Commun.*, 2013, *49*, 9773–9775.
85. J. H. Cavka, S. Jakobsen, U. Olsbye, N. Guillou, C. Lamberti, S. Bordiga and K. P. Lillerud, *J. Am. Chem. Soc.*, 2008, *130*, 13850–13851.
86. M. Xie, J. Liu, L. Dai, H. Peng and Y. Xie, *RSC Adv.*, 2023, *13(35),* 24699–24730.
87. A. J. Clough, J. W. Yoo, M. H. Mecklenburg and S. C. Marinescu, *J. Am. Chem. Soc.*, 2015, *137*, 118–121.
88. C. R. Mulzer, L. Shen, R. P. Bisbey, J. R. McKone, N. Kornienko, M. R. Dichtel and C. A. Mirkin, *ACS Cent. Sci.*, 2016, *2*, 667–673.
89. J. Liu, L. Chen, H. Cui, J. Zhang, L. Zhang and C. Y. Su, *Chem. Soc. Rev.*, 2014, *43*, 6011–6061.
90. N. Huang, P. Wang and D. Jiang, *Nat. Rev. Mater.*, 2016, *1*, 16068.
91. D. J. Ashworth and J. A. Foster, *J. Mater. Chem. A*, 2018, *6*, 16292–16307.
92. R. Saha, K. Gupta and C. J. Gomez Garcia, *Cryst. Growth Des.*, 2024, *24*(5), 2235–2265.
93. D. Sheberla, J. C. Bachman, J. S. Elias, C. J. Sun, Y. Shao-Horn and M. Dincă, *Nat. Mater.*, 2017, *16*(2), 220–224.
94. R. W. Day, D. K. Bediako, M. Rezaee, L. R. Parent, G. Skorupskii, M. Q. Arguilla, C. H. Hendon, I. Stassen, N. C. Gianneschi, P. Kim and M. Dincă, *ACS Cent. Sci.*, 2019, *5*(12), 1959–1966.
95. M. G. Campbell, D. Sheberla, S. F. Liu, T. M. Swager and M. Dincă, *Angew. Chem. Int. Ed.*, 2015, *54*, 4349–4352.
96. L. S. Xie, G. Skorupskii and M. Dincă, *Chem. Rev.*, 2020, *120*(16), 8536–8580.

97. X. Huang, S. Sheng, Z. Chen, Z. Chen, R. Dong, X. Feng and H. Xu, *Chem. Soc. Rev.*, 2021, *50*, 1138–1164.

98. R. Dong, T. Zhang and X. Feng, *Chem. Rev.*, 2018, *118*, 6189–6235.

99. A. Schneemann, V. Bon, I. Schwedler, I. Senkovska, S. Kaskel and R. A. Fischer, *Chem. Soc. Rev.*, 2014, *43*(16), 6062–6096.

100. S. S. Rajasree, X. Li and P. Deria, *Commun. Chem.*, 2021, *4*(1), 47.

101. R. Saha and C. J. G. García, *Chem. Soc. Rev.*, 2024, *53*, 9490–9559.

102. S. M. Cohen, *Chem. Rev.*, 2012, *112*, 970–1000.

103. K. K. Tanabe and S. M. Cohen, *Chem. Soc. Rev.*, 2011, *40*, 498–519.

104. Y. Bai, Y. Fang, Y. Deng, Q. Wang, J. Zhao, X. Zheng, Y. Zhang and J. Huang, *Nat. Mater.*, 2019, *18*, 465–471.

105. H. Tsao, H. Yi, Y. Xu, P. Chen, S. Yang and Y. Li, *Adv. Mater.*, 2018, *30*, 1704859.

106. Gallego, C. Hermosa, O. Castillo, I. Berlanga, C. J. Gómez-García, E. Mateo-Martí, J. I. Martínez, F. Flores, C. Gómez-Navarro, J. Gómez-Herrero and S. Delgado, Adv. Mater., 2013, 25, 2141–2146.

107. V. Nicolosi, M. Chhowalla, M. G. Kanatzidis, M. S. Strano and J. N. Coleman, Science, 2013, 340, 1226419.

108. Y. Peng, Y. Li, Y. Ban, H. Jin, W. Jiao, X. Liu and W. Yang, Science, 2014, 346, 1356–1359.

109. X. Wang, C. Chi, K. Zhang, Y. Qian, K. M. Gupta, Z. Kang, J. Jiang and D. Zhao, Nat. Commun., 2017, 8, 14460.

110. R. Makiura, S. Motoyama, Y. Umemura, H. Yamanaka, O. Sakata and H. Kitagawa, Nat. Mater., 2010, 9, 565–571.

111. M. Zhao, Q. Lu, Q. Ma and H. Zhang, Small Methods, 2017, 1, 1600030.

112. W. Cao, J. Li, H. Chen and J. Xue, *J. Photonics Energy*, 2014, 4, 040990.

113. Z. Jin, J. Yan, X. Huang, W. Xu, S. Yang, D. Zhu and J. Wang, *Nano Energy*, 2017, 40, 376–381.

114. C. Liu, C. Wang, H. Wang, T. Wang and J. Jiang, *Eur. J. Inorg. Chem.*, 2019, 45, 4815–4819.

115. K. Sasitharan, D. G. Bossanyi, N. Vaenas, A. J. Parnell, J. Clark, A. Iraqi, D. G. Lidzey and J. A. Foster, *J. Mater. Chem. A*, 2020, 8, 6067–6075.

116. K. Sasitharan, R. C. Kilbride, E. L. K. Spooner, J. Clark, A. Iraqi, D. G. Lidzey and J. A. Foster, *Adv. Sci.*, 2022, 9, 2104683.

117. Wu, Z. Li, M. Q. Li, Y. Diao, F. Lin, T. Liu, J. Zhang, P. Tieu, W. Gao, F. Qi and X. Pan, *Nat. Nanotechnol.*, 2020, 15, 934–940.

Chapter 2 Experimental Characterization Techniques

2.1 Introduction

Materials science and device engineering rely on analytical techniques to reveal structural, chemical, optical, and electronic properties. This chapter introduces ten methods used later in the work: X-ray diffraction (XRD), Fourier-transform infrared spectroscopy (FT-IR), ultraviolet–visible absorption spectroscopy (UV–Vis), atomic force microscopy (AFM), scanning electron microscopy (SEM), photoluminescence spectroscopy (PL), grazing-incidence wide-angle X-ray scattering (GIWAXS), current–voltage (J–V) measurements, external quantum efficiency (EQE), and ultraviolet photoelectron spectroscopy (UPS).

2.2 X-ray diffraction (XRD)

XRD is one of the most reliable methods for determining the crystalline order in layered and nanosheet materials. When an incident X-ray beam strikes the periodic arrangement of atoms within a crystal, part of the radiation is scattered elastically by electrons. If the path difference between scattered rays from successive planes equals an integer multiple of the X-ray wavelength, constructive interference occurs, producing a diffraction peak at a defined angle according to Bragg's law (Equation 2.1). The experimental arrangement typically places the powdered or thin film sample on a flat substrate (e.g. silicon wafer), with both the X-ray source and the detector mounted on a goniometer that allows synchronous rotation (Figure 2.1). This geometry ensures that the full angular range of 2θ values can be scanned to capture all reflections from the crystal planes. A knife edge is commonly positioned just above the sample to block reflected or scattered background radiation, thereby improving the signal-to-noise ratio of the diffracted beams collected by the detector.

In the case of powder X-ray diffraction (PXRD), the incident beam interacts with an ensemble of randomly oriented micro crystallites. Because each possible lattice

orientation is statistically present, diffraction from all accessible planes can be detected, resulting in a composite diffraction pattern that represents the bulk material. The positions of peaks correspond directly to interplanar distances, while their relative intensities provide information about preferred orientation and atomic arrangement. Peak broadening, on the other hand, reflects small crystallite sizes or lattice strain. As such, PXRD can be used both as a fingerprinting technique to confirm phase identity and as a quantitative tool to assess crystallinity and microstructural quality of metal–organic nanosheets (MONs).

$$n\lambda = 2d\sin\theta \qquad \text{Equation 2.1}$$

Where θ is the angle of diffraction, n is an integer, λ is the wavelength of incident X-rays, and d is the spacing between adjacent crystal planes.

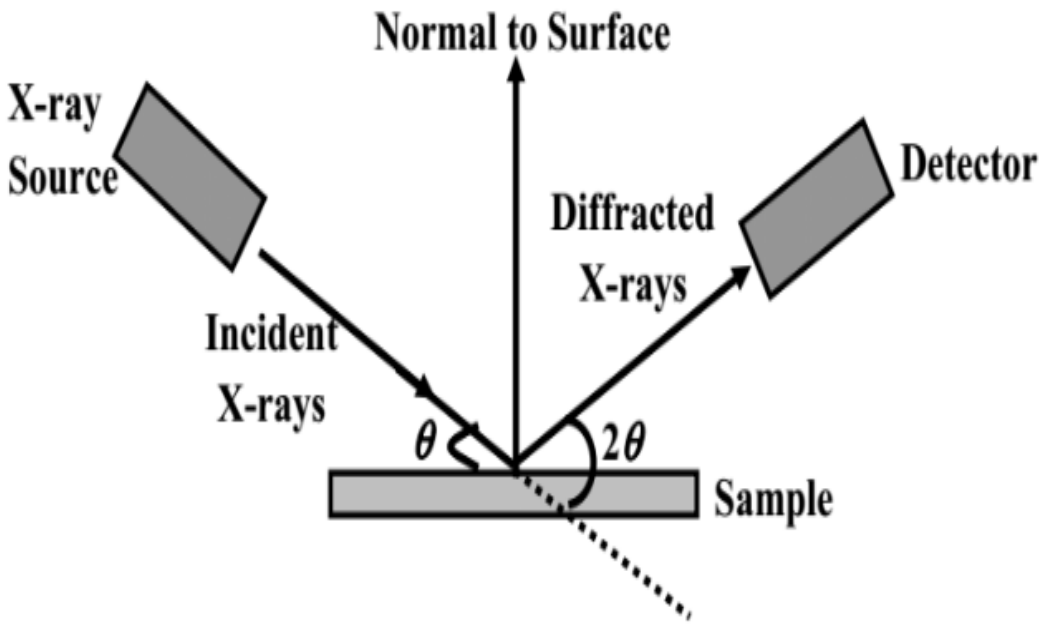

Figure 2.1 Schematic Representation on the Working Principles of X-ray Diffraction.

2.3 Fourier-transform infrared spectroscopy (FT-IR)

FT-IR is a widely used technique for probing the vibrational modes of molecules, which allows identification of functional groups and bonding states in materials. When infrared light interacts with a sample, photons with energies that match the vibrational

transitions of chemical bonds are absorbed, leading to characteristic peaks in the IR spectrum.[1]

An FT-IR instrument generally consists of a broadband IR source, a Michelson interferometer to modulate the light, and a detector that records the transmitted or reflected signal. The interferogram collected in the time domain is mathematically converted into a frequency-domain spectrum via Fourier transform, providing fast and high-resolution spectral data across a broad range.

For MONs, FT-IR is particularly valuable for confirming the coordination between metal centers and organic linkers. For example, the disappearance of the carboxylic acid C=O stretching band around 1700 cm^{-1}, together with the emergence of new peaks near 1600 cm^{-1} and 1400 cm^{-1}, is often taken as evidence of deprotonation and coordination of carboxylate groups to metal nodes.[2]

By comparing the spectra of free ligands with those of the final nanosheet material, FT-IR thus provides a quick and reliable fingerprint to verify framework formation and bonding environment.

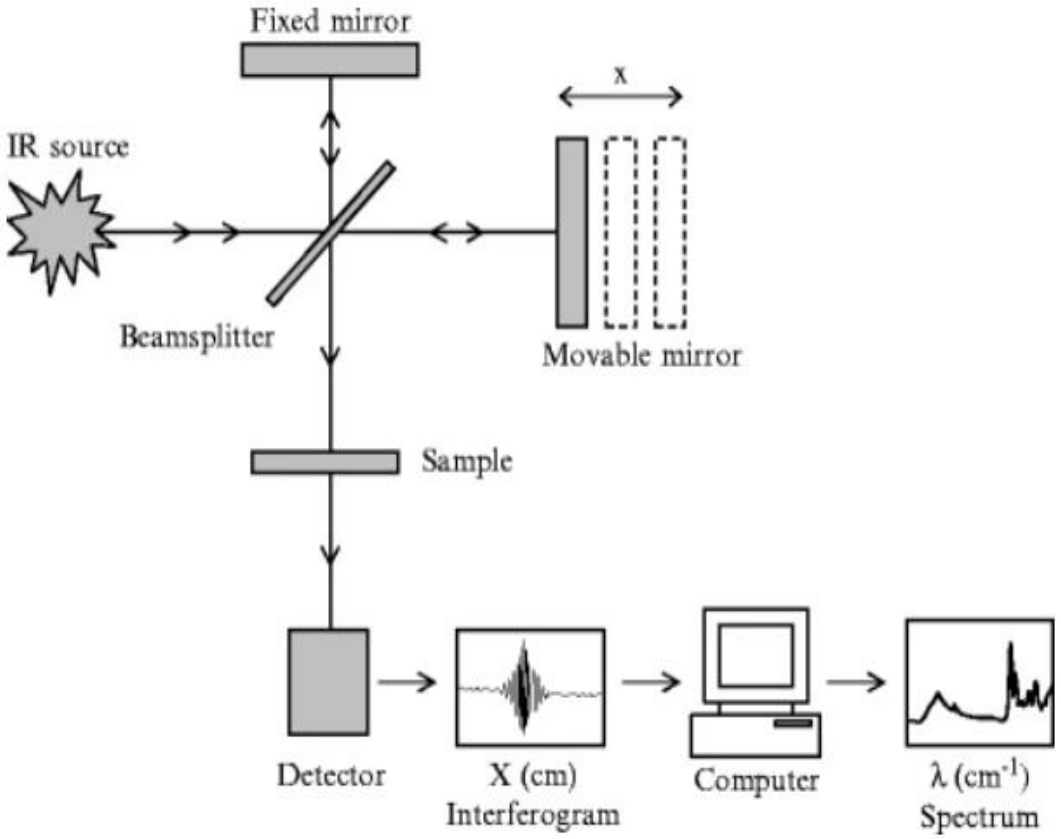

Figure 2.2 Schematic sketch of the essential features of a Fourier transforms infrared (FT-IR) spectrometer.

2.4 Ultraviolet–visible (UV–Vis) absorption spectroscopy

UV-Vis is a commonly used optical technique to study how materials absorb light in the ultraviolet and visible regions. The basic principle is that when the photon energy matches the gap between electronic states, electrons are promoted from a lower to a higher energy level, producing characteristic absorption peaks in the spectrum. In organic molecules, these transitions are usually $\pi \rightarrow \pi^*$ or $n \rightarrow \pi^*$, while in semiconductors or insulators they correspond to electronic transitions from the valence band to the conduction band.[3]

The experimental setup typically consists of a UV light source (such as a deuterium lamp) and a visible light source (such as a tungsten–halogen lamp). After passing through a monochromator, the selected wavelengths illuminate the sample, and a

detector records the transmitted or reflected intensity. According to the Beer–Lambert law, the absorbance A is proportional to the concentration c of the absorbing species and the optical path length l:

$$A = \log_{10}\left(\frac{I_0}{I_t}\right) = \varepsilon cl \quad \textbf{Equation 2.2}$$

where I_0 is the incident light intensity, I_t is the transmitted intensity, and ε is the molar absorptivity.

For MONs, UV–Vis absorption spectroscopy is particularly useful for monitoring changes in the electronic structure of organic linkers during assembly. For instance, porphyrin linkers typically show a strong Soret band at around ~417 nm in their free state, but this peak shifts to ~425 nm once incorporated into Zn_2(ZnTCPP) nanosheets, indicating stronger π–π stacking and enhanced intermolecular interactions.[4] In addition, the Q bands in the 500–700 nm range often split into multiple peaks, and their shape and number can be used to assess the degree of metalation and symmetry changes.[5] These spectral features provide direct evidence for nanosheet formation and electronic coupling.

Therefore, UV–Vis spectroscopy not only allows estimation of the optical band gap of MONs but also reveals how molecular assembly affects light absorption, serving as an important tool to connect structural features with optoelectronic performance.

2.5 Atomic force microscopy (AFM)

AFM is a high-resolution surface analysis technique that provides direct three-dimensional images of samples at the nanometer scale. Its operating principle relies on the interaction between a sharp nanoscale probe mounted on a flexible cantilever and the surface of the material. As the probe scans across the surface, local interaction forces cause tiny deflections of the cantilever. A laser beam reflected from the end of the cantilever onto a quadrant photodiode detects these deflections, which are then converted into height information to reconstruct a topographical image of the sample.[6]

Depending on the interaction mode, AFM typically operates in three configurations: contact, tapping, and non-contact. In contact mode, the probe remains in constant contact with the sample, which is effective for rigid materials but may damage soft samples. Tapping mode reduces sample disturbance by intermittently contacting and withdrawing from the surface, making it the most common choice for organic materials, polymers, and metal–organic framework–based materials. Non-contact mode maintains a small separation between the probe and the sample, which is suitable for fragile or easily deformed samples but often yields lower signal-to-noise ratios.

In the study of MONs, AFM plays a central role. It enables direct measurement of nanosheet thickness and lateral dimensions. AFM images can also reveal nanosheet dispersion and stacking behavior: well-dispersed nanosheets appear as uniformly distributed thin sheets, whereas aggregated nanosheets show increased local height and block-like features. Statistical analysis of height profiles further allows estimation of the fraction of monolayers versus multilayers, offering insight into the degree of synthetic control.

In addition, AFM is widely used to evaluate the uniformity and surface roughness of MON films deposited on substrates. For device applications, smoother films generally correlate with better continuity and charge transport properties. Thus, AFM not only verifies the two-dimensional morphology of MONs but also provides indirect links to device performance. Overall, AFM is an essential tool for connecting nanosheet structural characteristics with functional properties.

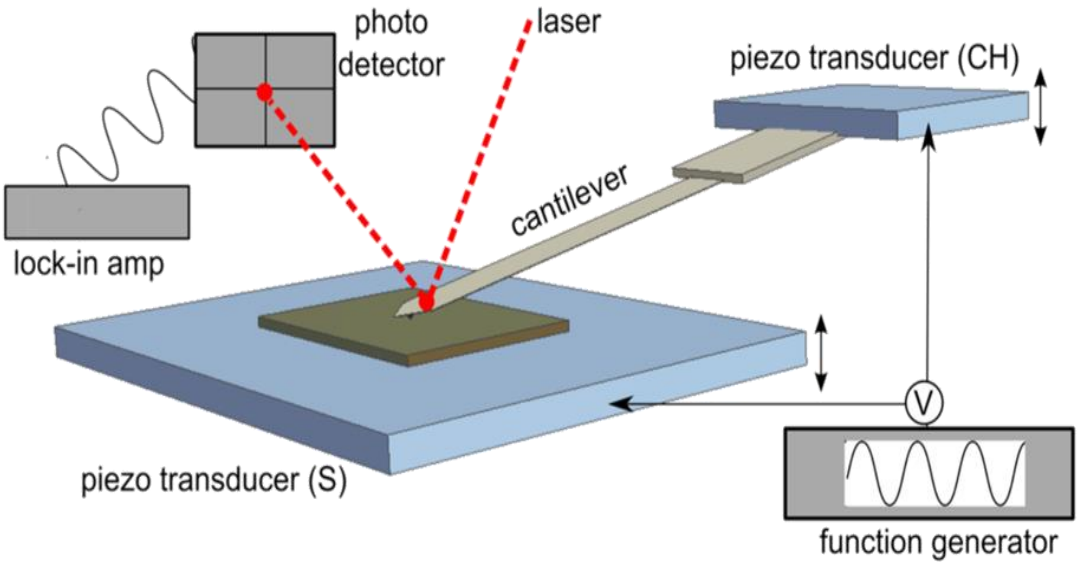

Figure 2.3 Schematics of Atomic-force microscopy (AFM)[7]

2.6 Scanning electron microscopy (SEM)

SEM is a powerful imaging technique that provides detailed information about the surface morphology of materials. The principle is based on scanning a focused beam of high-energy electrons across the sample surface. When the electron beam interacts with the atoms of the sample, various signals are generated, including secondary electrons, backscattered electrons, and characteristic X-rays. Among these, secondary electrons are most collected to form high-resolution images, as their emission is highly sensitive to surface topography.

A standard SEM setup consists of an electron gun, electromagnetic lenses to focus the beam, a scanning system, and detectors for different electron signals. By rostering the focused beam over the surface and collecting the emitted electrons, SEM produces images with a large depth of field and spatial resolution down to a few nanometers.[8] In addition, backscattered electron detection can provide compositional contrast, since heavier elements scatter electrons more efficiently, appearing brighter in the image.

For MONs, SEM is mainly used to visualize nanosheet morphology and aggregation at the microscale. Unlike AFM, which excels at thickness measurement, SEM offers a

broader view of lateral dimensions, sheet stacking, and surface coverage across larger areas.[8] Furthermore, SEM can reveal the continuity and homogeneity of MON films on substrates, providing important feedback for device integration.

Therefore, SEM complements AFM by offering morphological information at a larger scale, making it an indispensable technique for evaluating the quality, distribution, and film-forming behavior of MONs.

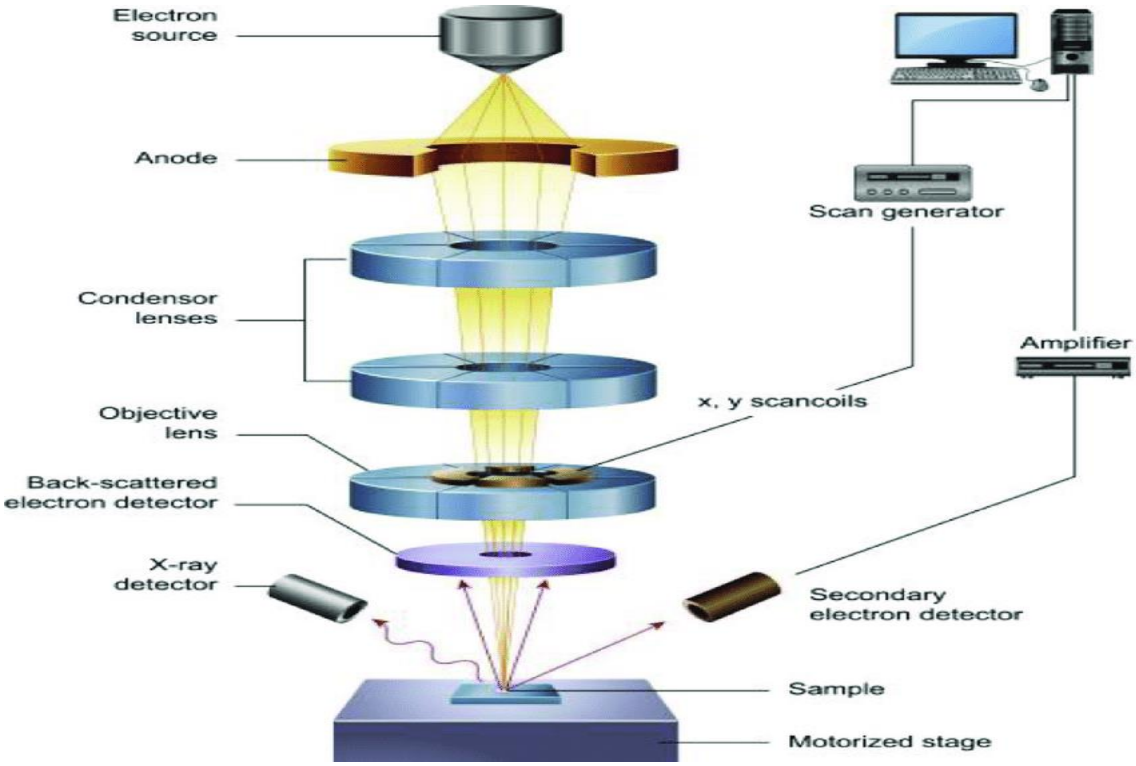

Figure 2.4 Schematics of Scanning electron microscopy (SEM)[9]

2.7 Photoluminescence spectroscopy (PL)

PL is an important optical characterization method for studying the excited-state behavior of materials. Its basic principle is that, after absorbing photons, electrons are promoted from the ground state to an excited state and subsequently return to lower energy states through radiative recombination, emitting photons in the process. By monitoring the wavelength and intensity of the emitted light, valuable information on the electronic structure and excited-state decay pathways of the material can be

obtained.

A typical PL setup consists of an excitation light source (such as a laser or xenon lamp), a monochromator, and a photo detector. The excitation source provides high-energy photons to irradiate the sample, the monochromator separates the emitted light, and the detector records the emission intensity as a wavelength function, thereby generating the emission spectrum.[10]

In material characterization, PL is often used to analyze the position and intensity of emission peaks. For instance, fluorescence quenching is typically associated with enhanced intermolecular interactions, the presence of defects, or increased non-radiative recombination channels. Meanwhile, redshifts or blueshifts in the emission peaks may indicate modifications in the electronic structure or the presence of aggregation effects.[11] In the study of MONs, PL spectra provide direct evidence of the changes in emission behavior after the assembly of organic ligands into two-dimensional structures. For example, porphyrin-based MONs often exhibits significant fluorescence quenching, which is usually interpreted because of stronger intermolecular coupling and enhanced exciton dissipation pathways. By comparing the PL spectra of free ligands and assembled nanosheets, researchers can quickly assess how framework construction influences exciton migration and energy dissipation and further relate these effects to performance in optoelectronic devices.

Therefore, PL spectroscopy not only provides straightforward information about emission levels and excited-state dynamics but also serves as a valuable tool to verify the correlation between structural changes and optoelectronic properties.

2.8 Grazing-incidence wide-angle X-ray scattering (GIWAXS)

GIWAXS is a structural characterization technique widely used to probe crystalline, molecular orientation, and packing order of thin films. Its operating principle is based on directing an incident X-ray beam onto the sample at a shallow angle, typically below the critical angle for total external reflection. This grazing-incidence geometry

enhances surface sensitivity and minimizes penetration depth, making GIWAXS especially suitable for studying thin films and nanostructured materials.

In a typical GIWAXS experiment, the sample is mounted at a fixed grazing angle, while a two-dimensional detector records the scattered X-rays over a wide angular range. The resulting diffraction patterns provide information about both in-plane and out-of-plane ordering, allowing researchers to determine lattice spacings, crystallite orientation, and degree of texture in thin-film samples.[12] Compared with conventional XRD, which primarily probes bulk crystallinity, GIWAXS offers higher sensitivity to surface and interfacial structures, which are often critical in device applications.

For materials, GIWAXS is particularly powerful in revealing molecular packing and stacking orientation within films. For instance, the presence of sharp diffraction spots indicates highly ordered domains, whereas diffuse halos suggest amorphous or disordered arrangements.[12] In device-oriented studies, GIWAXS patterns are often used to correlate structural ordering with charge transport efficiency, as improved crystallinity and preferential molecular orientation typically enhance carrier mobility and overall device performance.

Thus, GIWAXS serves as an indispensable tool for connecting thin-film structure to functional properties, providing insights that cannot be obtained by bulk diffraction methods alone.

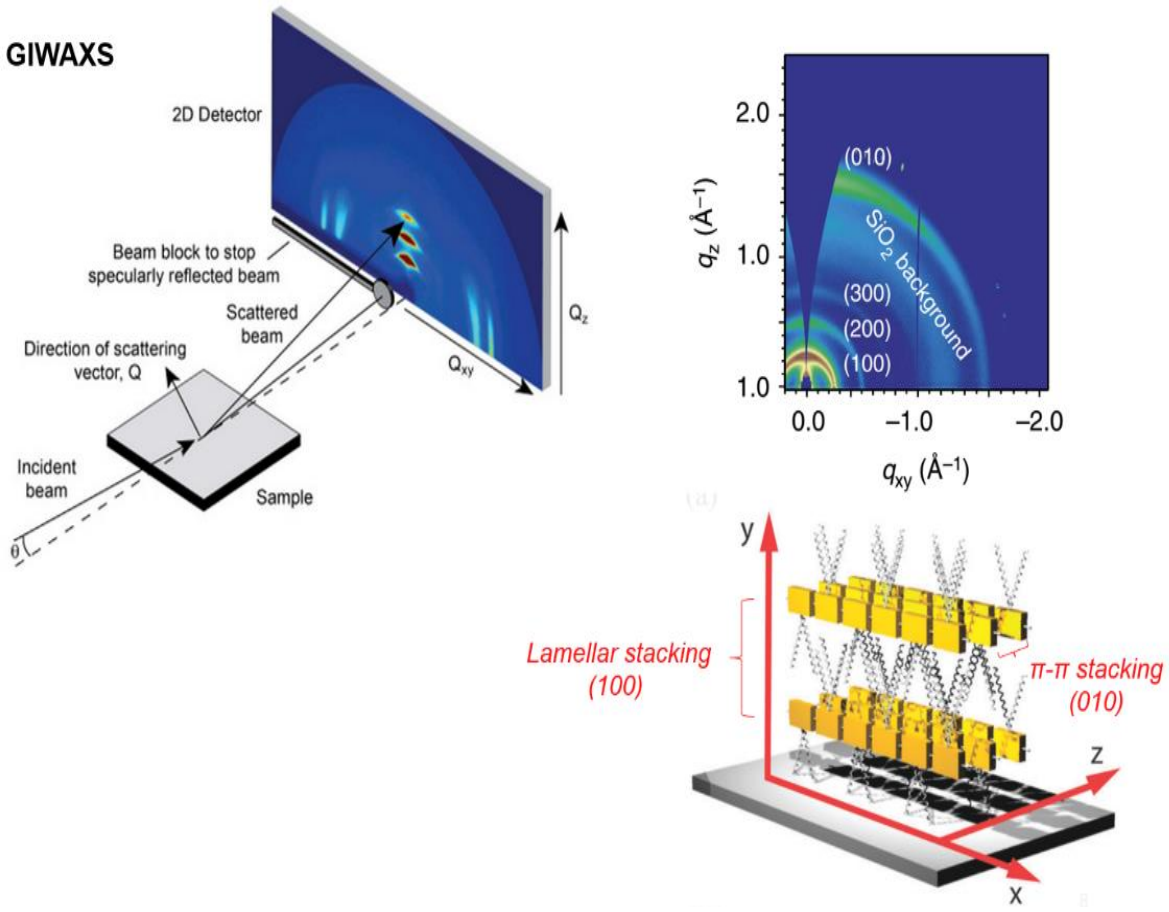

Figure 2.5 Schematic sketch of the essential features of a GIWAXS spectrometer. (Yu et al[14])

2.9 Current–voltage (J–V) measurements

J-V test is the most fundamental electrical characterization method for evaluating the performance of photovoltaic and optoelectronic devices, particularly solar cells. The basic principle is to apply an external voltage across the device while recording the corresponding current density (J), thereby generating a current–voltage curve. This curve not only reflects the phenomenological performance of the device but also reveals limiting processes in charge generation, separation, transport, and collection.

Standard J–V measurements are typically carried out under simulated AM 1.5G solar illumination (100 mW·cm^{-2}) using a solar simulator as the light source, while a source meter precisely controls the applied voltage and measures the current response. Both forward scans (from short-circuit to open-circuit) and reverse scans (from open-circuit

to short-circuit) are usually performed to assess hysteresis behavior, which is particularly relevant for PSCs. Such hysteresis often originates from ion migration, interfacial charge accumulation, or slow carrier dynamics.[15]

In functional material studies, J–V measurements are often used to evaluate the role of newly introduced layers or additives. For instance, when MONs is incorporated into charge transport layers, improvements in charge injection and extraction are typically manifested as parameters. This resulted in an overall enhancement of solar cells' performance. Moreover, dark J–V measurements provide additional insight into diode behavior, charge injection barriers, and recombination mechanisms, enabling a deeper understanding of how material modifications influence device operation.

Thus, J–V characterization is not only the basis for assessing photovoltaic performance but also an essential link between material design and device functionality.

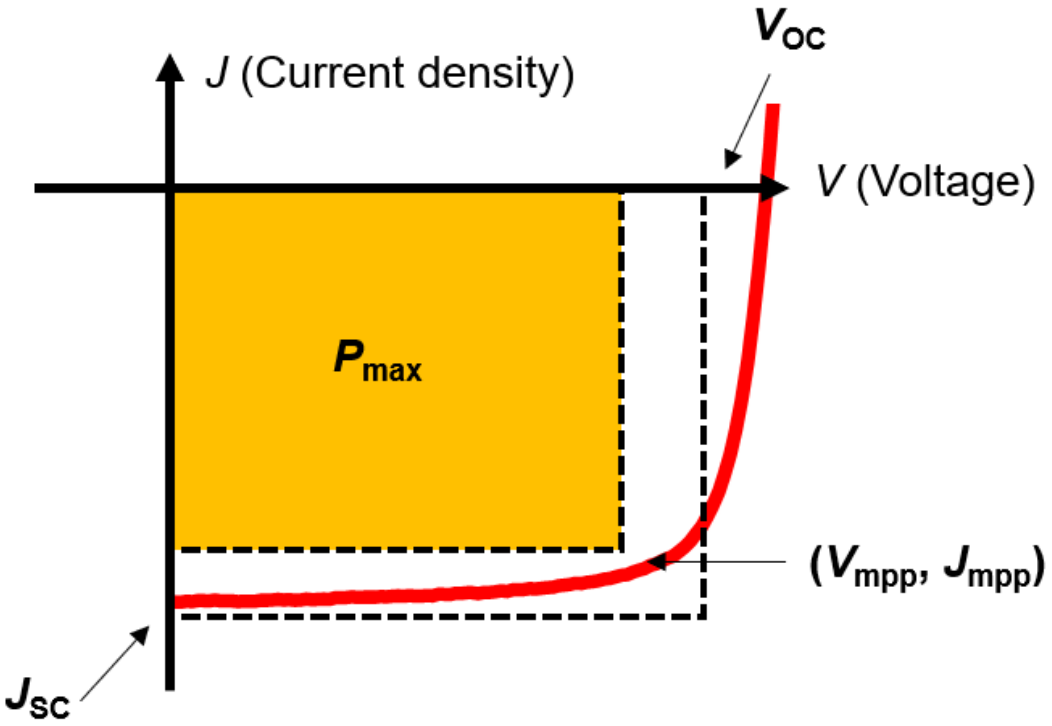

Figure 2.6 Current density–voltage (J–V) characteristic curve of a solar cell.

2.10 External quantum efficiency (EQE)

EQE is a key parameter in photovoltaic device characterization, describing the efficiency with which incident photons of a given wavelength are converted into collected charge carriers. It is defined as the ratio of the number of collected electrons to the number of incident photons. Unlike J–V measurements, which provide integral performance parameters, EQE offers spectral information that reveals how the device responds to different wavelengths of light.

Experimentally, EQE measurements are performed by illuminating the device with monochromatic light, often modulated to suppress background noise. The photocurrent response at each wavelength is recorded and combined with the incident photon flux to calculate the EQE value.[16]By integrating the EQE spectrum with the standard AM 1.5G solar spectrum, the short-circuit current density (Jsc) can be derived and compared with J–V measurements to ensure consistency.

In materials and device studies, EQE is often used to identify the origins of performance improvements. For example, an enhancement in EQE within a specific wavelength range indicates improved light absorption or charge separation efficiency in that spectral region. In PSCs, the incorporation of MONs as interfacial layers can lead to an increase in EQE across the visible region, suggesting more efficient photogenerated carrier extraction and transport, which ultimately contributes to higher power conversion efficiency.[17]

Thus, EQE is not only a complementary tool for validating J–V results but also an essential technique for understanding spectral response and optimizing device performance.

2.11 Ultraviolet photoelectron spectroscopy (UPS)

UPS is a widely used technique for probing the electronic structure of materials, particularly for determining the valence band position, work function, and highest

occupied molecular orbital (HOMO) level. The principle is based on irradiating the sample with ultraviolet photons (typically He I, 21.22 eV or He II, 40.8 eV). The photon energy is sufficient to excite electrons from the valence band or occupied molecular orbitals, allowing them to escape from the surface. By measuring the kinetic energy distribution of the emitted electrons, their binding energies can be derived, yielding information on the material's energy levels.

A typical UPS setup consists of a UV light source, a vacuum chamber, and an electron energy analyzer. During measurement, the analyzer records the number of electrons as a function of kinetic energy, producing a photoelectron spectrum. The high binding-energy cutoff is used to determine the work function (via the secondary electron cutoff), while the onset of the low binding-energy region corresponds to the HOMO energy. Combined with the optical band gap estimated from UV–Vis absorption, the lowest unoccupied molecular orbital (LUMO) level can also be inferred, enabling the construction of a complete energy level diagram.[18]

UPS is particularly important in optoelectronic device research, as energy level alignment strongly influences charge injection, transport, and extraction. For instance, when MONs are introduced as HTLs, the alignment of their HOMO levels with those of the perovskite absorber or electrode directly affects hole injection and mobility.[18] Thus, UPS results provide critical insights into whether interfacial barriers exist and whether the material is suitable for use as a charge transport layer.

Therefore, UPS is not only a powerful tool for elucidating the electronic structure of materials but also an essential technique for understanding energy-level alignment and optimizing device performance.

Reference

1. B. C. Smith, *Infrared Spectral Interpretation: A Systematic Approach*, CRC Press, Boca Raton, 2018.
2. Z. Hu, B. J. Deibert and J. Li, *Chem. Soc. Rev.*, 2014, 43, 5815–5840.
3. H. Zollinger, *Color Chemistry: Syntheses, Properties, and Applications of Organic Dyes and Pigments*, Wiley, Weinheim, 2003
4. P. Asselin and P. D. Harvey, *ACS Appl. Nano Mater.*, 2022, *5*, 6055–6082.
5. M. Gouterman, *J. Chem. Phys.*, 1959, *30*, 1139–1161.
6. G. Binnig, C. F. Quate and C. Gerber, *Phys. Rev. Lett.*, 1986, *56*, 930–933.
7. National Institute of Standards and Technology, *Scanning Probe Microscopy for Advanced Materials and Processes*, available at: https://www.nist.gov/programs-projects/scanning-probe-microscopy-advanced-materials-and-processes, accessed 30 September 2025.
8. L. Reimer, *Scanning Electron Microscopy: Physics of Image Formation and Microanalysis*, Springer, Berlin, 2000.
9. Nanoscope Instruments, *Scanning Electron Microscopy*, available at: https://www.nanoscience.com/techniques/scanning-electron-microscopy/, accessed 30 September 2025.
10. K. Prakash, B. Mishra, D. D. Díaz, C. M. Nagaraja and P. Pachfule, *J. Mater. Chem. A*, 2023, *11*, 14489–14538.
11. B. Valeur and M. N. Berberan-Santos, *Molecular Fluorescence: Principles and Applications*, Wiley, Weinheim, 2013.
12. Y. Liu, L. Wang, L. Xu and Y. Song, *J. Mater. Chem. C*, 2023, *11*, 5815–5840.
13. A. Hexemer and P. Müller-Buschbaum, *IUCrJ*, 2015, *2*, 106–125.
14. D. M. Smilgies, *Crystals*, 2025, *15*, 63.
15. H. Yu, Y. Wang, H. K. Kim, X. Wu, Y. Li, Z. Yao, M. Pan, X. Zou, J. Zhang, S. Chen and D. Zhao, *Adv. Mater.*, 2022, *34*, 2200361.
16. W. Tress, *Adv. Energy Mater.*, 2017, *7*, 1602358.
17. K. R. McIntosh and S. C. Baker-Finch, *IEEE J. Photovolt.*, 2015, *5*, 1563–1570.

18. H. Tang, Y. Bai, H. Zhao, X. Qin, Z. Hu, C. Zhou, F. Huang and Y. Cao, *Adv. Mater.*, 2024, *36*, 2212236.
19. R. J. Davis, M. T. Lloyd, S. R. Ferreira, M. J. Bruzek, S. E. Watkins, L. Lindell, P. Sehati, M. Fahlman, J. E. Anthony and J. W. Hsu, *J. Mater. Chem.*, 2011, *21*, 1721–1729.
20. Z. Zhou, S. Pang, Z. Liu, H. Xu and G. Cui, *J. Mater. Chem. A*, 2015, *3*, 19205–19217.

Chapter 3: Enhancing hole transport in perovskite solar cells using zinc porphyrin-based metal-organic nanosheets (MONs)

3.1 Introduction

Perovskite Solar Cells (PSCs) are one of the most promising photovoltaic technologies due to their high-power conversion efficiency (currently up to 31.25 %) [1] and ease of preparation. The high-Power coefficient efficiency (PCE) of PSCs is mainly due to the outstanding optoelectronic properties of perovskites, such as their excellent light absorption coefficient, long electron-hole diffusion length, and high defect tolerance.[2] Inorganic oxide, organic small molecules, and polymers are all commonly used in hole transport materials (HTMs) within PSCs. The thickness of the hole transport layer (HTL) plays a critical role in determining the device performance and reproducibility of PSCs. Too thin an HTL can cause incomplete coverage and hinder hole extraction, whereas an excessively thick layer increases series resistance. An optimal thickness of around 100 nm has been reported to balance efficient hole transport and reduced resistive losses.[3]

In HTMs, the use of functional additives is a well-established strategy to enhance film uniformity, optimize energy level alignment, and improve charge carrier mobility. For example, 2,2,7,7-tetrakis(N,N-di-p-methoxyphenylamine)-9,9′-spirobifluorene (Spiro-OMeTAD) is usually mixed with lithium bis(trifluoromethanesulfonyl)imide (Li-TFSI) and tert-butylpyridine (t-BP) as p-type dopants to achieve high conductivity and hole mobility when processed into the HTL.

Polymer HTM has better film-forming properties and is easy to fabricate. Poly[bis(4-phenyl) (2,4,6-trimethylphenyl) amine (PTAA), and Poly(3-hexylthiophene) (P3HT) are often used as HTMs.[4] Compared with the Spiro-OMeTAD, the semi-crystalline polymer P3HT has better stability and does not require support chemicals for stable use. However, the efficiency of P3HT-based solar cells is lower than other HTMs.[5]

Many studies have attempted to improve the performance of solar cells based on P3HT as HTL. A common way to improve the performance is to add dopant chemicals. The addition of Li-TFSI as an additive to the P3HT layer increased the performance from 14.30% to 17.55%.[6] However, it reduced the stability of the devices. In addition to additive or dopant strategies, interface engineering has also been employed to tune the performance of PSCs using P3HT as the HTL. For instance, poly (methyl methacrylate) (PMMA) has been inserted as an interfacial layer to adjust the energy-level alignment between the P3HT HTL and the gold electrode, leading to improved device stability.[7] However, while interface engineering can be effective, it often requires additional processing steps and may introduce complexity, which limits its large-scale applicability. Thus, there remains a strong need for new, low-cost, and efficient additives that can simultaneously improve stability and performance.

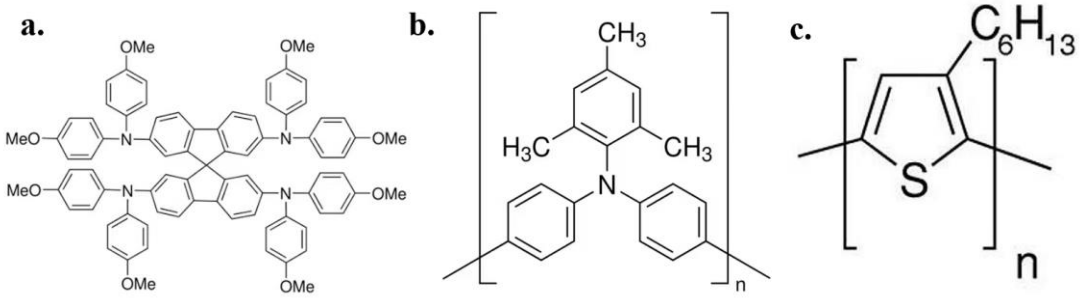

Figure 3.1 Structure of a.Spiro-MeOTAD,b.PTAA and c. P3HT

However, current dopant chemicals such as LiTFSI are expensive and the interface engineering is complex, so new additives are required to create low cost, stable and high-performance devices.

MONs are an emerging class of 2D nanomaterials consisting of organic linkers coordinated with metal ions or metal clusters.[8] MONs have the same high surface area and aspect ratio as other 2D materials, but their modular structure allows for easy and systematic tuning of their electronic, optical, and mechanical properties, as well as the introduction of new chemical functionalities.[9] The planar nature and nanoscopic

dimensions of 2D MONs make them good candidates for integration within thin HTL, providing a more uniform and continuous film that enhances charge transport properties.

Previous studies have also demonstrated that incorporating metal–organic frameworks (MOFs) into HTLs can enhance stability. For example, copper- and cobalt-based 3D MOFs improved PSC stability, with devices retaining 82% of their initial performance after 264 hours in ambient conditions, though the maximum PCE achieved was only 10.4%.[10] However, 3D MOFs often face intrinsic limitations for thin-film device integration: their bulk crystalline nature leads to poor film-forming ability, their electrical conductivity is typically low due to inefficient charge hopping between metal clusters and organic linkers, and their micrometer-scale particles are difficult to uniformly disperse in polymer matrices. As a result, while 3D MOFs can stabilize devices, they rarely deliver significant efficiency gains. These challenges motivate the exploration of 2D MONs, which combine high surface area, tunable electronic properties, and better processability for thin-film applications.

Previously, Foster and co-workers demonstrated the potential of MONs in organic photovoltaics by incorporating Zn_2(ZnTCPP), into P3HT: PCBM blends. The addition of Zn_2(ZnTCPP) doubled the PCE compared to the control devices, which they attributed to improved structural ordering of the semi-crystalline P3HT matrix. This conclusion was supported by GIWAXS measurements that revealed stronger (100) lamellar stacking and enhanced π–π stacking peaks, as well as AFM images showing smoother and more continuous film morphology. Space-charge-limited current (SCLC) measurements further confirmed a significant increase in hole mobility.[11] In a subsequent study using the high-performance PffBT4T2OD: PCBM system, the introduction of Zn_2(ZnTCPP) MONs increased the PCE from 10.6% to 12.3%, which at that time represented the highest reported efficiency for a fullerene-based organic solar cell. In this case, GIWAXS again indicated enhanced crystalline and molecular packing, while transient photovoltage and photocurrent measurements evidenced suppressed recombination and more efficient charge extraction.[12] Together, these

studies provided direct evidence that MONs can act as templates to promote molecular ordering.

Based on the findings of Foster and co-workers, which demonstrated that Zn_2(ZnTCPP) MONs can act as templates to enhance crystallinity and hole transport in semi-crystalline polymers, we hypothesize that incorporating Zn_2(ZnTCPP) nanosheets into the P3HT hole transport material will similarly improve its ordering, film quality, and charge transport properties when used in PSCs. To test this hypothesis, Zn_2(ZnTCPP) nanosheets were synthesized, thoroughly characterized, and blended with P3HT to fabricate composite HTLs. The structural, optical, and electronic properties of these films were systematically investigated using AFM, SEM, UV–Vis absorption, PL quenching, Raman spectroscopy, UPS, and GIWAXS. The photovoltaic performance of PSCs based on these HTLs was then evaluated through J–V measurements, EQE spectra, and stability testing, enabling a direct correlation between material properties and device performance.

The aim of this chapter is to systematically present the synthesis strategy, structural verification, and device integration of Zn_2(ZnTCPP) MONs, followed by an in-depth discussion of their functional role within the PSC architecture. The chapter is structured as follows: first, the top-down synthesis method and relevant optimization steps are described in detail. This is followed by a comprehensive presentation of the characterization results, including morphological, crystallographic, and spectroscopic analyses. Next, the incorporation process of the MONs into the HTL is outlined, with emphasis on processing conditions and interfacial considerations. Finally, the photovoltaic performance data are discussed, highlighting the correlation between the structural features of the MONs and the observed improvements in charge transport and device efficiency.

3.2 Results

3.2.1 Synthesis and characterization of the Zn_2(ZnTCPP) MONs

Zn_2(ZnTCPP) nanosheets were synthesis according to previous method by Sasitharan et al. [11] Briefly, Zn_2(ZnTCPP) nanosheets were synthesized by heating TCPP with zinc nitrate in a DMF:ethanol mixture at 80 °C for 24 h to yield a 3D MOF, which was then exfoliated into 2D MONs by sonication in ethanol. The crystalline phase was confirmed by XRPD, while elemental analysis verified the expected composition of ZnTCPP·6H_2O·DMF. Complementary UV–Vis and FT-IR measurements further confirmed the characteristic electronic transitions and coordination modes of the porphyrinic framework. Taken together, these results demonstrate the successful and reproducible synthesis of Zn_2(ZnTCPP) MONs with well-defined structural and compositional integrity.

To confirm the size and thickness of the synthesized MONs, atomic force microscopy (AFM) measurements were performed on suspensions of 10 µL material deposited onto freshly cleaved mica substrates. As shown in Figure 3.2a, the AFM topography image (5 µm × 5 µm scan area) reveals the formation of well-dispersed, ultra-thin nanosheets with lateral dimensions ranging from 100 to 300 nm. Threeline scans (labeled 1, 2, and 3) were drawn across individual nanosheets to evaluate their thickness. The corresponding height profiles (Figure 3.2b) exhibit sharp step edges with a uniform height of approximately 1–2 nm, confirming that the nanosheets are predominantly monolayer in thickness.

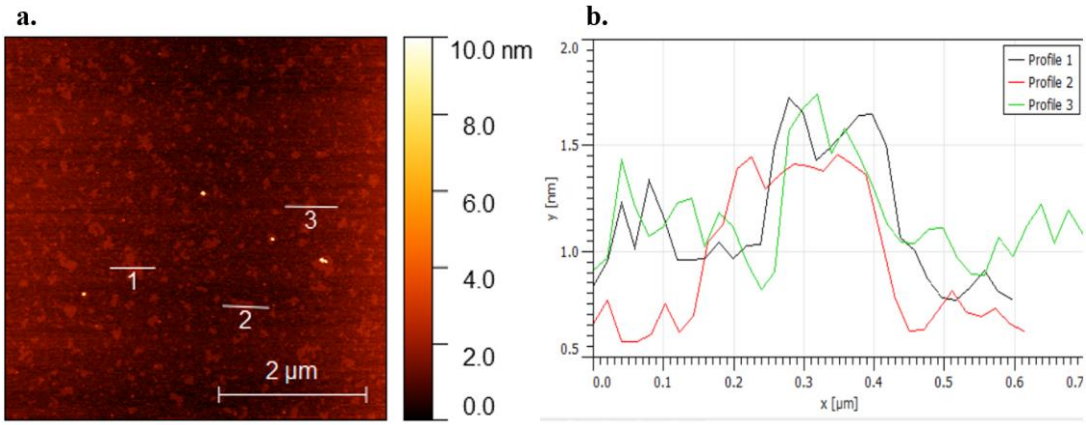

Figure 3.2 AFM characterization of MONs deposited on mica. a,tapping-mode AFM image (5 µm × 5 µm) and b, Height profiles along lines 1–3Three line scans (labeled Profile1, 2, and 3) are marked across individual nanosheets.

The measured thickness of 1-2 nm for the nanosheets is consistent with previous reports.[13]

The crystalline structure of the synthesized 2D Zn_2(ZnTCPP) MONs was confirmed by XRD. Typically, 10 mg of the resulting powder was used for the measurement. The obtained diffraction pattern (Figure 3.3a) is consistent with previous reports [11], indicating the successful formation and structural integrity of the 2D MONs.

The optical properties of the materials were tested by UV-visible spectroscopic measurements of Zn_2(ZnTCPP) MONs in suspension (Figure 3.3b). The results show that they are strongly absorbing, with a characteristic π–π* absorption band at around 435 nm, and Q bands at 564 and 601 nm. Compared with the TCPP ligand precursor, which exhibits four Q bands, the Zn_2(ZnTCPP) MONs display only two Q bands. This simplification is a well-established spectroscopic hallmark of metallated porphyrins, arising from the increased molecular symmetry upon Zn^{2+} coordination at the central site of the TCPP ligands. [13]

Moreover, the Soret band of Zn_2(ZnTCPP) MONs exhibits a pronounced broadening and reduced intensity compared with that of free TCPP, suggesting strong electronic coupling and delocalization within the 2D coordination network. Such broadening is

typically associated with π–π stacking interactions and partial aggregation of porphyrin units in the nanosheet structure. Besides, a slight red shift of the absorption edge is also observed for Zn_2(ZnTCPP) MONs, indicating an extended π-conjugation and reduced optical band gap upon metal coordination.

The reproducibility of the UV-Vis spectral features was found to confirm that the MONs' structure remains consistent across different synthesis batches indicating full-metalation of the porphyrin center in all batches.

The FT-IR spectra of TCPP and Zn_2(ZnTCPP) MONs (Figure 3.3c) further confirm the coordination between Zn^{2+} ions and TCPP ligands. The characteristic C=O stretching vibration of the carboxylic acid groups (–COOH) in TCPP at around 1700 cm^{-1} almost disappears after coordination, while two new bands appear at 1620 cm^{-1} and 1400 cm^{-1}, which are assigned to the asymmetric and symmetric stretching vibrations of the deprotonated carboxylate ($–COO^-$) groups, respectively. The asymmetric carboxylate stretching band at 1620 cm^{-1}, although slightly higher than the typical range for free carboxylates (1550–1610 cm^{-1}), is consistent with a monodentate coordination mode of the $–COO^-$ groups to Zn^{2+} ions, as the Δν value ($\nu_{as} - \nu_{s} = 220$ cm^{-1}) is larger than that of the free carboxylate ion (∼160 cm^{-1}).[14] In addition, the absorption features around 1000 cm^{-1} are attributed to the Zn–N coordination between the metal centers and the porphyrin nitrogen atoms.[15] These spectral changes collectively indicate the successful formation of Zn_2(ZnTCPP) MONs with consistent structural characteristics across batches.

a.

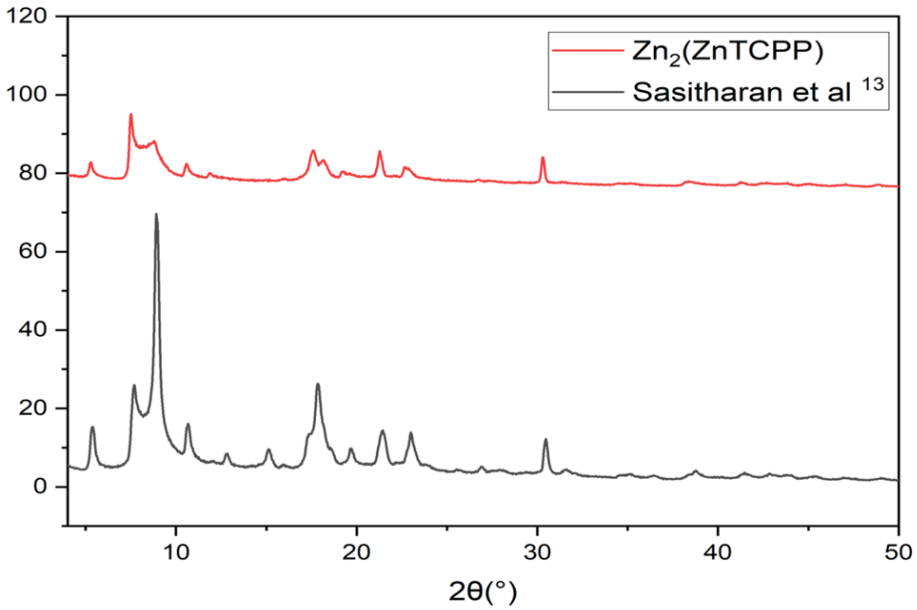
Zn2(ZnTCPP)
Sasitharan et al [13]
120
100
80
60
40
20
0
10
20
30
40
50
2θ(°)

b.

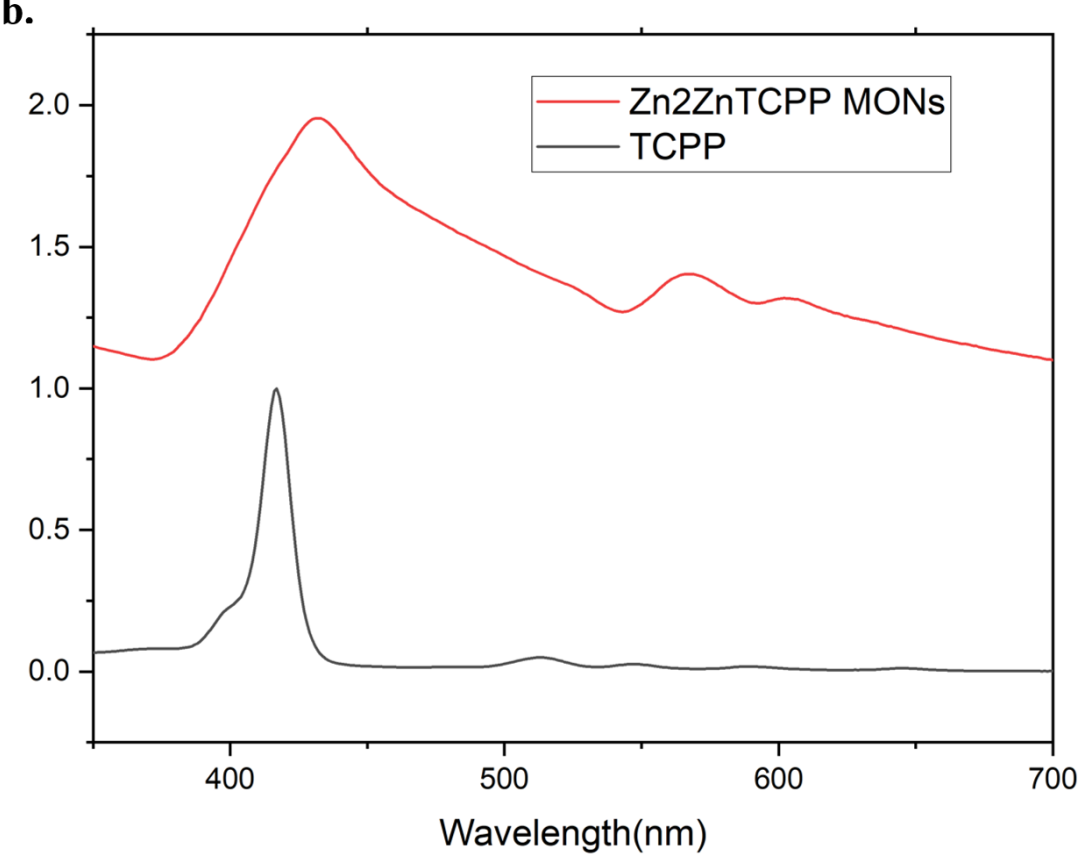
Zn2ZnTCPP MONs
TCPP
2.0
1.5
1.0
0.5
0.0
400
500
600
700
Wavelength(nm)

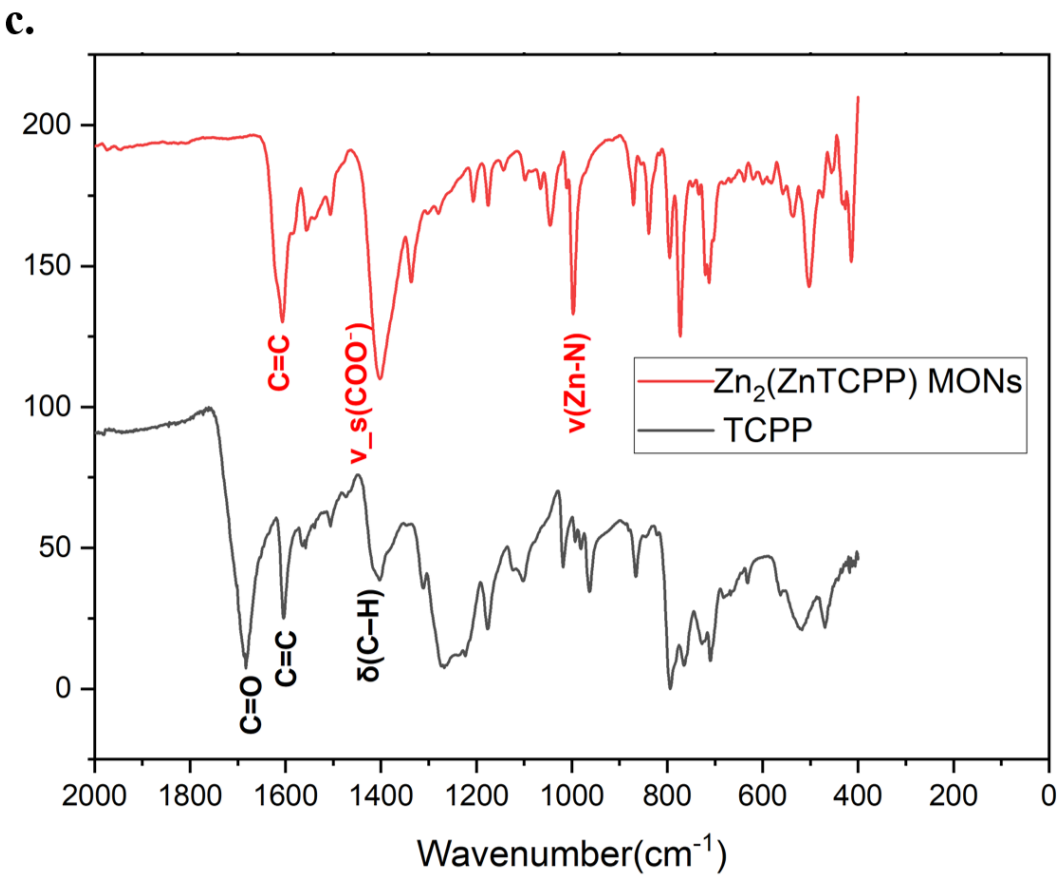

Figure 3.3. Physical characterization of a. XRD for Zn_2(ZnTCPP), b. UV-Vis spectra recorded for TCPP and Zn_2(ZnTCPP) dissolved in ethanol, c. FT-IR for Zn_2(ZnTCPP) MONs powder.

3.2.2 Device fabrication, optimization, and performance

In order to investigate the influence of Zn_2(ZnTCPP) MONs on the photovoltaic performance, various amounts of MONs (1 mg, 5 mg, and 10 mg) were incorporated into P3HT to prepare composite HTLs. The resulting PSCs, with a planar n–i–p configuration of ITO/SnO_2/CsFAPbICl/P3HT with or without MONs/Au (Figure 3.4), were fabricated and tested under simulated AM 1.5 G illumination. The corresponding photovoltaic parameters are summarized in Table 1.

The P3HT: Zn_2(ZnTCPP) (1:0.1 wt%) film achieved an average PCE of 7.90%, while the 1:0.5 wt% ratio gave the best result with a PCE of 9.90%, due to higher V_oc and fill factor. When the MON content increased to 1:1 wt%, the average efficiency slightly

decreased to 8.07%, possibly because of aggregation or poor film uniformity. Therefore, moderate MON loading (1:0.5 wt%) provided the best balance and highest device performance.

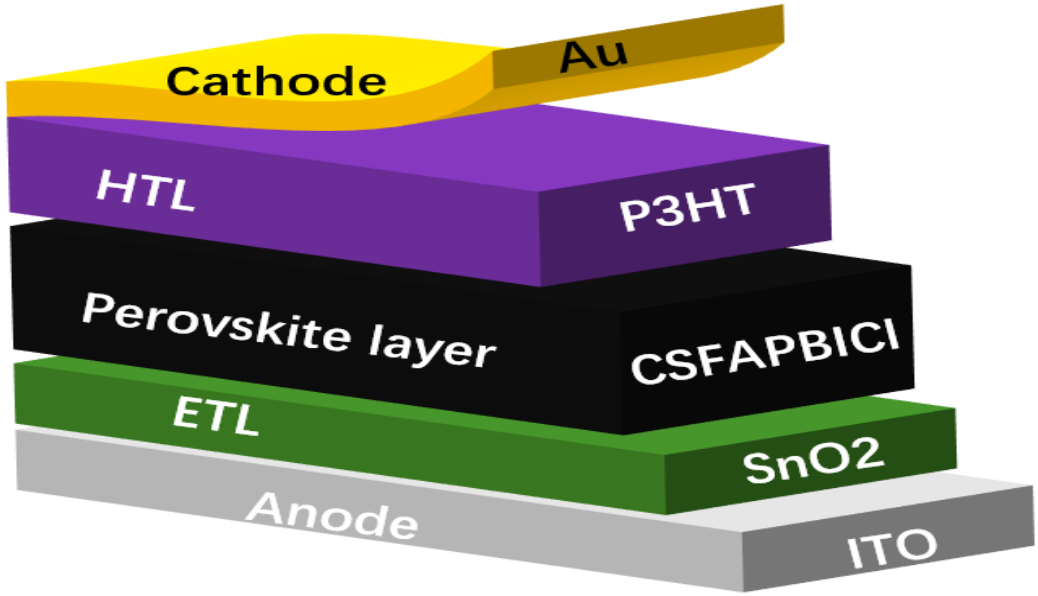

Figure 3.4 Structure of PSCs

As detailed in Table 1, the overall device performance using P3HT as the HTL was lower compared to those based on Spiro-OMeTAD, which is consistent with its relatively limited hole mobility and energy alignment. Initially, Spiro-OMeTAD was selected as the preferred HTL due to its well-established performance in organic and PSCs. However, upon incorporation of the Zn_2(ZnTCPP) MONs into the Spiro-based architecture, a marked decline in device efficiency was observed.

Table 1. Comparative device average performance using Spiro-OMeTAD and P3HT-based HTLs with and without Zn_2(ZnTCPP) MONs

No.	HTL	J_{sc}(mA/cm^2)	V_{oc}(V)	FF(%)	PCE(%)
1	Spiro-OMeTAD [15]	23.40	1.140	80.6	21.51
2	Spiro-OMeTAD: Zn_2(ZnTCPP) (1:0.05 wt%)	7.22±0.24	0.49±0.35	29.43±0.32	1.38+0.23
3	P3HT	17.83±0.386	0.85±0.159	40.12±1.57	6.55±0.16
4	P3HT-TCPP	7.28±0.64	0.51±0.29	36.89±0.10	2.51±0.13
5	P3HT:Zn_2(ZnTCPP) (1:0.1 wt%)	17.45± 0.76	0.94±0.071	47.24±1.4	7.90±0.69
6	P3HT:Zn_2(ZnTCPP) (1:0.5 wt%)	19.02±0.16	1.02±0.21	62.45±0.36	12.11±0.31
7	P3HT: Zn_2(ZnTCPP) (1:1 wt%)	16.96±0.253	0.91±0.310	49.13±0.113	8.07±0.365

As shown in Figure 3.5 and table 1, the incorporation of Zn_2(ZnTCPP) MONs into the P3HT HTL led to marked improvements across all key photovoltaic parameters. For the optimal 1:0.5 wt% ratio of MONs in P3HT, the Jsc increased from 17.83±0.386 mA/cm² (pure P3HT) to 19.02±0.16 mA/cm², reflecting enhanced exciton dissociation and improved charge collection. A more substantial enhancement was observed in Voc, which rose from 0.85±0.159 V to 1.02±0.21V, likely due to reduced interfacial recombination and better energy level alignment induced by MONs. The fill factor (FF) also improved significantly from 40.12±1.57% to 62.45±0.36%, indicating improved transport charge and suppressed non-radiative losses.

As a result, the overall PCE increased from 6.55±0.16% to 12.11±0.31%, almost doubling the output. Notably, this improvement is not limited to isolated cases: as shown in Figure 3.5c., the champion device based on the P3HT:Zn_2(ZnTCPP) (1:0.5 wt%) composite achieved a PCE of 14.8%, significantly higher than 8.27% for the pristine P3HT device. The Voc increased from 0.92 V to 1.06 V, suggesting improved interfacial energetics and suppressed recombination losses. The Jsc also rose from 18.32 mA cm^{-2} to 19.44 mA cm^{-2}, reflecting enhanced exciton dissociation and charge collection. Moreover, the fill factor (FF) exhibited a remarkable increase from 58.61% to 71.52%, indicating more efficient charge transport and reduced non-radiative recombination at the interface. These improvements collectively confirm that the introduction of Zn_2(ZnTCPP) MONs facilitates more balanced charge extraction and improved interfacial contact within the P3HT layer, resulting in superior overall device efficiency.

To ensure that the performance enhancement originated from the incorporation of MONs rather than the organic ligand itself, the same amount of TCPP (5mg) was used as an independent additive for comparison.

The P3HT–TCPP device exhibited a marked decline in all parameters, with a Voc of

0.51±0.29 V, Jsc of 7.28±0.64 mA cm^{-2}, and PCE of only 2.51±0.13%. This significant

degradation indicates that the free TCPP molecules likely disrupt charge transport within the P3HT matrix, creating trap states or energetic disorder that hinder carrier mobility and extraction. In addition, different loadings of MONs were incorporated to investigate the influence of MON content on device performance.

At a low loading of 1:0.1 wt%, the P3HT: Zn_2(ZnTCPP) composite delivered a Voc of 0.94 V and a PCE of 7.90±0.69%, already surpassing pristine P3HT (6.55±0.16%). The improvement is attributed to enhanced energy-level alignment and improved hole transport arising from the delocalized electronic structure of the MONs.

However, excessive loading (1:1 wt%) led to a decline in performance (Voc = 0.91±0.310V, PCE = 8.07±0.365%), which was likely due to partial aggregation of MON nanosheets within the polymer matrix, which impedes charge percolation pathways and increases interfacial recombination. This suggests that an optimal dispersion of MONs is crucial to maintaining balance between interfacial modification and charge transport continuity.

In summary, the comparative analysis demonstrates that the introduction of Zn_2(ZnTCPP) MONs into the P3HT HTL effectively enhances device performance through improved energy-level alignment, charge transport, and interfacial quality. Control experiments using the TCPP ligand alone confirm that the observed improvement originates from the integrated 2D coordination framework rather than the organic ligand itself. The systematic variation in MON loading further reveals a clear composition–performance relationship: moderate incorporation (1:0.5 wt%) achieves optimal dispersion and charge transfer. Overall, the findings highlight the critical role of well-dispersed conductive MONs in facilitating efficient charge extraction and stabilizing interfacial energetics, thereby offering a promising strategy for advancing perovskite solar cell performance.

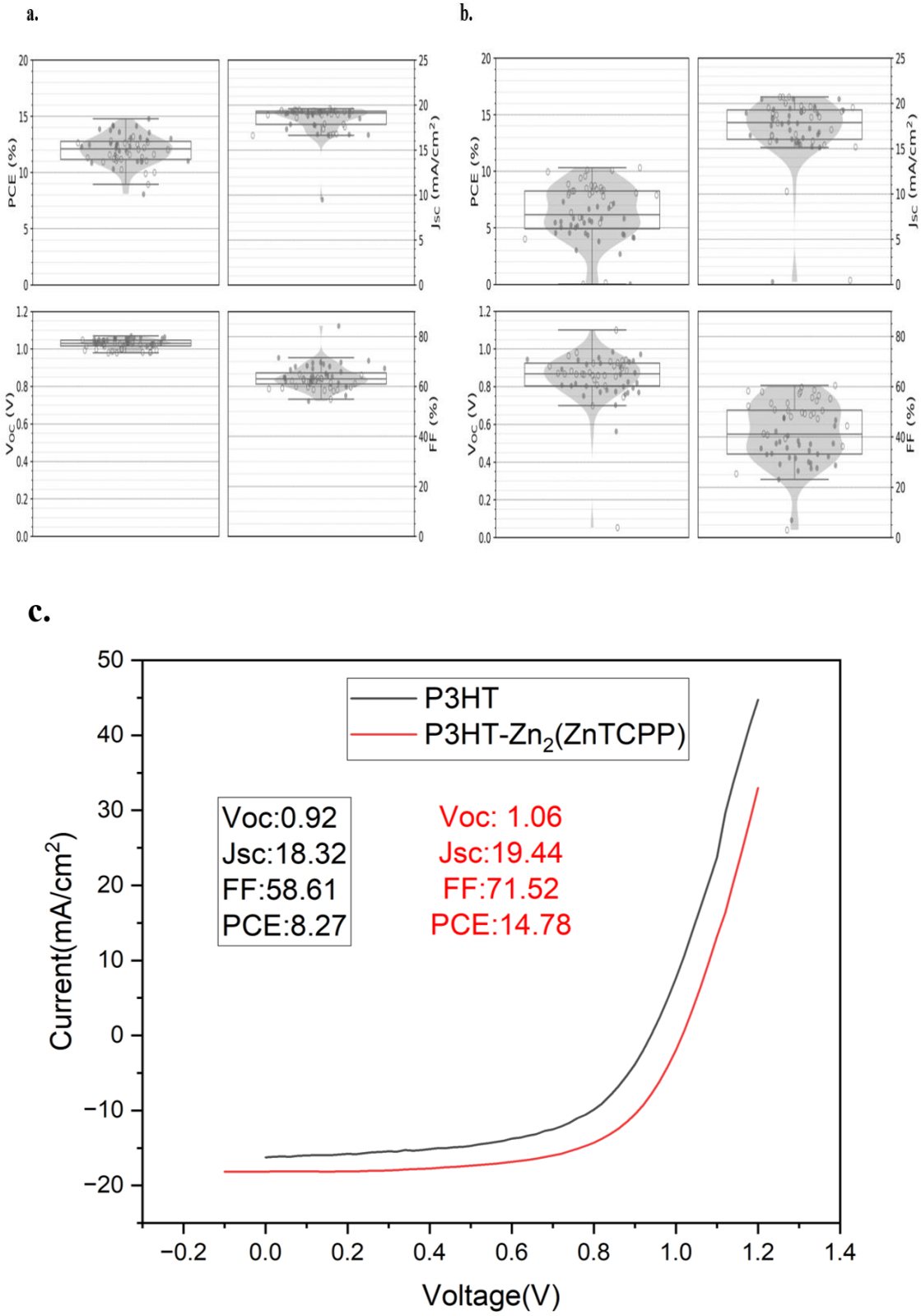

Figure 3.5. Performance of a. P3HT-MONs devices and b. P3HT only devices, the champion devices of c. P3HT-MONs (red curve) device and P3HT only device (black curve)

Furthermore, the external quantum efficiency (EQE) spectra in Figure 3.6 provide additional evidence for the improved photocurrent generation in devices incorporating Zn_2(ZnTCPP) MONs. Compared to the pristine P3HT-based HTL, the MONs-modified devices (1:0.5 wt%) display consistently higher EQE values across the 400–650 nm range, with a particularly notable enhancement in the visible region. This indicates a more efficient photo-to-charge conversion process, potentially linked to improved interfacial charge dynamics or optical modulation introduced by the MONs. Of particular interest is the peak around 450 nm, which coincides with the characteristic Soret band absorption of Zn_2(ZnTCPP) observed in UV–vis spectroscopy. While this spectral overlap does not directly confirm active light harvesting by the MONs, it suggests their possible contribution to the overall optical response of the device. Collectively, these EQE improvements are consistent with the enhanced Jsc and PCE values observed, underscoring the functional role of MONs in boosting device performance.

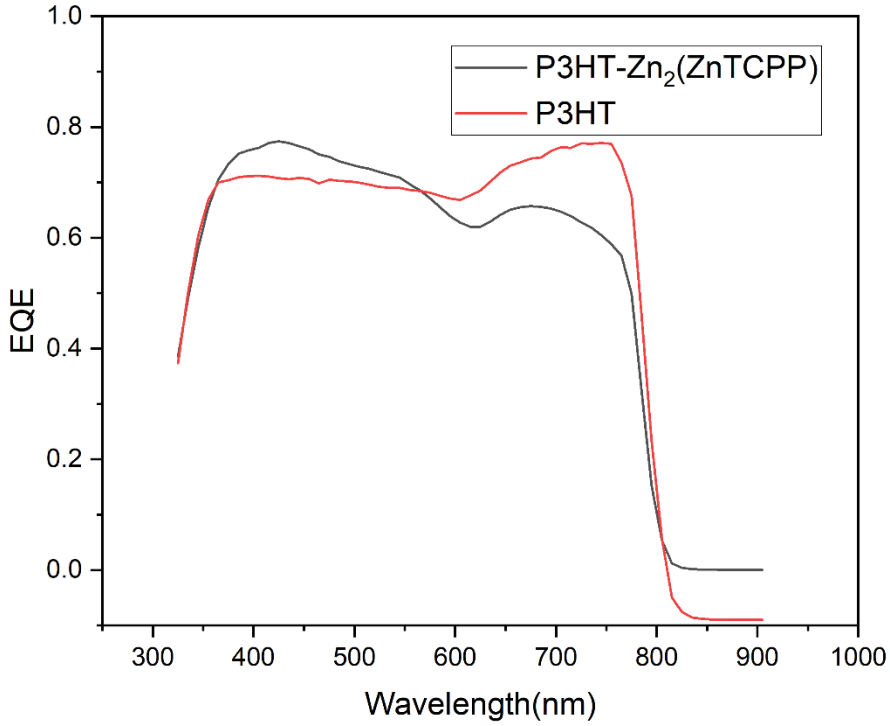

Figure 3.6. EQE spectra of PSCs using P3HT and P3HT: Zn_2(ZnTCPP) MONs (1:0.5) as HTLS.

3.2.2 Discussions on the role of MONs addition into the P3HT Hole transport layer

Scanning electron microscopy (SEM) imaging was carried out on P3HT–Zn_2(ZnTCPP) blend films that were spin-coated onto pre-cleaned ITO glass substrates under the same preparation conditions as those used for the HTL fabrication in devices. Figure 6a and b show SEM micrographs of the pristine P3HT and P3HT–Zn_2(ZnTCPP) films, respectively. The surface of the pristine P3HT film (a) appears smooth and featureless at low contrast, while the P3HT–Zn_2(ZnTCPP) blend film (b) shows a more granular texture, suggesting the presence of well-dispersed MONs. The absence of large aggregates in (b) indicates that Zn_2(ZnTCPP) is uniformly distributed throughout the P3HT matrix.

Atomic force microscopy (AFM) and scanning electron microscopy (SEM) were employed to investigate the morphological effects of Zn_2(ZnTCPP) MON incorporation into the P3HT-based HTL.

As shown in Figure 3.7c and d, AFM analysis revealed a clear reduction in surface roughness at the nanoscale after MONs addition. The pristine P3HT film exhibited relatively large height variations of up to approximately 105 nm, whereas the P3HT:Zn_2(ZnTCPP) (1:0.5 wt%) composite film showed a smoother and more homogeneous surface with height fluctuations reduced to around 80 nm.

This morphological improvement suggests that MONs promote more uniform film formation and enhance the packing order of P3HT chains. The improved surface smoothness likely facilitates stronger interfacial contact with the perovskite layer, thereby reducing interfacial traps and enabling more efficient hole transport across the HTL.

In contrast, the SEM images (Figure 3.7a and 3.7b) reveal an increase in microscale surface heterogeneity in the MONs-containing films, with the appearance of discrete

bright features likely corresponding to partially aggregated or restacked MON domains. The pristine P3HT film appears smoother at this scale, indicating fewer large-scale surface irregularities.

This apparent discrepancy between AFM and SEM observations can be attributed to the difference in probing scales: AFM captures nanoscale topography over a limited area, while SEM reveals microscale morphology over a larger field of view. Together, these complementary techniques suggest that MONs improve the local ordering and uniformity of the HTL at the nanometer scale, while also introducing textural features at the micrometer scale due to partial aggregation. These morphological characteristics may contribute to the observed improvements in device performance.

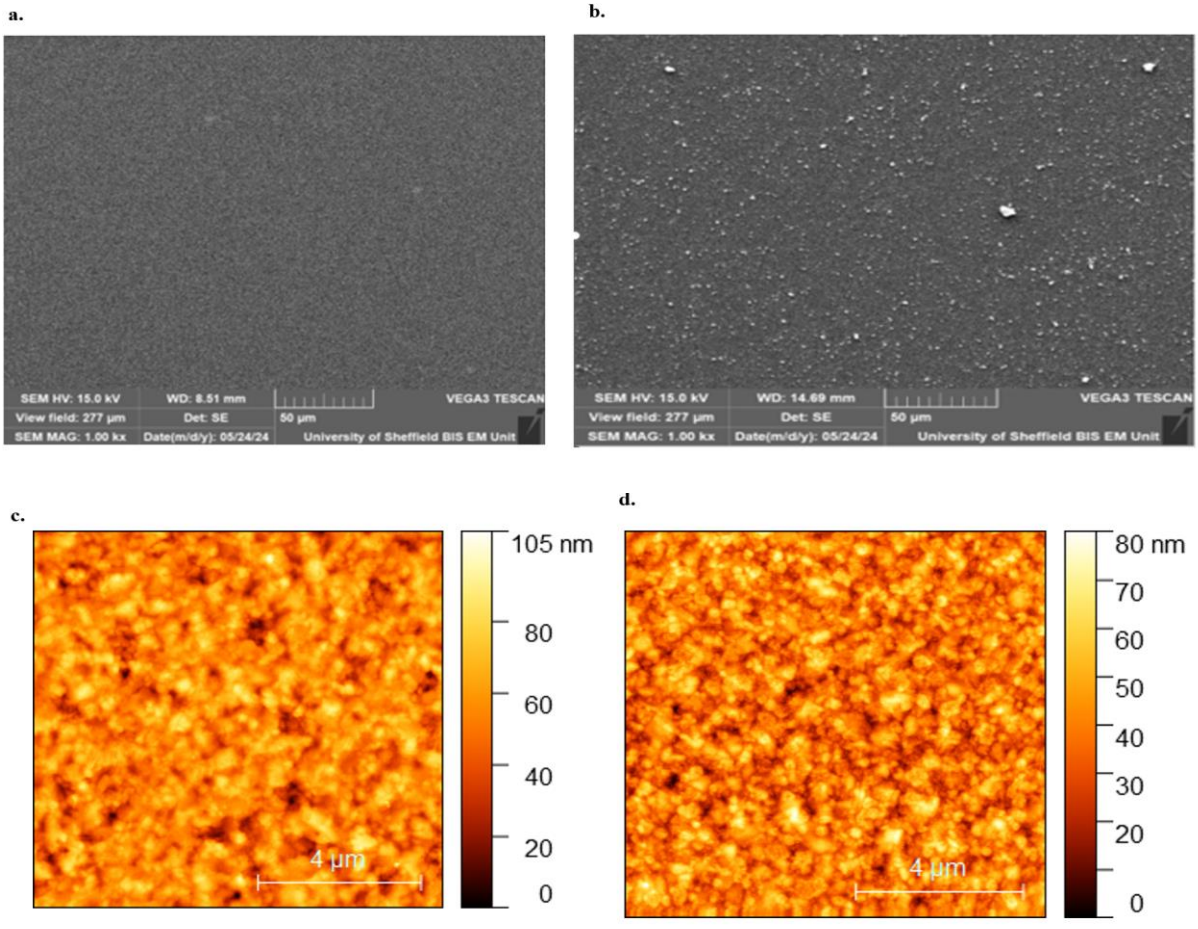

Figure 3.7. SEM image of a. P3HT only layer and b. P3HT-MONs layer, AFM image of c. P3HT layer and d. P3HT-MONs layer.

Figure 3.8a compares the UV–vis absorption spectra of three film configurations: pristine perovskite (PVK), PVK with a P3HT overlayer, and PVK with a P3HT:Zn_2(ZnTCPP) MONs blend. All films were fabricated using the identical layer-by-layer spin-coating procedure employed in device fabrication, ensuring that the optical properties reflect realistic interfacial structures.

The pristine PVK film exhibits the strongest overall absorption across the visible range. The introduction of a P3HT overlayer slightly suppresses the absorption intensity, particularly between 400 and 650 nm. This attenuation is likely attributable to increased optical reflection/scattering at the additional organic–inorganic interface and to partial shielding of the perovskite surface by the semitransparent polymer layer, which collectively reduce the photon flux reaching the active layer.

Notably, the incorporation of Zn_2(ZnTCPP) MONs into the P3HT matrix partially recovers the absorption loss in the 400–500 nm region, where a distinct shoulder emerges around 450 nm. This feature corresponds to the characteristic Soret band of the porphyrin-based framework, confirming that the MONs contributes an additional light-harvesting channel in the high-energy spectral region. Importantly, this selective enhancement does not alter the perovskite absorption onset (located at ~715 nm, corresponding to an optical bandgap of ~1.71 eV S3.7), suggesting that the MONs introduce complementary absorption without compromising the intrinsic band-edge transition of the perovskite.

Figure 3.8b compares the absorption spectra of pristine P3HT and P3HT films incorporating 0.1 wt%, 0.5 wt%, and 1 wt% of Zn_2(ZnTCPP) MONs. With increasing MON content, a slight but discernible rise in absorbance is observed around 450 nm, which can be attributed to the characteristic Soret-band transition of the porphyrin-based framework. Concurrently, a marginal decrease in the 500–600 nm region is evident, likely resulting from the relatively lower extinction coefficients of the porphyrinic species in this spectral range or minor light-scattering effects induced by the MON dispersion within the polymer matrix. Despite these subtle variations, the

overall spectral line shape remains largely unchanged, indicating that the incorporation of MONs does not compromise the optical transparency of the P3HT hole-transport layer.

Taken together, these results demonstrate that while the P3HT overlayer introduces an additional interfacial barrier that reduces visible-light absorption, the inclusion of Zn_2(ZnTCPP) MONs selectively enhances short-wavelength absorption and partially compensates for this loss. This synergistic optical effect may contribute to the observed improvement in J_{sc} in MON-modified devices.

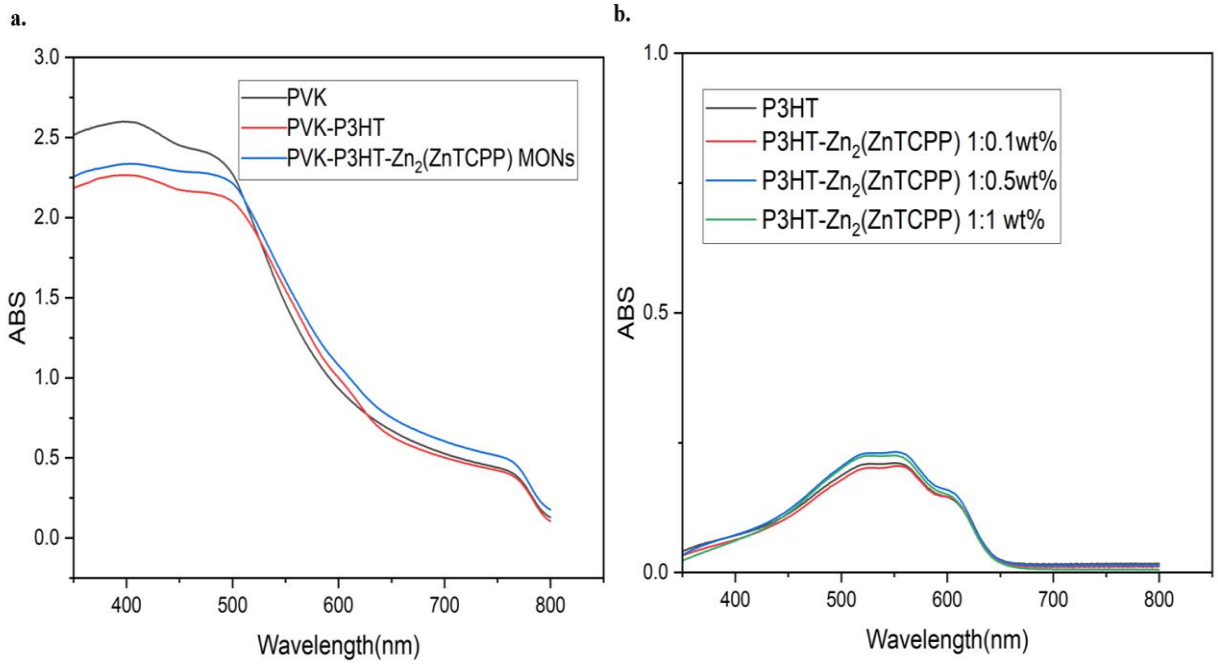

Figure 3.8 Optoelectronic characterizations: a. thin film absorption spectra of pervosikte-P3HT -Zn_2(ZnTCPP), Zn_2(ZnTCPP) MONs dropcast (5 mg ml^{-1}) and dried, b. P3HT and different weight ration of Zn_2(ZnTCPP) MONs spin-coated with chlorobenzene at 3000 rpm with 30 seconds and dried.

Figure 3.9 presents the Raman spectra of pristine P3HT and P3HT–Zn_2(ZnTCPP) MON composite films on ITO glass substrates, recorded with a 532 nm excitation laser at 10% power. Both films exhibit two characteristic peaks at approximately 1380 and 1450 cm^{-1}, assigned to the C–C stretching and C=C symmetric stretching modes of the thiophene rings in the P3HT backbone, respectively. Upon MON incorporation,

no discernible shift in these peak positions is observed, confirming that the Zn_2(ZnTCPP) MONs do not disrupt the conjugation length or molecular conformation of P3HT. This structural integrity is essential for maintaining the hole-transport functionality of the P3HT layer. Notably, a slight increase in the intensity of these characteristic peaks is observed in the composite film, which may tentatively suggest improved molecular ordering or enhanced scattering cross-section upon MON incorporation. However, as no internal standard was employed for intensity normalization, this observation should be interpreted with caution and is discussed only qualitatively. Nevertheless, the unchanged peak positions provide unambiguous evidence that the MONs do not degrade the polymer backbone, ensuring that any improvement in device performance can be attributed to the positive contributions of the MONs rather than to structural alteration of the P3HT matrix.

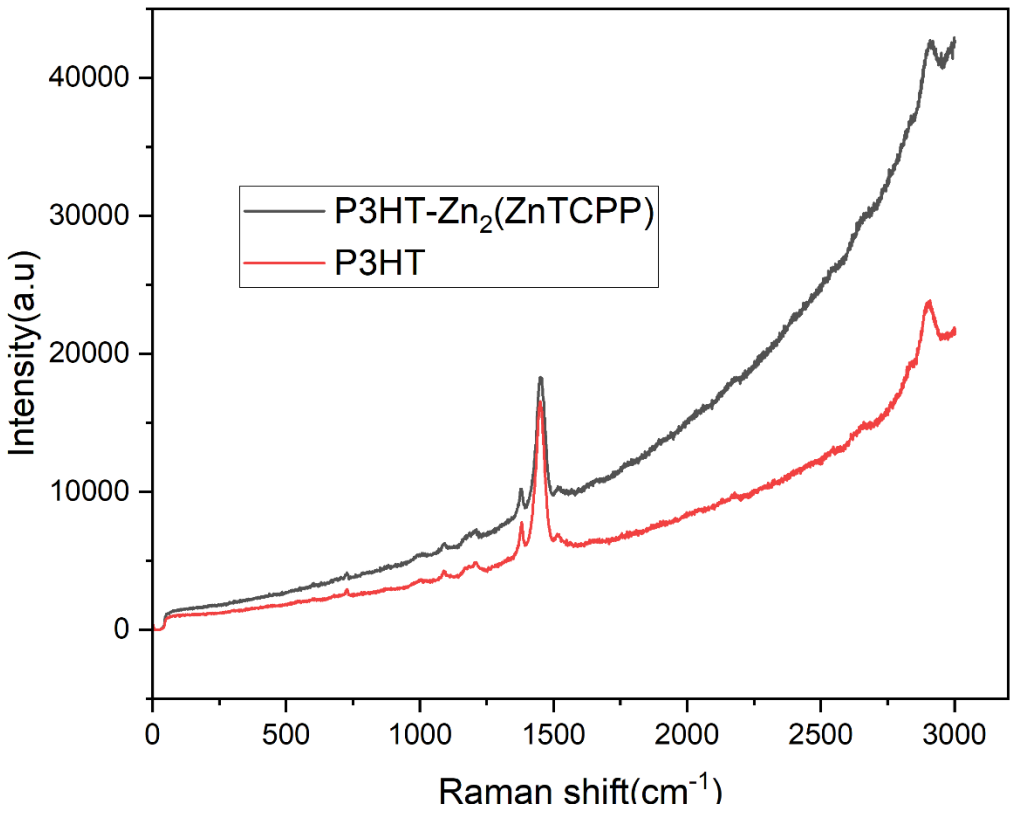

Figure 3.9 Raman Spectra of P3HT only and P3HT-Zn_2(ZnTCPP) MONs (5 mg ml^{-1}) in ITO glasses

Figure 3.10 presents the solid-state photoluminescence (PL) spectra of pristine P3HT and P3HT–Zn_2(ZnTCPP) MON composite films, prepared under identical conditions to those used in device fabrication, to investigate the charge transfer behavior at the HTL. The pristine P3HT film exhibits a strong PL emission peak centered at approximately 650 nm, corresponding to the radiative recombination of photogenerated excitons within the P3HT matrix. In addition, a weaker shoulder is observed at approximately 700 nm, which is characteristic of the vibronic progression of regioregular P3HT.

Upon incorporation of Zn_2(ZnTCPP) MONs, the PL intensity is drastically quenched across the entire emission range, with the quenching efficiency reaching approximately 98% at the peak maximum. This near-complete suppression of P3HT emission indicates efficient photoinduced charge transfer or energy transfer from the P3HT matrix to the MONs, which effectively competes with radiative recombination. It is noteworthy that the residual emission in the composite film exhibits a slightly blue-shifted peak position, suggesting a reduction in P3HT aggregation or a preferential interaction of the MONs with more ordered P3HT domains.

We note that the observed PL quenching could, in principle, be partially influenced by the heavy atom effect of Zn^{2+} within the MONs, which may enhance intersystem crossing and reduce the fluorescence yield of the adjacent P3HT layer. However, the degree of quenching (≈98%) far exceeds what would typically be expected from intersystem crossing alone, and the concomitant improvement in photovoltaic performance (J_{sc} and FF) supports charge transfer as the dominant mechanism. These results demonstrate that Zn_2(ZnTCPP) MONs play a critical role in facilitating exciton dissociation and hole extraction in the composite HTL, consistent with the enhanced device performance observed in J–V and EQE measurements.

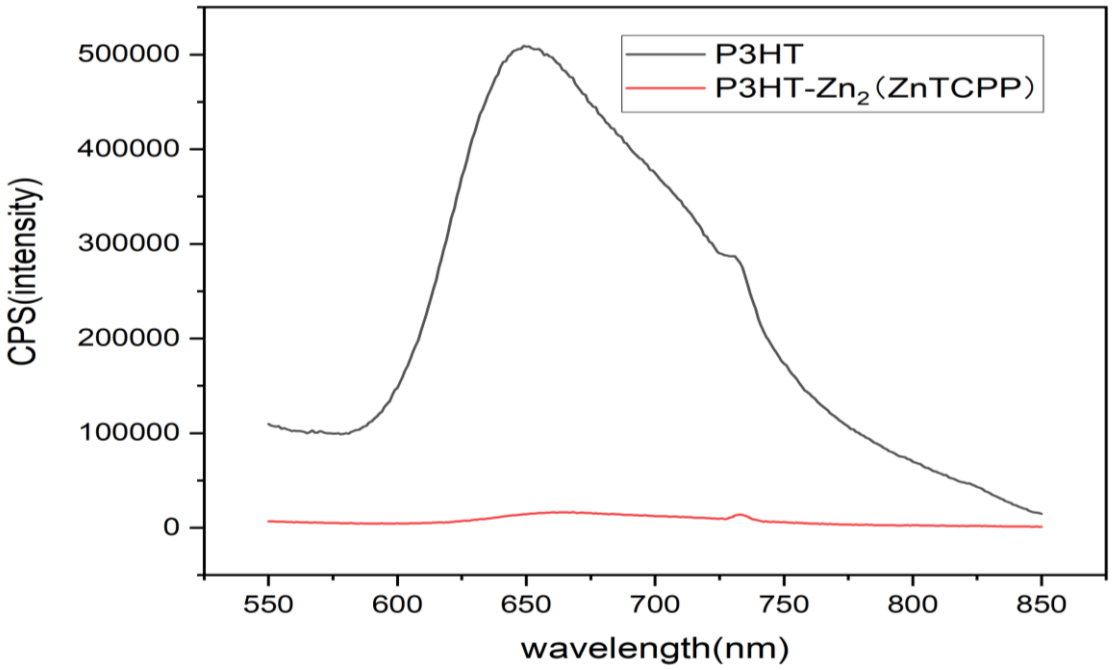

Figure 3.10. Photoluminescence (PL) spectra of thin films of pristine P3HT and P3HT: Zn_2(ZnTCPP) composite.

Upon incorporation of Zn_2(ZnTCPP) MONs, the intensity of both peaks increases and the full width at half maximum (FWHM) decreases slightly, indicating narrower, sharper peaks. This spectral sharpening suggests a higher degree of molecular ordering and improved π–π stacking interactions in the P3HT chains [17] likely facilitated by interactions with the 2D porphyritic MON framework. Such structural reorganization implies enhanced crystallinity and planarity of the P3HT domains. Improved crystallinity of the HTL is often associated with better charge mobility and reduced trap density. Enhanced charge carrier transport and defects mitigate of passivation layer for efficient PSCs which can explain the observed enhancement in the FF of the corresponding devices. These findings reinforce the beneficial role of Zn_2(ZnTCPP) MONs in improving the crystallinity.

To investigate the impact of Zn_2(ZnTCPP) MON doping on the electronic structure of the HTL, ultraviolet photoelectron spectroscopy (UPS) was conducted on three different thin films: pristine PVK, pure P3HT, and P3HT doped with Zn_2(ZnTCPP) MONs. All films were spin-coated onto pre-cleaned ITO glass substrates using the same

deposition conditions as those employed in the fabrication of photovoltaic devices, ensuring consistency and relevance of the measured electronic properties.

Figure 3.11 presents the UPS spectra and corresponding energy level analysis for the three configurations. Figure3.10a shows the full-range spectra, while Figure 3.10b highlights the high binding energy region used to determine the secondary electron cutoff. Based on these cutoff values, the work function and HOMO levels were calculated. The HOMO energy levels were determined using the following formula:

$$E_{HOMO} = h\nu - (E_{cutoff} - E_{onset})$$

where $h\nu$ is the photon energy (21.22 eV for the Helium plasma source), E_{cutoff} is the secondary electron cutoff, and E_{onset} is the HOMO onset derived from the low binding energy region.

Figures 3.11c–3.10e present the secondary electron cutoff regions of perovskite (PVK), P3HT–Zn_2(ZnTCPP) MONs, and pristine P3HT thin films, respectively, extracted from the full-range spectra shown in Figure 3.10a. The cutoff regions are shown with an expanded Y-axis to clearly resolve the subtle differences in cutoff positions among the samples, as these features would be compressed and indistinguishable on the full-scale plot. This magnification does not alter or distort the spectral features—it merely enhances visual clarity in the region of interest, which is standard practice in UPS analysis for determining work functions and HOMO levels. The full-range spectra in Figure 3.10a remain available for reference, ensuring complete transparency of the original data.

Discernible differences in the secondary electron cutoff positions are observed among the three samples. The cutoff onset of the P3HT–MONs composite (2.10 eV) shifts toward higher binding energy relative to pristine P3HT (1.57 eV), indicating a reduced work function upon MON incorporation. For PVK, the cutoff appears at 0.87 eV, consistent with its lower work function. For P3HT and P3HT–MONs, the cutoff onsets are well resolved, allowing reliable determination of the work function and

HOMO levels by linear extrapolation of the steepest slope to the baseline. For PVK, the onset is less distinct owing to a more gradual slope transition, which introduces slightly greater uncertainty; nevertheless, the extracted value is consistent with literature reports for similar perovskite compositions.

A subtle shoulder is observed near the cutoff region in the P3HT–MONs spectrum, which may reflect a minor density-of-states contribution from the porphyrin framework. This feature does not interfere with the main cutoff determination.

The extracted HOMO levels are summarized in Table 3. The HOMO level of the MON-doped P3HT layer is -5.22 eV, which is closer to that of the perovskite (-5.45 eV) than pristine P3HT (-5.10 eV), corresponding to a reduced energetic offset from 0.35 eV to 0.23 eV upon MON incorporation. This improved energy alignment minimizes the interfacial barrier for hole transfer, consistent with the enhanced J_{sc} and FF observed in MON-modified devices.

Table 3 the HOMO energy levels of different thin films

Thin film	HOMO energy level
$CSFAPbCl_{0.3}I_{0.7}$	-5.45 eV
P3HT-MONs	-5.22 eV
P3HT	-5.10 eV

These results indicate that the HOMO level of the MON-doped P3HT layer is closer to that of the perovskite absorbing layer compared to pristine P3HT. This improved energy alignment is beneficial for hole extraction, as it minimizes the energetic offset and reduces interfacial energy barriers. Consequently, charge transfer at the perovskite/HTL interface becomes more efficient, which is likely to enhance overall device performance.

In summary, the UPS analysis confirms that Zn_2(ZnTCPP) MON incorporation not only tunes the morphological characteristics of the P3HT layer (as shown in previous figures) but also optimizes the electronic structure, thereby facilitating more effective hole extraction from the perovskite layer.

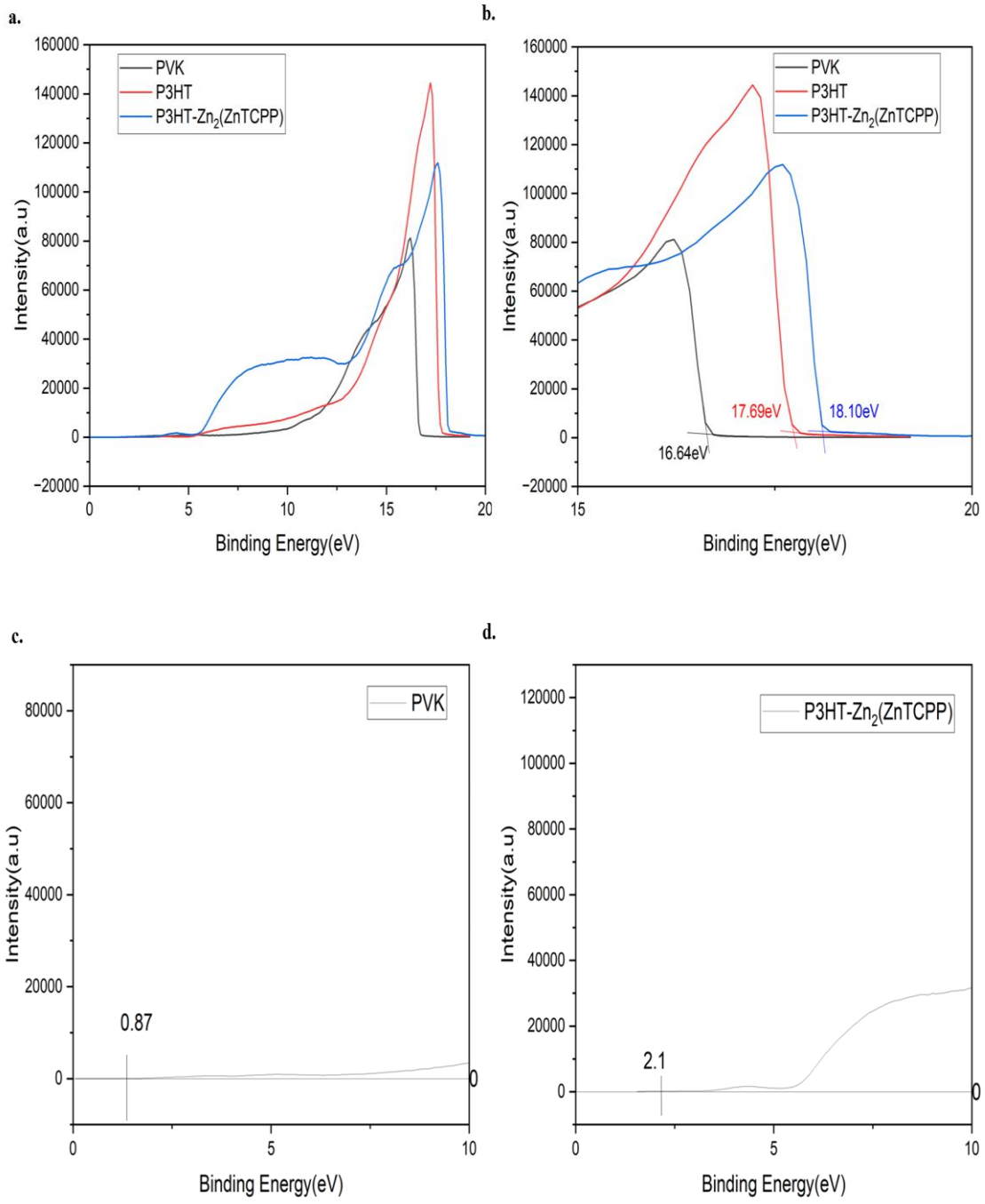

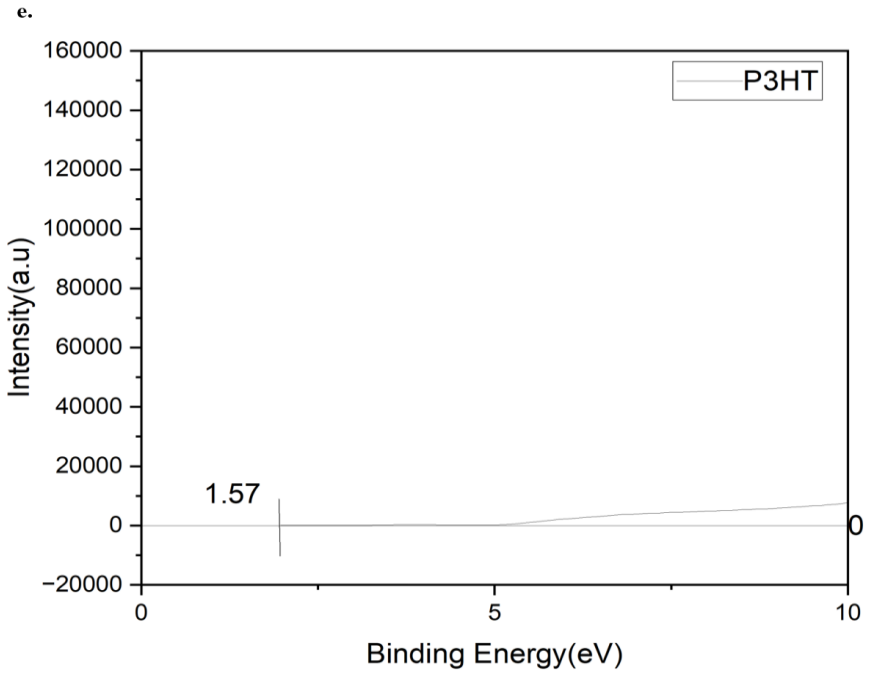

Figure 3.11 a. Full UPS spectrum for Perovskite, P3HT-MONs, and P3HT only thin film b. High binding energy area for Perovskite, P3HT-MONs, and P3HT only thin film, c.-e. low binding energy area for Perovskite, P3HT-MONs and P3HT respectively.

To elucidate the structural influence of Zn_2ZnTCPP MONs doping on P3HT molecular organization, Grazing-Incidence Wide-Angle X-ray Scattering (GIWAXS) measurements were performed in both out-of-plane and in-plane directions. Used the same preparation step of HTL to make the thin film for the GIWAXS test. With Figure 3.12a we can see that the low-Q region (approximately 0.4 $Å^{-1}$), a prominent diffraction peak was observed in the composite films, corresponding to the (100) lamellar stacking of P3HT, which reflects the ordered arrangement of side chains. Compared with pristine P3HT, the P3HT-Zn_2(ZnTCPP) composite exhibited a significantly stronger (100) peak, indicating that the incorporation of Zn_2(ZnTCPP) MONs effectively enhances the lamellar ordering of P3HT.

Around Q≈1.5 $A^{\circ-1}$, a characteristic π–π stacking diffraction peak of P3HT was also observed. The increased intensity of this peak in the composite film suggests stronger or more ordered π–π interactions between aromatic backbones, which may facilitate

more stable charge transport pathways and contribute to improved carrier mobility.

In the out-of-plane GIWAXS patterns, a broad diffuse scattering band spanning Q=0.8∼1.3 $A^{\circ -1}$ is exclusively observed for the P3HT-Zn_2(ZnTCPP) composite film, whereas no prominent diffraction hump appears in this scattering region for the neat P3HT reference sample. Combined with powder XRD characterization of pristine Zn_2(ZnTCPP), this broad scattering signal is perfectly consistent with the diffraction range corresponding to the semi-crystalline ordered domains of porphyrin-based two-dimensional nanosheets, verifying that such diffuse scattering originates from short-range ordered Zn_2(ZnTCPP) nanocrystalline domains dispersed within the P3HT polymer matrix. Neat P3HT only presents two characteristic diffraction peaks assigned to the (100) alkyl lamellar stacking and interchain π–π stacking of conjugated backbones, and it contains no intermediate-scale ordered structures that could produce scattering signals in this Q range, further excluding signal interference from the polymer host. This result directly demonstrates that Zn_2(ZnTCPP) MONs retain their intrinsic ordered structural features in the blended film rather than being randomly and completely dispersed. While elevating the inherent packing order of P3HT, the incorporated nanosheets introduce brand-new ordered domains inside the film, which simultaneously modulates the thin-film micromorphology and charge-transport properties.

Besides, the GIWAXS analysis reveals that the π–π stacking peak is significantly more intense in the out-of-plane direction (Q ≈ 1.47 $Å^{-1}$), while it is weak or negligible in the in-plane profile. This indicates that the aromatic backbones of P3HT predominantly adopt a face-on orientation relative to the substrate, which is favorable for vertical charge transport in perovskite solar cell devices.

Calculate the distance using the formula $d = \frac{2\pi}{Q}$ to Further analysis of GIWAXS patterns revealed two characteristic diffraction peaks in both pristine P3HT and P3HT-Zn_2(ZnTCPP) composite films, corresponding to the (100) lamellar stacking of alkyl side chains and π–π stacking between conjugated backbones. In the pristine P3HT film,

the (100) peak appeared at Q=0.3906 $A^{\circ -1}$, corresponding to an interlayer spacing of d=16.09 A˚, while the π–π stacking peak was located at Q=1.47 $A^{\circ -1}$, yielding a π–π distance of d=4.27 A˚, consistent with typical semicrystalline polymer features. Upon incorporation of Zn_2(ZnTCPP), the (100) peak slightly shifted to Q=0.39 $A^{\circ -1}$ with a calculated spacing of d=16.11 A˚, suggesting that the overall lamellar periodicity remains unchanged, although the crystallinity may be enhanced. The π–π stacking peak remained unchanged in position, yet exhibited higher intensity, indicating stronger and more ordered face-on π–π interactions. This improvement in molecular ordering along the out-of-plane direction is likely to facilitate more efficient vertical hole transport, supporting the role of Zn_2(ZnTCPP) as a structural and electronic modulator in HTL applications.

In the in-plane GIWAXS profiles (Figure 3.12b), the P3HT-Zn_2(ZnTCPP) composite film shows a significantly intensified diffraction peak at Q≈0.53 $A^{\circ -1}$, which corresponds to the (100) lamellar stacking of P3HT side chains. This suggests enhanced in-plane ordering of the polymer chains upon incorporation of Zn_2(ZnTCPP), possibly due to templating or structural induction by the 2D MONs. Meanwhile, the π–π stacking peak around Q≈1.5 $A^{\circ -1}$ does not exhibit notable enhancement in the in-plane direction, implying that π–π interactions remain preferentially oriented out-of-plane. These observations confirm that the composite maintains a face-to-molecular orientation, with enhanced lamellar ordering parallel to the substrate, favoring vertical hole transport in device applications.

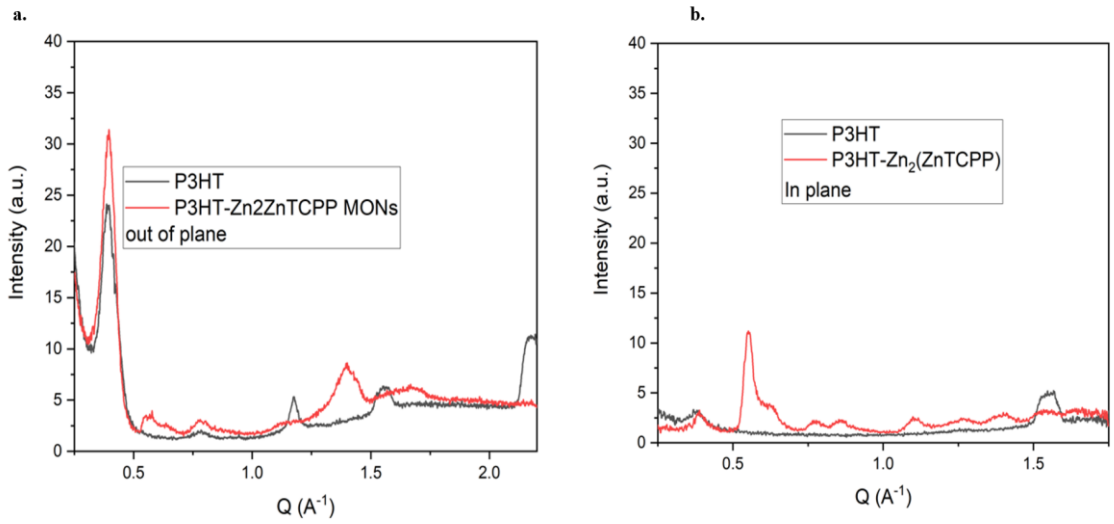

Figure 3.12 a. Out of plane GIWAXS patterns of pristine P3HT and P3HT-Zn_2(ZnTCPP) composite films in ITO glasses, b. In plane GIWAXS patterns of pristine P3HT and P3HT-Zn_2(ZnTCPP) composite films in ITO glasses

3.3 Discussion

The incorporation of Zn_2(ZnTCPP) MONs into the P3HT-based HTLs significantly enhances the performance of PSCs. Morphological characterization by SEM and AFM reveals that the addition of MONs leads to a more homogeneous and compact P3HT film with reduced surface roughness.

The optical properties of the MONs also contribute positively to device performance. UV-vis absorption spectra of Zn_2(ZnTCPP) MONs display a strong Soret band near 435–450 nm and Q bands at 564 and 601 nm. When embedded in the P3HT matrix, this strong absorption around 450 nm is retained and reflected in the EQE spectra of the solar cells. The MON-containing devices show enhanced external quantum efficiency particularly in the 400–650 nm region, suggesting that MONs not only improve the film morphology but also assist in light harvesting and carrier generation, especially near their intrinsic absorption peaks. This additional absorption in the visible region likely contributes to the observed increase in short-circuit current density (Jsc).

Moreover, Raman spectroscopy confirms that the Zn_2(ZnTCPP) MONs do not disrupt

the conjugation length or molecular conformation of P3HT, thereby preserving the structural integrity and hole-transport functionality of the HTL. Although a slight increase in Raman peak intensity is observed upon MON incorporation, the absence of an internal standard precludes quantitative interpretation of this variation. Nevertheless, the unchanged peak positions ensure that the improved device performance can be attributed to the positive contributions of the MONs rather than to any structural degradation of the P3HT matrix.

Energy-level alignment also plays a critical role. UPS measurements show that the HOMO level of the P3HT: MONs film (–5.22 eV) is closer to the HOMO of the perovskite absorber (–5.45 eV) than that of pristine P3HT (–5.10 eV), suggesting better energetic matching for hole extraction. This improved alignment reduces the energy offset at the HTL/perovskite interface and facilitates more efficient hole transfer, as reflected in the improved Voc and reduced hysteresis in J-V characteristics.

PL analysis provides further evidence for enhanced charge transfer dynamics. The steady-state PL spectra show strong emission from pristine P3HT centered around 670 nm, corresponding to radiative recombination of photo-generated excitons. In contrast, the PL emission is significantly quenched in the P3HT: Zn_2(ZnTCPP) films, indicating efficient exciton dissociation and suppressed recombination at the interface. This pronounced PL quenching aligns well with the observed improvements in Voc and Jsc, supporting the hypothesis of enhanced interfacial charge separation facilitated by MONs.

Taken together, these complementary analyses demonstrate that Zn_2(ZnTCPP) MONs not only modulate film morphology and molecular ordering but also improve interfacial energetics and charge transfer properties. Their incorporation into the P3HT HTL enables simultaneous improvements in J_{sc}, V_{oc}, FF, and PCE, highlighting their potential as multifunctional additives for next-generation perovskite solar cell architectures.

3.4 Conclusion

This chapter has successfully achieved its aim of systematically elucidating the synthesis, characterization, and device application of Zn_2(ZnTCPP) MONs as multifunctional additives in polymeric HTLs. Through the top-down synthesis route, high-quality, ultrathin nanosheets were obtained and structurally verified via comprehensive morphological, crystallographic, and spectroscopic analyses. Their incorporation into the P3HT matrix was shown to enhance film uniformity, molecular ordering, and interfacial contact with the perovskite layer, thereby improving charge extraction and transport.

The work revealed that the MONs not only broaden light absorption in the short-wavelength region but also optimize energy-level alignment within the HTL/perovskite interface. And enhance the crystallinity of the semi-crystalline polymer HTL. As a result, photovoltaic performance significantly improved, with device efficiencies increasing from 6.55±0.16% for pristine P3HT-based devices to 12.11±0.31% for P3HT: MON (1:0.5) compositions, and up to 14.8% in fully optimized architectures.

In broader significance, this work represents the first demonstration of directly incorporating 2D porphyrin-based MONs into a semi-crystalline polymeric HTL, establishing an effective strategy for interfacial and electronic optimization in PSCs. It thereby contributes to the expanding body of research on MOF-engineered interlayers aimed at enhancing both the efficiency and operational stability of next-generation photovoltaic devices.

3.5 Materials and Methods Precursor materials preparation

Materials

Lead iodide (PbI_2, 99.99%), lead chloride ($PbCl_2$, 99.99%), caesium iodide (CsI), formamidinium iodide (FAI), anhydrous dimethylformamide (DMF, 99.99%), and chlorobenzene (CB) were all purchased from Sigma-Aldrich. Tris(4-chlorophenyl)

porphyrin (TCPP) was obtained from Insight Biotechnology. Zinc nitrate was obtained from Thermo Scientific. Ethanol and high-purity DMF (for HPLC) were obtained from Sigma-Aldrich, while isopropanol (IPA) was the same sourced. Hellmanex III (HEX) was purchased from Ossila. Tin oxide colloidal dispersion (15% in H_2O) was obtained from Alfa Aesar.

Characterization Equipment

Spin Coating: Performed using an Ossila spin coater with a multiple-substrate chuck. Different spin-coating parameters were employed depending on the specific layer being deposited. For instance, the perovskite, HTL (P3HT or P3HT–MON composites), and ETL (SnO_2) layers were each fabricated under optimized speed and duration conditions to achieve uniform thickness and desired film morphology.

X-ray Diffraction (XRD): X-ray powder diffraction patterns were obtained using a Bruker D8 Advance diffractometer equipped with a Cu Kα radiation source (λ = 1.5418 Å), operated at 40 kV and 40 mA. The diffraction data were collected over a 2θ range of 3–50° with a step size of 0.02°. Approximately 5–10 mg of the MON powder sample was evenly spread on a low-background sample holder for measurement.

UV-Vis Spectroscopy: Absorption spectra were recorded using a Cary 5000 UV-Vis-NIR spectrometer with a 1 cm path length quartz cuvette. The samples were prepared as 1 mg mL^{-1} solutions and measured in absorption mode over a wavelength range of 300–800 nm. The obtained spectra were processed and analyzed using Origin software to evaluate the optical absorption characteristics and spectral features of the MONs.

Atomic Force Microscopy (AFM): Morphological characterization was carried out with a Bruker Multimode 5 AFM operating in soft tapping mode under ambient conditions using a Bruker OTESPA-R3 cantilever. For sample preparation, 20 μL of a 1 mg mL^{-1} solution was drop-cast onto freshly cleaved mica substrates, followed by gentle heating to rapidly evaporate the solvent and form uniform thin films. Image processing and surface roughness analysis were performed using Gwyddion software.

Raman Spectroscopy: Raman spectra of the hole transport layer were recorded using a Horiba XploRA Plus Raman spectrometer in the range of 300–3200 cm^{-1}, with a spectral resolution of 1.4 cm^{-1}, using a 532 nm laser at 10% intensity (~25 mW). The films were prepared under the same spin-coating conditions as those used for device fabrication by depositing 50 µL of a 10 mg mL^{-1} P3HT solution, either in its pristine form or containing 5 mg of Zn_2(ZnTCPP) MONs, followed by spin coating at 5000 rpm for 30 s to ensure identical thickness and morphology to the HTL used in the devices.

Ultraviolet Photoelectron Spectroscopy (UPS): A Kratos Axis Supra instrument equipped with a monochromated Al Kα source (21.22 eV) was used to determine the surface energy levels of the hole transport layer. The samples were fabricated under identical spin-coating conditions to those applied in device preparation by dispensing 50 µL of a 10 mg mL^{-1} P3HT solution, with or without 5 mg of Zn_2(ZnTCPP) MONs, and spin-coated at 5000 rpm for 30 s. These conditions ensured the formation of films with comparable thickness and surface morphology to the HTLs used in the photovoltaic devices.

Solar Simulation and J–V Characterization: A Newport 92251A-1000 solar simulator (AM 1.5G, 1000 W m^{-2}) was used with a silicon reference cell. The active area was defined using a matte black mask with a 2.385 mm^2 aperture. Current–voltage characteristics were measured using a Keithley 237 source meter, with a bias sweep from 0 to 1.2 V at a rate of 0.2 V s^{-1}. Devices were contacted using a probe station.

Grazing-incidence wide-angle X-ray scattering (GIWAXS): using a Bruker Nanostar instrument and an Excillum MetalJet liquid gallium X-ray source equipped with a Dectris Pilatus 1M pixel detector. The system operates with Ga Kα radiation and covers a q-range of 0.001–4.0 $Å^{-1}$. The films were prepared under identical spin-coating conditions to those used for device fabrication by dispensing 50 µL of a 10 mg mL^{-1} P3HT solution, either pristine or blended with 5 mg of Zn_2(ZnTCPP) MONs, and spin-coated at 5000 rpm for 30 s. This ensured that the structural ordering and orientation information obtained from GIWAXS corresponded directly to the HTL films used in

the devices.

Photoluminescence (PL) spectra: were recorded using a Fluoromax-4 spectrofluorometer (Horiba) to investigate the optical emission properties. The excitation wavelength was set to 488 nm, with an excitation slit width of 5 nm. Emission data were collected in the 500–850 nm range with an emission slit width of 5 nm and an increment step of 1 nm. The films were prepared using the same spin-coating parameters as those applied for device fabrication, by depositing 50 µL of a 10 mg mL^{-1} P3HT solution, either pristine or containing 5 mg of Zn_2(ZnTCPP) MONs, and spin-coated at 5000 rpm for 30 s. During measurement.

Synthesis and physical characterization of Zn_2(ZnTCPP) MONs

Zn_2(ZnTCPP) metal-organic nanosheets (MONs) were synthesized via a modified method based on work by Sasitharan et al.7. Briefly, H_2TCPP (79 mg, 0.3 mmol), $Zn(NO_3)_2 \cdot 3H_2O$ (89 mg, 0.9 mmol), DMF (15 mL), and ethanol (5 mL) were mixed and heated at 80 °C for 24 h. The resulting purple crystals were collected by centrifugation at 4500 rpm for 10 min and washed with ethanol until the supernatant was clear (yield: 87%).

To exfoliate Zn_2(ZnTCPP) MOF into 2D MONs, 20 mg of the MOF was dispersed in 4 mL of ethanol using a vortex mixer for 30 s. The mixture was sonicated for 60 min in a Fisherbrand Elmasonic P 30H bath (80 kHz, 100% power, 16–20 °C) using sweep mode, while continuously stirred with an overhead stirrer. The suspension was then centrifuged at 1500 rpm for 10 min to remove unexfoliated materials.

Structural and optical characterization of the 2D MONs was performed using a series of techniques. XRD was conducted on 10 mg of dried MONs using a scan range of 0–50° (2θ) to verify the crystalline structure.

UV–visible absorption spectra were obtained by dispersing 1 mg of MONs in 10 mL of ethanol and measuring in absorbance mode over a wavelength range of 300–800 nm.

FT-IR spectra of Zn_2(ZnTCPP) MONs were recorded using a Bruker Tensor II spectrometer in the range of 400–4000 cm^{-1} with a spectral resolution of 2 cm^{-1}. The samples were prepared by allowing the as-synthesized Zn_2(ZnTCPP) dispersion to dry naturally in air, after which approximately 1 mg of the dried material was used for transmission measurements. The obtained spectra were analyzed to identify the characteristic vibrational modes of the porphyrin framework and the coordination features of Zn^{2+} ions with TCPP ligands, confirming the successful formation of the Zn_2(ZnTCPP) structure.

Fabrication of Perovskite Solar Cells

Substrate Cleaning

The substrates were first boiled in deionized (DI) water and ultrasonicated for 10 minutes, followed by ultrasonication in a 1:10 (v/v) mixture of hexane (HEX) and DI water for another 10 minutes at 37 kHz and 100% power. Afterward, they were rinsed with DI water and isopropanol (IPA) and subjected to the same sonication steps. Finally, the substrates were dried with nitrogen gas and treated with UV-ozone (UVO) for 20 minutes.

Electron transport layer (ETL)

The ETL solution was prepared by mixing 500 μL of SnO_2 colloidal dispersion with 2000 μL of deionized water. After storage in the refrigerator, the solution was spin-coated (50 μL) onto the cleaned ITO substrate at 3000 rpm for 30 s, followed by annealing at 150 °C for 30 min. UVO treatment was applied to the coated substrates for 15 min before further processing.

Perovskite Layer

Perovskite precursor solution was prepared by dissolving $PbCl_2$, PbI_2, CsI, and FAI in a molar ratio of 0.55:5.5:0.93:4.6 in a solvent mixture of DMF and NMP (5 mL:0.53 mL). The solution was deposited by spin coating at 5000 rpm for 30 s (50 μL) inside

the glovebox. The film was first annealed at 70 °C for 5 min in the glovebox, then immediately transferred to ambient conditions for annealing at 150 °C for 10 min.

Hole Transport Layer (HTL)

The HTL solution was prepared by dissolving 10 mg of P3HT in 1 mL of chlorobenzene. For composite HTLs, appropriate weights of Zn_2(ZnTCPP) MONs were added to the P3HT solution to obtain various weight ratios. The HTL was deposited by spin coating 30 μL of solution at 3000 rpm for 30 s inside the glovebox.

Electrode Deposition

An 80 nm gold electrode was thermally evaporated onto the HTL layer using an Edwards 306 bell-type evaporator. The completed devices were encapsulated for testing.

Reference

1. X. Y. Chin, D. Turkay, J. A. Steele, S. Tabean, S. Eswara, M. Mensi, P. Fiala, C. M. Wolff, A. Paracchino, K. Artuk and D. Jacobs, *Science*, 2023, 381, 59–63.
2. K. Chen, S. Schünemann, S. Song and H. Tüysüz, *Chem. Soc. Rev.*, 2018, 47, 7045–7077.
3. G. W. Kim, D. V. Shinde and T. Park, *RSC Adv.*, 2015, 5, 99356–99360.
4. P. Xu, E. L. Lim and Z. Wei, *ChemSusChem*, 2025, 18, e202500460.
5. F. Lin, J. Luo, Y. Zhang, J. Zhu, H. A. Malik, Z. Wan and C. Jia, J. Mater. Chem. A, 2023, 11, 2544–2567.
6. P. Zhou, T. Bu, S. Shi, L. Li, Y. Zhang, Z. Ku, Y. Peng, J. Zhong, Y. B. Cheng and F. Huang, J. Mater. Chem. C, 2018, 6, 5733–5737.
7. S. Kundu and T. L. Kelly, *Mater. Chem. Front.*, 2018, 2, 81–89.
8. D. J. Ashworth and J. A. Foster, *J. Mater. Chem. A*, 2018, 6, 16292–16307
9. J. Nicks, K. Sasitharan, R. R. Prasad, D. J. Ashworth and J. A. Foster, *Adv. Funct. Mater*., 2021, 31, 2103723.
10. F. Arjmand and Z. R. Rashidi Ranjbar, *Sci. Rep.*, 2024, 14, 12843.
11. K. Sasitharan, D. G. Bossanyi, N. Vaenas, A. J. Parnell, J. Clark, A. Iraqi, D. G. Lidzey and J. A. Foster, *J. Mater. Chem. A*, 2020, 8, 6067–6075.
12. K. Sasitharan, R. C. Kilbride, E. L. Spooner, J. Clark, A. Iraqi, D. G. Lidzey and J. A. Foster, *Adv. Sci*., 2022, 9, 2200366.
13. M. R. Ibrahim, S. Alneyadi, K. N. Truong, H. El-Maghraby, M. Abdellah, A. M. El-Zohry, S. Wuttke and Y. Greish, *RSC Adv.*, 2025, 15, 21479–21492
14. V. Zeleňák, Z. Vargová and K. Györyová, *Spectrochimica Acta Part A: Molecular and Biomolecular Spectroscopy*, 2007, **66**, 262–272.

15. L. Chen, Y. Yang and D. Jiang, *J. Am. Chem. Soc.*, 2010, 132, 9138–9143.

16. T. Bu, J. Li, H. Li, C. Tian, J. Su, G. Tong, L. K. Ono, C. Wang, Z. Lin, N. Chai and X. L. Zhang, *Science*, 2021, 372, 1327–1332

17. F. Cheng, R. He, S. Nie, C. Zhang, J. Yin, J. Li, N. Zheng and B. Wu, *J. Am. Chem. Soc.*, 2021, **143**, 5855–5866.

Supporting information

The photovoltaic performance of perovskite solar cells incorporating Zn_2(ZnTCPP) MONs and P3HT, with TCPP used as the sole organic linker, was systematically evaluated.

To evaluate the impact of Zn_2(ZnTCPP) metal-organic nanosheets (MONs) on the hole transport properties of perovskite solar cells (PSCs), devices were fabricated using P3HT blended with Zn_2(ZnTCPP) MONs as the hole transport layer (HTL). Two blend ratios were investigated: 1:10 and 1:1 in weight ratio (Zn_2(ZnTCPP):P3HT). The TCPP organic linker was also used as a support chemical for comparison.

Statistical Device Performance

Figures S3.1 and S3.2 show the statistical distribution of the main PV parameters for 1:10 and 1:1 device:

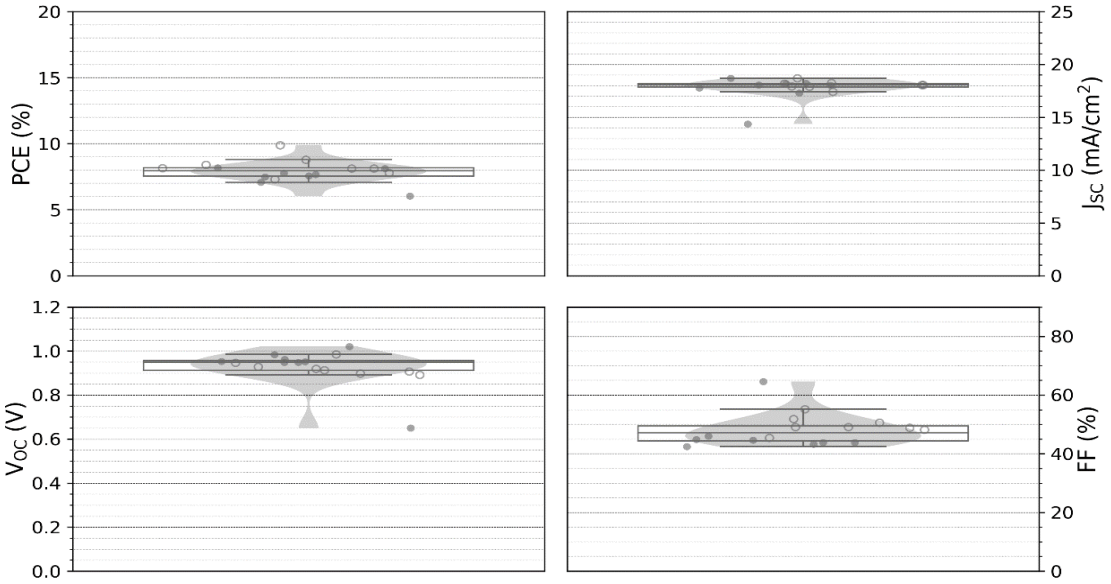

Figure S3.1 PV parameters of 1:10wt% Devices

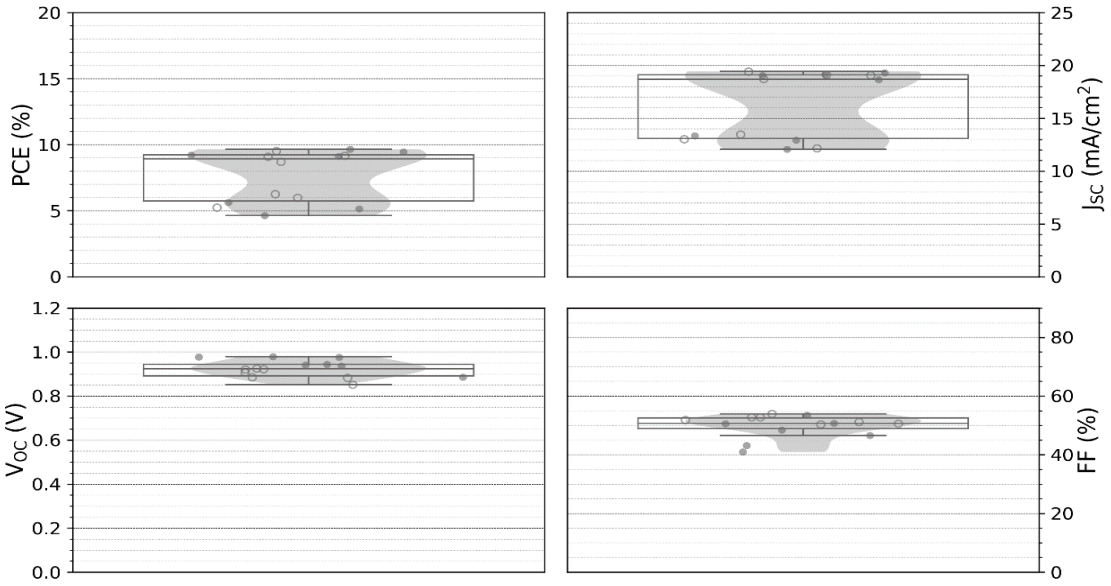

Figure S3.2 PV parameters of 1:1 wt% Devices

Representative current density–voltage (J–V) curves for the best-performing devices are provided in Figures S3.3 and S3.4:

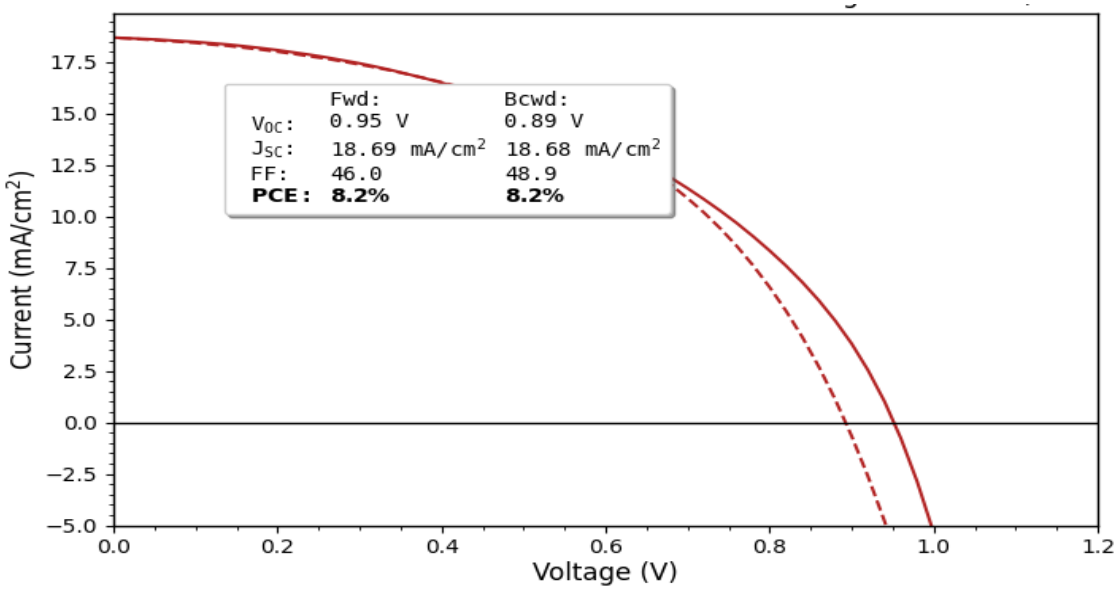

Figure S3.3 Champion Device of 1:10 wt% Devices

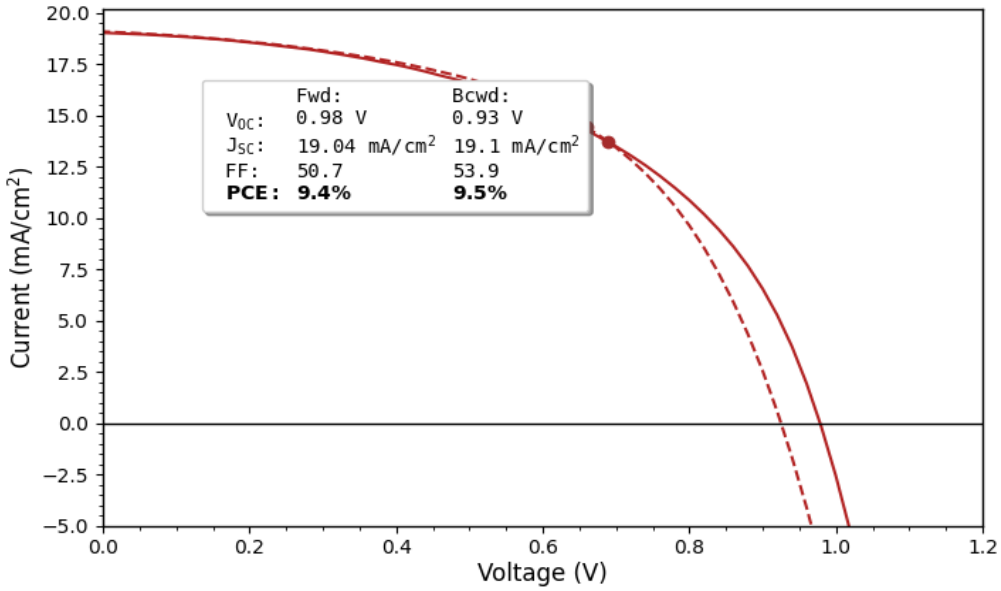

Figure S3.4 Champion Device of 1:1 wt% Devices

Figure S3.5 and 3.6 show the statistical distribution of the main PV parameters for 1:0.5wt% champion devices of P3HT-TCPP

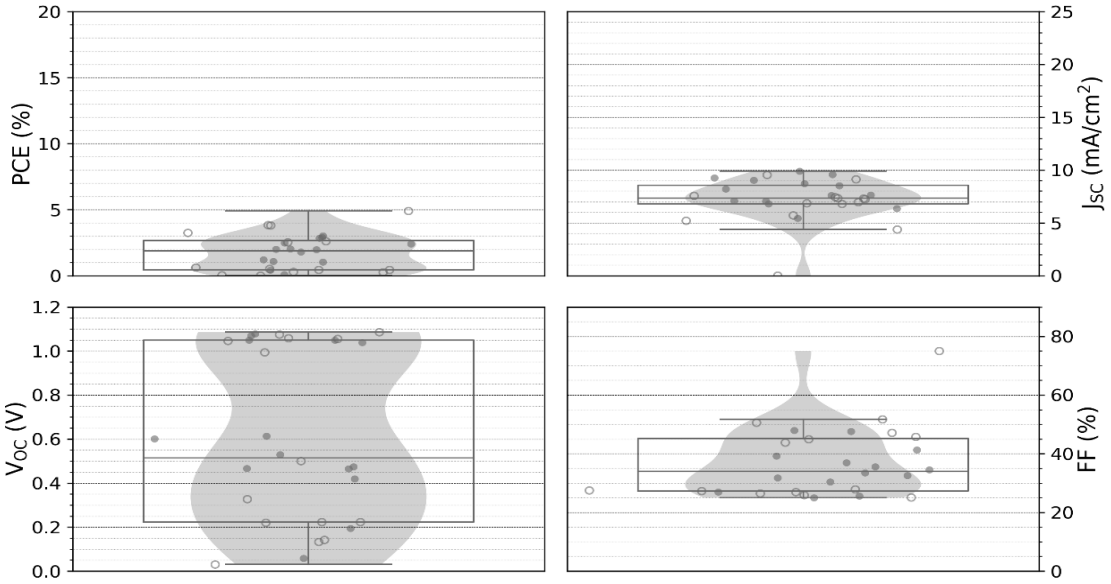

Figure S3.5 PV parameters of 1:0.5 wt% of P3HT-TCPP Devices

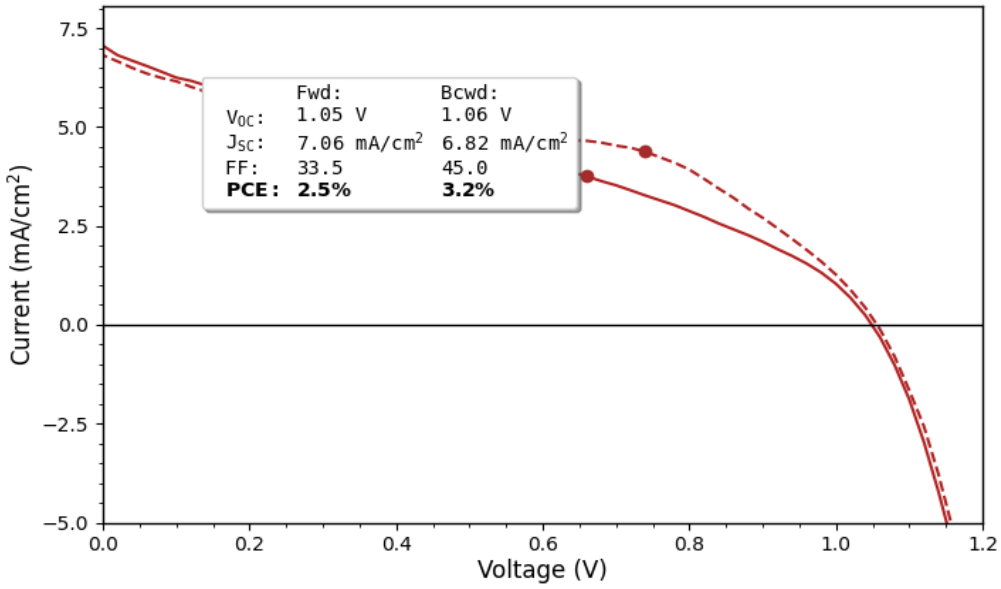

Figure S3.6 Champion Device of 1:0.5 wt%of P3HT-TCPP Devices

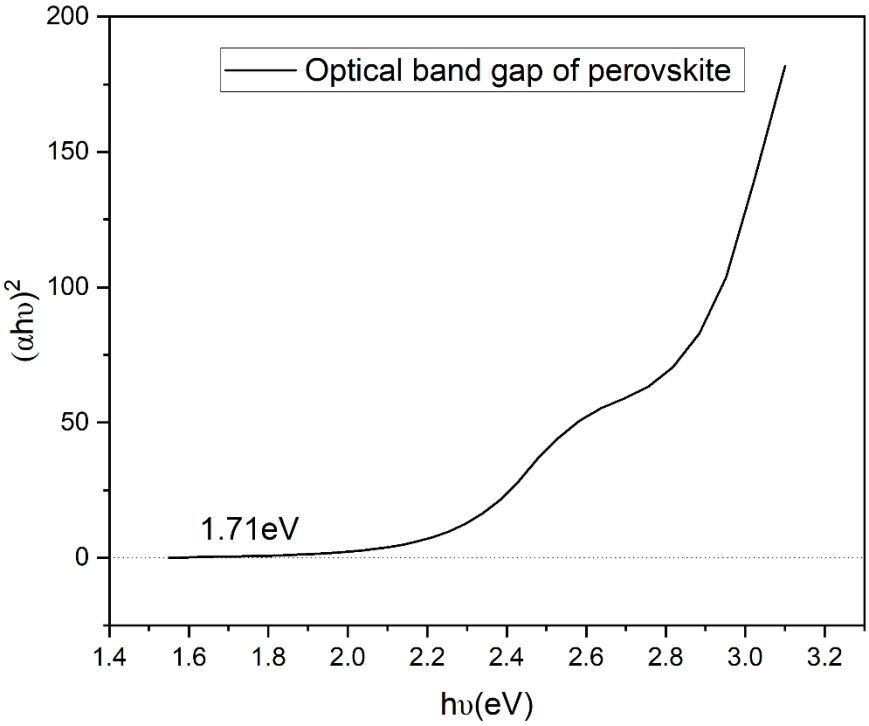

Figure S3.7 Optical band gap of $CSFAPbCl_{0.3}I_{0.7}$

Chapter 4: Comparative enhancement of hole transport in P3HT hole transport layers using Cu_2(CuTCPP) and Zn-Pd-TCPP 2D MONs

4.1 Introduction

Building upon the findings in Chapter 3, where the integration of Zn_2(ZnTCPP) metal–organic framework nanosheets (MONs) into P3HT-based hole transport layers (HTLs) significantly improved device performance, this chapter explores further structural and compositional modifications of porphyrin-based MONs to enhance hole transport in perovskite solar cells (PSCs). The previously demonstrated improvements in charge mobility, film morphology, and energy level alignment validate the use of porphyrin-based 2D MONs as promising functional additives.

As 2D materials constructed by the coordination of organic ligands with metal ions or clusters, MONs inherits the functional diversity of traditional MOFs while offering distinct advantages in thin-film devices owing to their ultrathin morphology and high specific surface area.[1] These features contribute to enhanced interfacial coupling, efficient carrier transport, and tunable energy level alignment in optoelectronic systems.[2]

Many studies have demonstrated that the functional properties of MONs are closely linked to the characteristics of their metal centres.[3] In particular, factors such as the electronic configuration, coordination environment, electrochemical activity, and polarization ability of different metal ions can substantially influence the band structure, charge-carrier mobility, crystallization behavior, and interfacial compatibility of MONs.[4] Considering these insights into metal-dependent modulation of MON properties, this chapter explores the use of two novel types of porphyrin-based MONs, Cu_2(CuTCPP) (copper-coordinated tetrakis(4-carboxyphenyl) porphyrin) and Zn–Pd–TCPP(Bimetallic Zn–Pd tetrakis(4-carboxyphenyl)porphyrin), to investigate the

tunability of hole transport properties in PSCs.

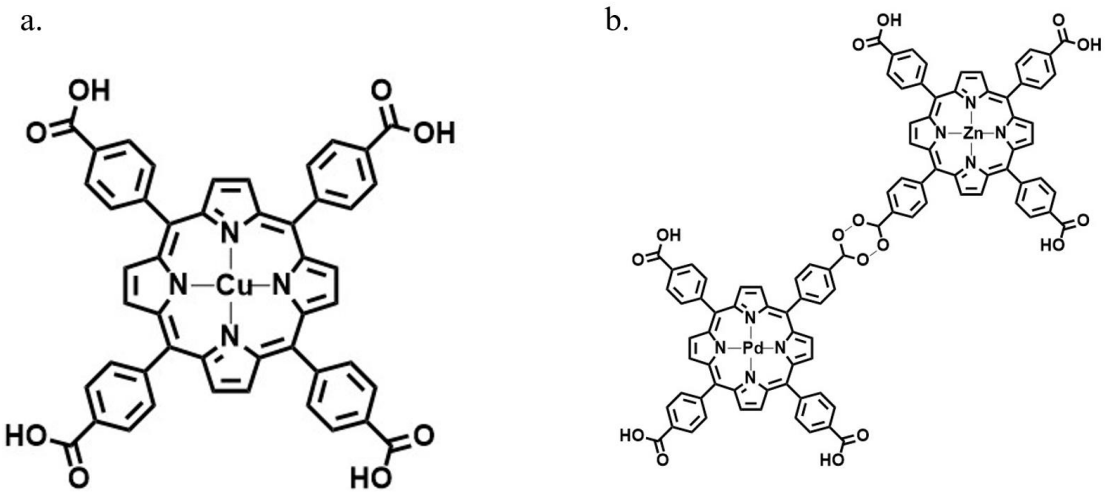

Figure 4.1 Structure of a. Cu_2(CuTCPP) and b. Zn-Pd-TCPP

Cu_2(CuTCPP) is a structurally ordered two-dimensional MON with a fully conjugated π-porphyritic backbone. This unique porphyrinic scaffold imparts strong optical absorption and a broad, intense visible-light response.[5] For instance, Andrés et al[6] employed Cu_2(CuTCPP) nanosheets in visible-light-driven overall water splitting, where they efficiently absorbed light with $\lambda > 450$ nm and generated a pronounced anodic photocurrent under illumination. The photocurrent varied with applied bias, indicating that charge carriers could effectively migrate to the electrode. Furthermore, in situ ATR-FTIR measurements showed that, upon visible-light irradiation, the vibrational peaks of the carboxyl C=O and –OH groups exhibited redshifts, suggesting that photoexcited electrons were transferred from the ligands to the copper nodes, thereby facilitating charge transport.[6] Taken together, these results highlight the strong optical response and efficient electron–hole separation capability of Cu_2(CuTCPP).

In another work, Liang et al [7] introduced 0.5% Cu_2(CuTCPP) MONs into g-C_3N_4 to build a 0.5% CuTCPP/g-C_3N_4 composite which produced 350 μmol·g^{-1} of hydrogen after 2 hours of simulated solar irradiation, which is about 8.3 times higher than that of pure g-C_3N_4. Besides, electrochemical impedance spectroscopy (EIS) and photoluminescence (PL) measurements further revealed that the incorporation of

Cu_2(CuTCPP) significantly reduced charge transfer resistance and quenched the PL signal. These results indicate that Cu_2(CuTCPP) effectively promotes the separation and transfer of photogenerated charge carriers. Based on these works, we therefore hypothesize that Cu_2(CuTCPP) is a highly promising additive for HTLs in PSCs.

Metal ion doping has emerged as an effective strategy to further improve the electrical conductivity of porphyrin-based MONs.[8] In particular, the incorporation of Pd^{2+} into MONs has been reported to enhance charge carrier concentration by introducing additional electronic states near the Fermi level, and to improve carrier mobility by facilitating continuous charge-hopping pathways across metal nodes. Such improvements have been demonstrated in a variety of systems, including Pd-doped Ni-MOFs for electrocatalysis[9], Pd-functionalized Zr-based MOFs for sensing applications[10], and Pd@MOF composites used in energy storage[11] and HER catalysis.[12] These findings suggest that Pd^{2+} can play a dual role in modulating both the electronic and structural characteristics of MONs, making it a versatile dopant for enhancing performance in charge-sensitive applications.

The Zn-based framework offers a structurally robust scaffold with a suitable band gap of 2.498 eV and well-aligned energy levels (VB = –5.689 eV, CB = –3.191 eV), conducive to photocatalytic water splitting[13]. However, the d^{10} closed-shell configuration of Zn^{2+} limits its capacity for hole extraction and transport, as charge transfer in Zn-TCPP predominantly relies on intra-ligand π–π* transitions with minimal ligand-to-metal charge transfer (LMCT) pathways. In contrast, Pd-TCPP demonstrates significantly enhanced charge separation and transport properties, as evidenced by its long-lived triplet state (62 μs) and efficient LMCT enabled by the open-shell d^8 configuration of Pd^{2+}.[14]

This facilitates hole capture at the Pd centre through N→Pd interactions, as supported by NBO analysis and transient photocurrent measurements. Moreover, electrochemical impedance spectroscopy (EIS) and photophysical studies indicate reduced interfacial resistance and suppressed charge recombination in Pd-based systems compared to their

Pt analogues. By combining Zn and Pd within a single MOF system, the design leverages the structural stability and high surface area of Zn nodes with the superior hole extraction and transport capabilities of Pd-TCPP linkers. The conduction band of the Zn framework aligns favourably with the LUMO of Pd-TCPP, while the Pd centre serves as a localized hole sink, enhancing separation and transport via LMCT pathways. This dual-site configuration not only stabilizes photogenerated holes but also preserves solvent tolerance, with Pd–N coordination shown to remain intact in polar environments.

Thus, in this chapter, Cu_2(CuTCPP) and Zn–Pd–TCPP MONs were synthesized and blended with P3HT to form hybrid HTLs. The impact of each MON on the photovoltaic performance and energy-level alignment of PSCs was systematically compared, including a direct comparison with the Zn_2(ZnTCPP)-based system discussed in the previous chapter. By evaluating three MON structures with distinct metal compositions, this chapter aims to provide deeper insights into the structure–property relationships governing MON–polymer hybrid HTLs and to offer practical strategies for enhancing PSC performance through rational material design.

4.2 Results

4.2.1Synthesis and characterization of the Cu_2(CuTCPP) and Zn-Pd-TCPP MONs

Cu_2(CuTCPP) and Zn–Pd–TCPP nanosheets were synthesized according to previously established methods by Sasitharan et al[15]and Kim et al [14]. Briefly, Cu_2(CuTCPP) was synthesized by heating a mixture of meso-tetra(4-carboxyphenyl) porphyrin (H_2TCPP) and copper (II) nitrate trihydrate ($Cu(NO_3)_2 \cdot 3H_2O$) in a solvent system consisting of N, N-dimethylformamide (DMF) and ethanol (EtOH) at 80 °C for 24 hours. The reaction yielded a 3D MOF as a black microcrystalline powder. The product was collected as a purple solid, washed thoroughly with ethanol, and isolated by centrifugation. The purified material was subsequently redispersed in ethanol and sonication for one hour

to form 2D MONs.

Zn-Pd-TCPP was prepared by a two-solution approach. In vial A, zinc nitrate trihydrate ($Zn(NO_3)_2 \cdot 3H_2O$), polyvinylpyrrolidone (PVP), and trifluoroacetic acid (TFA) were dissolved in a mixed solvent of DMF and ethanol. Separately, in vial B, palladium (II) meso-tetra(4-carboxyphenyl) porphyrin (Pd-TCPP) was dissolved in a mixture of DMF and ethanol. The solution in vial B was added into vial A under stirring. The resulting mixture was sonicated for 10 minutes and then heated at 80 °C for 24 hours.

The formation of the target crystalline phase was confirmed by XRD, verifying the structural integrity of the synthesized 2D MONs. Elemental analysis gave results consistent with the expected molecular compositions of approximately $C_{48}H_{26}Cu_3N_4O_{8.8}H_2O$ and $C_{48}H_{26}N_4O_8PdZn_2$ $._3H_2O$, hereafter referred to as Cu_2(CuTCPP) and Zn–Pd–TCPP MONs, respectively. UV–Visible (UV-Vis) absorption spectroscopy was used to characterize the electronic transitions of the framework, while Fourier-transform infrared (FT-IR) spectroscopy provided complementary information on functional groups and coordination modes. Taken together, these results confirm the successful and reproducible synthesis of the desired 2D MONs.

To evaluate the nanosheet morphology and thickness, atomic force microscopy (AFM) was conducted on Cu_2(CuTCPP) and Zn–Pd–TCPP samples, Typically, measurements of 10 μL suspensions deposited on mica revealed the formation of ultrathin nanosheets.As shown in Figure 4.2. The Cu_2(CuTCPP) nanosheets appeared well-dispersed across the substrate, with relatively smooth surface profiles and distinct thicknesses in the range of 2.0–4.3 nm, which is consistent with monolayer or bilayer 2D MONs structures.

In contrast, the Zn–Pd–TCPP sample exhibited a more densely packed morphology, accompanied by pronounced height increases in the AFM profile. The measured thickness of these nanosheets ranged from 4.5 to 7.5 nm, indicating possible multilayer stacking or increased interlayer interactions caused by Pd^{2+} incorporation. The observed

morphological changes suggest that Pd doping not only modifies the charge transport properties of the material but also affects its assembly behaviour and film-forming characteristics.

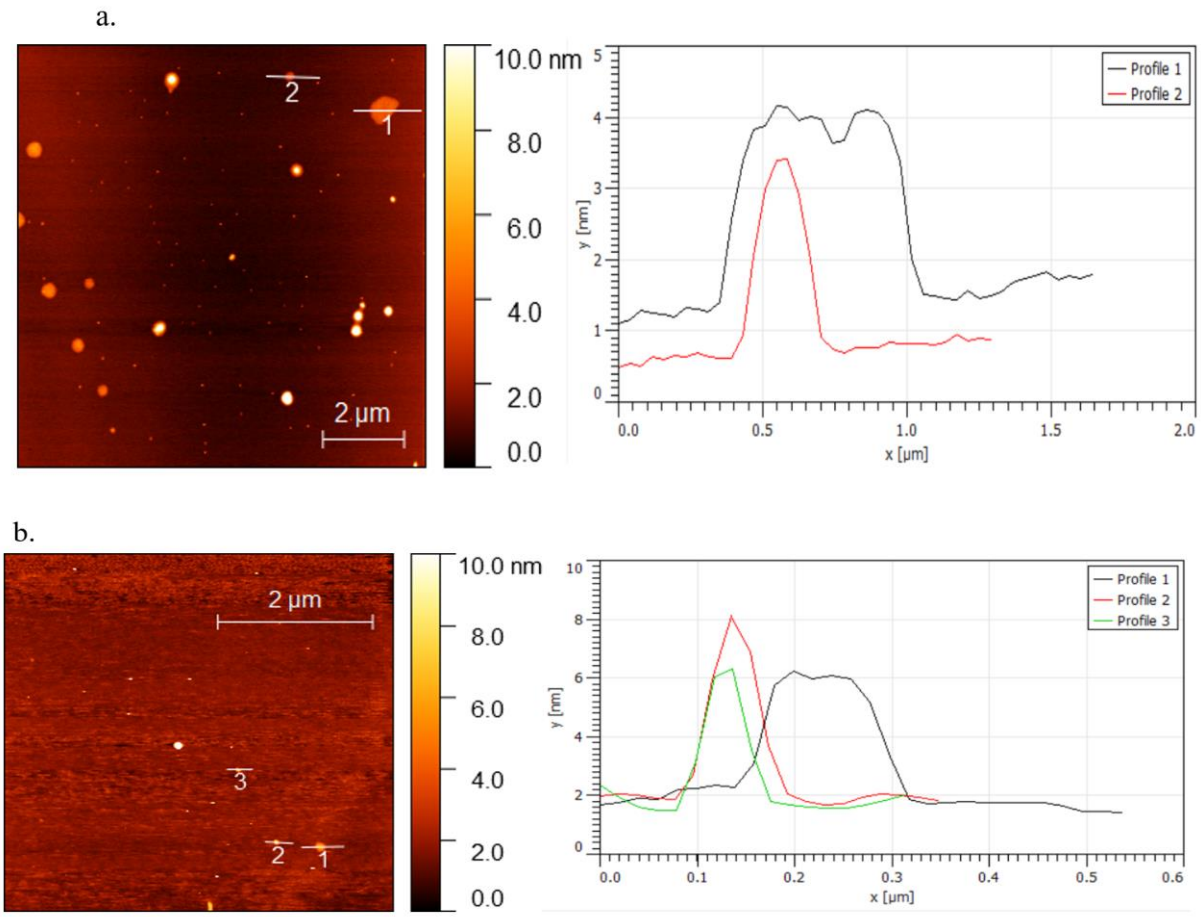

Figure 4.2 AFM images and selection of a. Cu_2(CuTCPP) and b. Zn-Pd-TCPP nanosheet

These observations confirm that Cu_2(CuTCPP) nanosheets exhibit thinner and more uniform morphology compared to Zn–Pd–TCPP, which is critical for their integration into thin-film optoelectronic applications. This proves the consistency of the structure of 2D MONs.

To determine the percentage composition of carbon, hydrogen, and nitrogen in the product was derived from elemental analysis experiments. $C_{48}H_{24}Cu_3N_4O_8.8H_2O.DMF$ and $C_{48}H_{26}N_4O_8PdZn_2.3H_2O$ calculated from the molecular formula was used as the theoretical value for the structure of Cu2(CuTCPP) and Zn-Pd-TCPP MONs. Element

analysis was carried out on the synthesized samples to compare their compositions. The experimental CHN results of both Cu_2(CuTCPP) and Zn–Pd–TCPP MONs show lower carbon and slightly higher hydrogen contents compared with their theoretical compositions, indicating the presence of coordinated or adsorbed water molecules. The deviation is more pronounced for Cu_2(CuTCPP), corresponding to approximately eight water molecules and DMF per formula unit, while the Zn–Pd–TCPP sample exhibits a lower degree of hydration (~3H_2O). These results confirm that both MONs retain the porphyrin framework integrity but contain variable amounts of bound water due to their structural and compositional differences.

Table 1. Elemental analysis of Cu2(CuTCPP) and Zn-Pd-TCPP MONs

Sample	C	H	N
$C_{48}H_{24}Cu_3N_4O_8$.8H_2O.DMF	51.37%	3.97%	5.87%
Synthesized Cu_2(CuTCPP) MONs	51.79%	4.08%	5.81%
$C_{48}H_{26}N_4O_8PdZn_2$.3H_2O	53.38	2.81%	5.21%
Synthesized Zn-Pd-TCPP MONs	53.48%	2.99%	5.20%

The XRD patterns of Zn_2(ZnTCPP), Cu_2(CuTCPP), and Zn–Pd–TCPP MONs (Figure 4.3a) reveal distinct structural characteristics that reflect the influence of metal centers on framework ordering. Both Zn_2(ZnTCPP) and Cu_2(CuTCPP) MONs exhibit multiple sharp and well-resolved diffraction peaks in the 2θ range of 5–30°, indicative of a high degree of crystallinity and long-range periodicity within the 2D layered frameworks. For Zn_2(ZnTCPP), the most intense reflection appears at 8.07°, corresponding to the (001) plane with an interlayer d-spacing of approximately 10.9 Å, accompanied by

additional prominent peaks at 10.09° (100), 11.73° (110), 13.31° (200), 17.35° (210), 24.80° (300), and 27.26° (005). Similarly, Cu_2(CuTCPP) exhibits its strongest diffraction at 7.87° (001) with a d-spacing of 11.2 Å, along with well-defined peaks at 8.16° (002), 9.53° (003), 11.45° (100), 13.27° (110), 14.09° (200), 20.40° (004), and 24.16° (300). The presence of these pronounced reflections confirms that the metal–porphyrin coordination units are regularly arranged, forming extended crystalline domains. The slight differences in peak positions between Zn_2(ZnTCPP) and Cu_2(CuTCPP), particularly the shift of the (001) reflection from 7.87° to 8.07°, can be attributed to variations in lattice parameters arising from the distinct ionic radii and coordination geometries of Cu^{2+} and Zn^{2+}, respectively, resulting in a contraction of the interlayer spacing from 11.2 Å to 10.9 Å.

In contrast, the Zn–Pd–TCPP MONs exhibit only a single broad diffraction feature centered at approximately 4.6°, with no discernible high-angle reflections. The strongest and essentially only observable peak appears at 7.42°, corresponding to the (001) plane with a d-spacing of 11.9 Å, which is broader and significantly less intense than the corresponding reflections in the Cu and Zn analogs. A few weak features at 8.17°, 9.48°, 11.18°, and 13.42° are also detectable but are substantially broader and lower in intensity, indicating a markedly reduced coherence length. This broad, low-intensity pattern suggests a significantly lower degree of crystallinity and a more disordered stacking arrangement. The disruption of long-range order is likely attributable to the incorporation of Pd^{2+} into the Zn–TCPP framework, where heterobimetallic coordination may introduce local lattice distortions and weaken interlayer interactions, resulting in interlayer displacements that lead to turbostratic stacking.[15]

Collectively, these observations indicate that while Cu_2(CuTCPP) and Zn_2(ZnTCPP) MONs retain a well-defined layered crystalline architecture with clear (001), (100), and (110) reflections, the introduction of Pd^{2+} into the Zn–TCPP framework results in a partial loss of periodicity and reduced structural order, as evidenced by the

disappearance of high-angle peaks and significant broadening of the (001) reflection. The interlayer spacing follows a clear trend: Zn–Pd–TCPP (11.9 Å) > Cu_2(CuTCPP) (11.2 Å) > Zn_2(ZnTCPP) (10.9 Å), suggesting that metal substitution effectively modulates the interlayer packing density. This structural variation supports the hypothesis that Pd incorporation modulates the self-assembly and packing behavior of porphyrin-based MONs. Our findings are consistent with previous reports on 2D porphyrinic MONs, confirming the successful synthesis of crystalline Cu_2(CuTCPP) and Zn_2(ZnTCPP), as well as structurally disordered Zn–Pd–TCPP nanosheets.[16,17]

The FT-IR spectra (Figure 4.3b) provide direct evidence for the successful coordination of Cu^{2+} ions with the TCPP ligands in Cu_2(CuTCPP) MONs. In the fingerprint region (1800–400 cm^{-1}), several diagnostic changes are observed upon metal coordination. The strong absorption band at 1700 cm^{-1}, assigned to the C=O stretching vibration of free carboxylic acid groups in TCPP, is significantly attenuated in the Cu_2(CuTCPP) MONs, while a new, intensified band appears at approximately 1400 cm^{-1}, corresponding to the symmetric stretching vibration of deprotonated carboxylate (COO^-) groups. Concurrently, a new peak emerges at around 500 cm^{-1}, which can be attributed to the Cu–N stretching vibration, confirming coordination between Cu^{2+} and the porphyrin core nitrogen atoms. The characteristic porphyrin ring breathing vibration near 1000 cm^{-1} remains well preserved, indicating that the porphyrin core structure is retained during assembly. These spectral changes are fully consistent with the expected coordination geometry and confirm the successful formation of Cu_2(CuTCPP) MONs.

Similarly, the FT-IR spectrum of Zn–Pd–TCPP MONs reveals notable changes compared to the free TCPP ligand, confirming successful coordination and framework formation. The C=O stretching band at 1700 cm^{-1} is markedly reduced in intensity, accompanied by a pronounced enhancement of the COO^- symmetric stretching band at approximately 1400 cm^{-1}, which indicates deprotonation of the carboxylic acid groups upon metal coordination. A new absorption feature near 500 cm^{-1}, assignable to metal–nitrogen (M–N) stretching, further confirms the coordination of metal ions to the

porphyrin N atoms. The porphyrin ring breathing mode at approximately 1000 cm^{-1} remains intact, confirming that the porphyrin core is preserved during the synthesis of Zn–Pd–TCPP MONs. These spectral features collectively demonstrate the formation of a metal–ligand network via both carboxylate and porphyrin nitrogen coordination sites.

The UV–Vis absorption spectra of Cu_2(CuTCPP) and Zn–Pd–TCPP MONs are presented in Figures 4.3c and 4.3d, respectively. The Cu_2(CuTCPP) MONs display a broad absorption band centered around 438 nm, which can be assigned to a Soret-like transition, together with a weaker feature near 555 nm corresponding to a Q-type band. Although these bands appear less distinct than those in isolated porphyrin molecules, the broadened and attenuated profiles are consistent with the formation of extended 2D coordination frameworks, in which strong π–π stacking and metal–ligand interactions cause spectral broadening and partial overlap of electronic transitions.[18] The reduced spectral resolution further suggests enhanced delocalization within the Cu–porphyrin layers, in agreement with the high crystallinity observed in the XRD results.

By contrast, the Zn–Pd–TCPP MONs exhibit two discernible absorption features at approximately 435 nm and 532 nm, characteristic of Soret- and Q-type transitions, respectively. The clearer separation of these two bands indicates a lower molecular symmetry, likely arising from the heterobimetallic coordination of Zn^{2+} (d^{10}) and Pd^{2+} (d^{8}) centers. The introduction of Pd^{2+} induces additional d–π orbital coupling and ligand-to-metal charge transfer (LMCT) processes, leading to red-shifted and broadened absorption features.[19] These effects reflect enhanced electronic coupling and charge delocalization within the Zn–Pd–TCPP network, which may facilitate hole extraction when incorporated into polymeric HTLs.

Overall, the optical characteristics of both MONs confirm the retention of porphyrinic electronic transitions, though their spectral shapes differ due to variations in metal-center symmetry and interlayer coupling. The broadened and merged absorption bands thus represent collective excitations within the extended frameworks rather than discrete molecular transitions.

a.

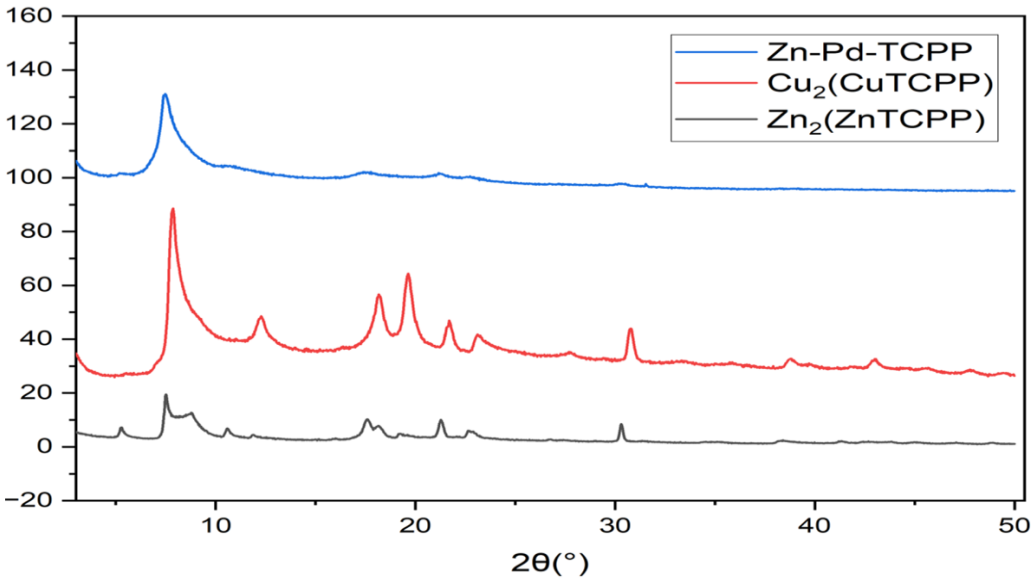
Zn-Pd-TCPP
Cu2(CuTCPP)
Zn2(ZnTCPP)
2θ(°)

b.

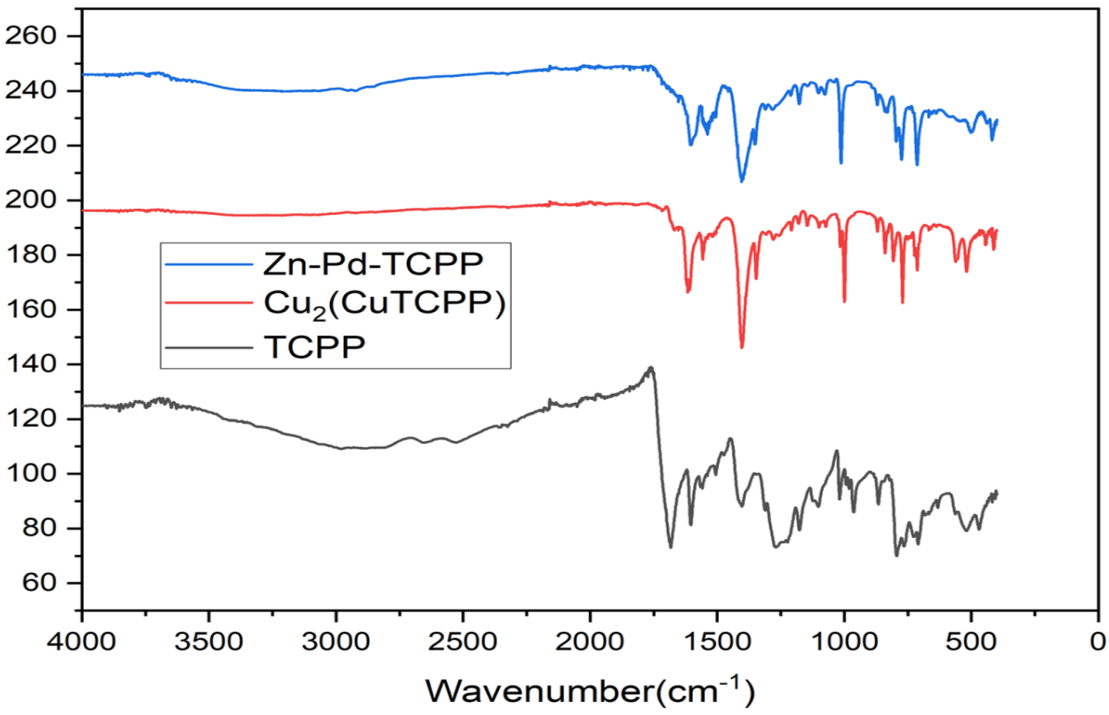
Zn-Pd-TCPP
Cu2(CuTCPP)
TCPP
Wavenumber(cm-1)

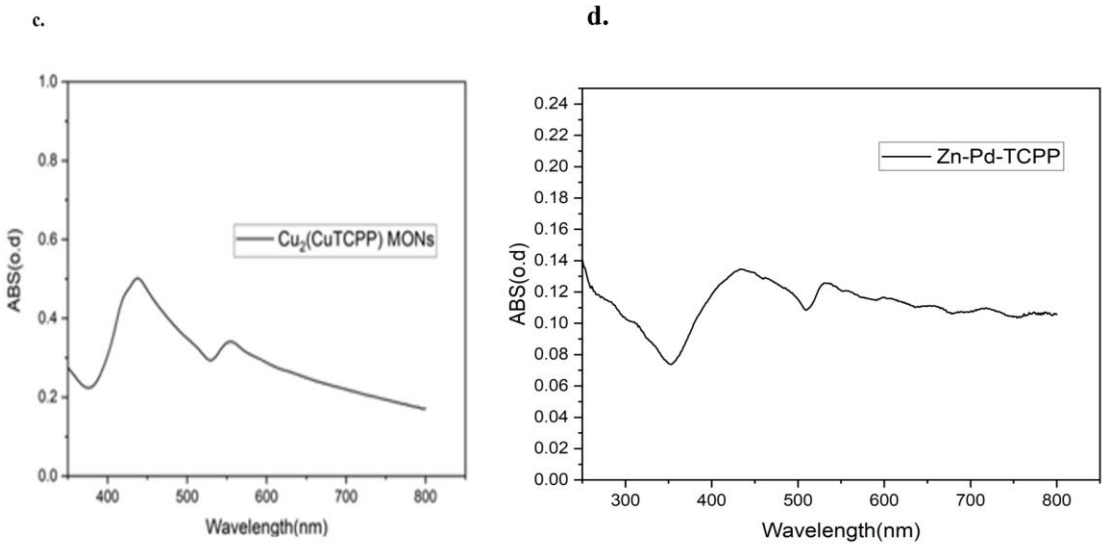

Figure 4.3. Physical characterization of a. XRD for Zn_2(ZnTCPP), Cu_2(CuTCPP) and Zn-Pd-TCPP, b. FT-IR spectra recorded for Cu_2(CuTCPP), Zn-Pd-TCPP and TCPP ligand power., c,d. UV-Vis for Cu_2(ZnTCPP) and Zn-Pd-TCPP MONs redisperse in ethanol.

4.2.2 Device fabrication, optimization, and performance

Based on these findings and previous research, we have decided to integrate 2D MONs into HTL to optimize the efficiency of PSCs. This approach leverages the beneficial interaction between MONs and P3HT, aiming to achieve a significant improvement in device performance while maintaining the structural integrity and functional properties of HTL.

In Chapter 3 it was found that 50% weight ratio of P3HT: MONs is the best ratio. Thus, 50% of weight ratios of Cu_2(CuTCPP) and Zn-Pd-TCPP MONs were incorporated into the HTL to fabricate various PSCs. The same structure of PSCs in this study were fabricated with a conventional n–i–p structure of ITO/SnO_2/CSFAPbICl/P3HT (or P3HT–MONs)/Au, as illustrated in Chapter 3. The solar cell performance parameters, obtained using a Sun Simulator, are summarized in Table 2.

As detailed in Table 2, the baseline device employing P3HT as the HTL exhibited limited power conversion efficiency (PCE) of 6.55±0.16%, which aligns with the

known limitations of P3HT in terms of hole mobility and energy level alignment. Upon incorporation of Cu_2(CuTCPP) MONs into the P3HT matrix, the device performance improved markedly, with increases in open-circuit voltage (V_{oc}) and fill factor (FF), resulting in a PCE of 7.06±0.129%. This enhancement suggests that the nanosheets contributed to improved charge extraction and suppressed recombination losses at the HTL/perovskite interface.

Further improvement was achieved with Zn–Pd–TCPP MONs, where the device demonstrated the highest PCE of 7.99±0.143%, along with enhanced, Voc, and FF. The performance gain is likely attributed to better energy level matching and more favorable interfacial interactions between Zn–Pd–TCPP MONs and the P3HT matrix, which facilitated more efficient hole transport and collection. These results indicate that appropriate integration of conductive 2D MONs into HTL can significantly enhance the overall performance by optimizing interfacial energetics and transport dynamics. The comparative results validate the functional contribution of the MONs and highlight the importance of interfacial engineering in P3HT-based architecture.

It is noteworthy that both MON-incorporated devices exhibited a slight decrease in Jsc compared with the pristine P3HT-based cell. This reduction can be ascribed to the partial optical absorption and scattering introduced by the porphyrin-based MONs, which slightly reduce the photon flux reaching the perovskite layer. The incorporation of Cu_2(CuTCPP) and Zn–Pd–TCPP nanosheets also modifies the HTL morphology, leading to denser or slightly thicker films that further influence light transmission. Nevertheless, the enhanced Voc and FF indicate that interfacial charge extraction and energy level alignment were substantially improved, compensating for the minor photocurrent loss. Overall, the small reduction in Jsc reflects an optical trade-off, whereas the electrical benefits of improved carrier transport and reduced recombination dominate, resulting in a net efficiency gain.

The J–V characteristics of the PSCs employing different HTLs are shown in Figure c, and the corresponding photovoltaic parameters are summarized in Table 2. The control

device based on pristine P3HT exhibited a PCE of 8.27%, with Voc = 0.92 V, Jsc = 18.32 mA cm^{-2}, and FF = 58.61%. Upon incorporating Cu_2(CuTCPP) MONs into the P3HT matrix, the device achieved a slightly higher efficiency of 8.92% (Voc = 0.93 V, Jsc = 19.07 mA cm^{-2}, FF = 52.56%). A further enhancement was obtained for the Zn–Pd–TCPP-based device, which reached a PCE of 9.98% with an increased Voc (0.96 V) and comparable Jsc (18.37 mA cm^{-2}).

These results indicate that the integration of 2D porphyrin-based MONs into the P3HT HTL effectively improves interfacial charge extraction and suppresses recombination losses, as reflected by the increased Voc and PCE values. Although the Jsc remains nearly constant or slightly decreased, this can be attributed to light absorption and scattering within the modified HTL. The near-ideal diode behavior and minimal hysteresis observed in the J–V curves further confirm the improved interfacial energetics and charge transport stability enabled by the MON incorporation.

Together with the data in Table 2, these J–V measurements reinforce the conclusion that appropriate MON incorporation into the P3HT matrix plays a decisive role in optimizing interfacial energetics, improving carrier dynamics, and ultimately boosting solar cell efficiency.

Table 2. Comparative device performance using P3HT-based HTLs with and without Cu_2(CuTCPP) and Zn-Pd-TCPP MONs

No.	HTL	J_{sc}(mA/cm^2)	V_{oc}(V)	FF (%)	PCE (%)
1	P3HT	17.83±0.386	0.85±0.159	40.12±1.57	6.55±0.16
2	P3HT-Cu_2(CuTCPP) MONs	16.89±0.176	0.90±0.018	47.95±0.48	7.06±0.129
3	P3HT-Zn-Pd-TCPP MONs	17.17±0.186	0.92±0.019	53.2±0.42	7.99±0.143

a.

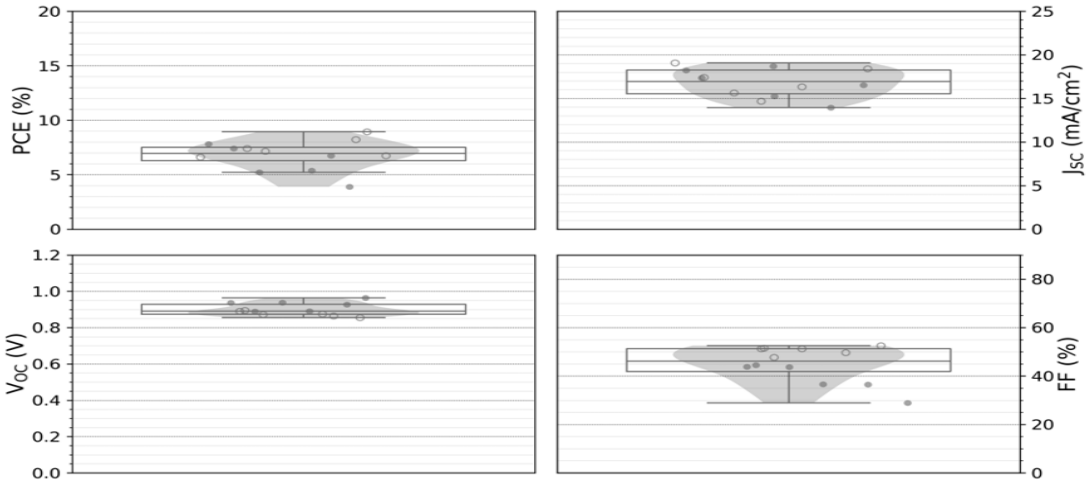

b.

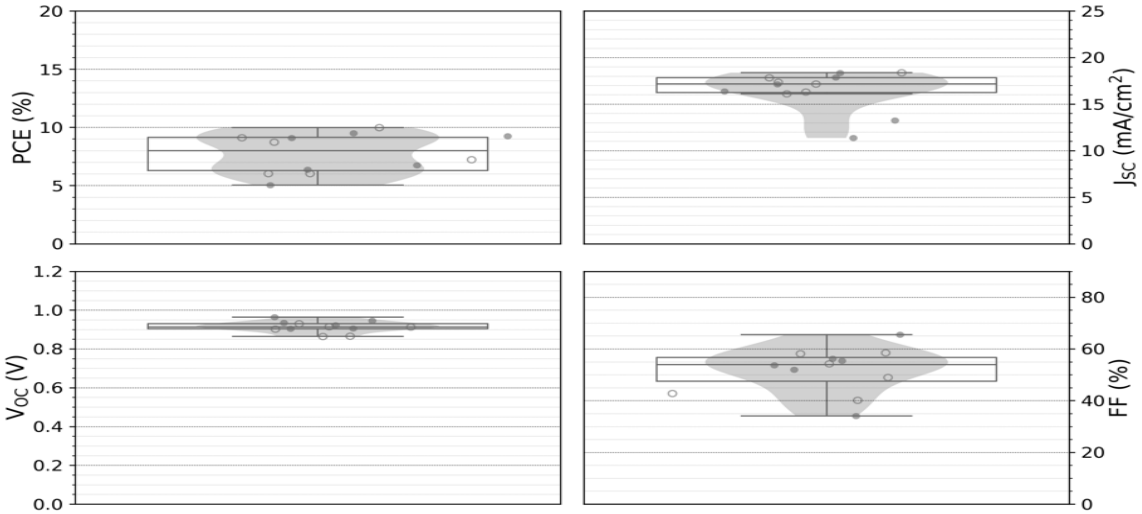

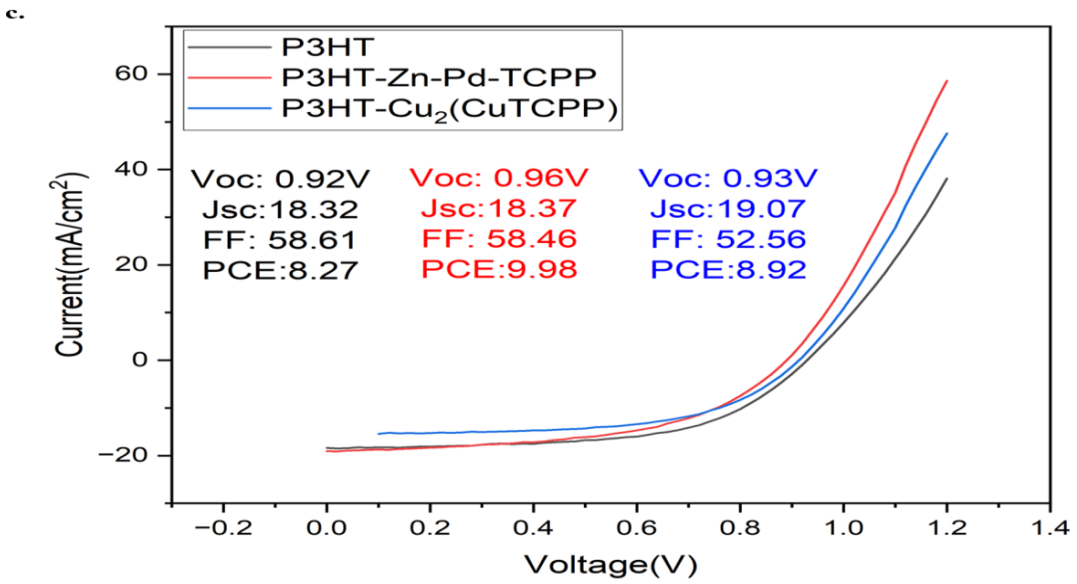

Figure 4.4 Performance of a. P3HT-Cu_2(CuTCPP) MONs devices and b. P3HT-Zn-Pd-TCPP devices, c. the champion devices of P3HT-Cu_2(CuTCPP) MONs devices and P3HT-Zn-Pd-TCPP devices.

The external quantum efficiency (EQE) spectra presented in Figure 4.5 offers further insight into the influence of 2D metal-organic nanosheets (MONs) on the photo response characteristics of the devices. The pristine P3HT-based device exhibited a typical spectral response with a broad plateau ranging from 400 to 750 nm and a maximum EQE exceeding 80% in the visible region.

Upon incorporation of Zn–Pd–TCPP MONs into the P3HT matrix, the device demonstrated a notable enhancement in EQE values across the entire visible range, particularly between 450 and 650 nm. The peak EQE response not only increased in magnitude but also broadened slightly, suggesting more efficient light-to-charge conversion. This improvement can be attributed to enhanced hole transport dynamics and better interfacial charge extraction, likely facilitated by the favorable energy alignment and nanoscale morphology of the Zn–Pd–TCPP MONs.

In contrast, the device incorporating Cu_2(CuTCPP) MONs displayed a modest reduction in EQE compared to the pristine P3HT device, with lower response across most of the spectrum. This may be related to suboptimal interfacial contact or reduced conductivity of the Cu-based MONs, leading to hindered charge extraction and

increased recombination losses.

Despite these differences, all three devices retained similar spectral profiles, indicating that the addition of MONs does not alter the fundamental absorption properties of the perovskite active layer. Overall, the EQE trends are consistent with the observed Jsc and PCE values extracted from J–V measurements, further validating the positive contribution of Zn–Pd–TCPP MONs to device performance enhancement.

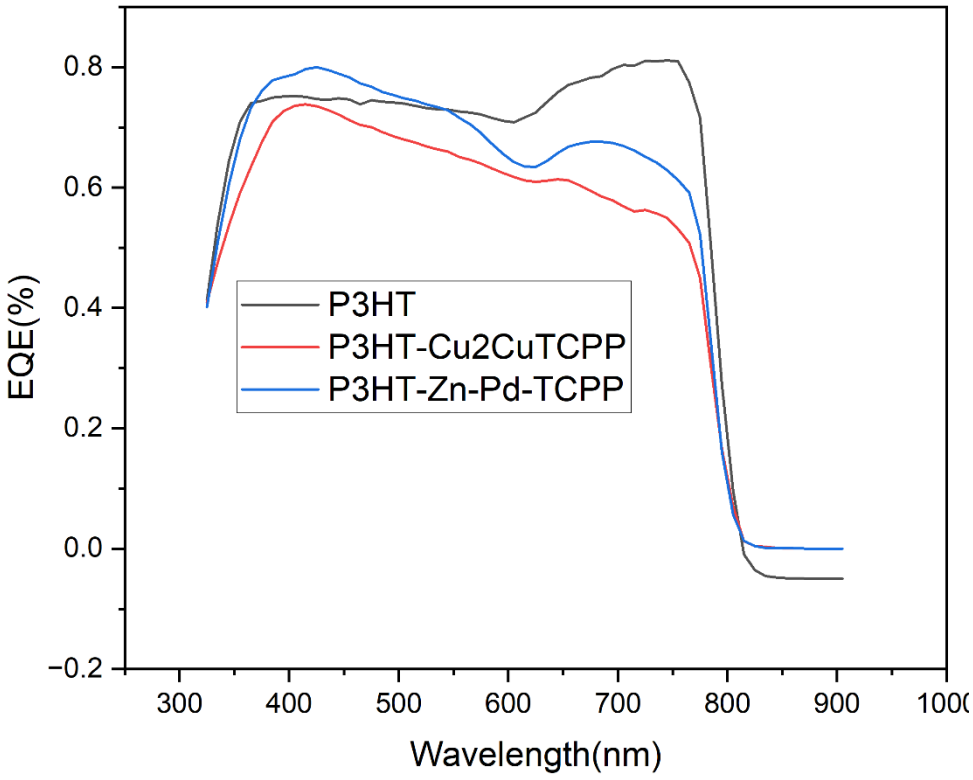

Figure 4.5 EQE spectra of PSCs using P3HT and P3HT-Cu2CuTCPP and Zn-Pd-TCPP MONs (1:0.5) as HTLs

4.2.3 Discussion on the role of MONs addition into the P3HT Hole transport layer

As shown in Figure 5a and 5b, AFM analysis was performed to evaluate the nanoscale surface morphology of the P3HT films blended with Cu_2(CuTCPP) and Zn–Pd–TCPP MONs, respectively. The pristine P3HT film in Chapter 3 is known to exhibit relatively uniform nanocrystalline domains with moderate surface roughness. Upon addition of

Cu_2(CuTCPP) MONs, the film (Figure 4.6a) retained the granular nanostructure but exhibited increased vertical height variation, reaching up to ~65 nm. The distribution of brighter features suggests local aggregation or poor dispersion of the nanosheets, leading to rougher surface topography.

In contrast, the P3HT-Zn–Pd–TCPP blend film (Figure 4.6b) displayed a more heterogeneous surface, with scattered bright domains rising as high as ~200 nm. These sharp protrusions are likely due to partial aggregation or vertical stacking of MONs, indicating less dispersion within the polymer matrix. Despite these features, the base film appears more continuous and compact than the Cu-based sample, which may suggest improved local film integrity and charge transport pathways.

Overall, while both MON-blended films introduced topographic features distinct from pristine P3HT, the Cu-based layer appears slightly more homogeneous at the nanoscopic scale, whereas the Zn–Pd-based film introduces larger height irregularities. These morphological differences may influence interfacial contact quality and hole extraction efficiency, potentially contributing to the distinct photovoltaic behavior observed in the corresponding devices.

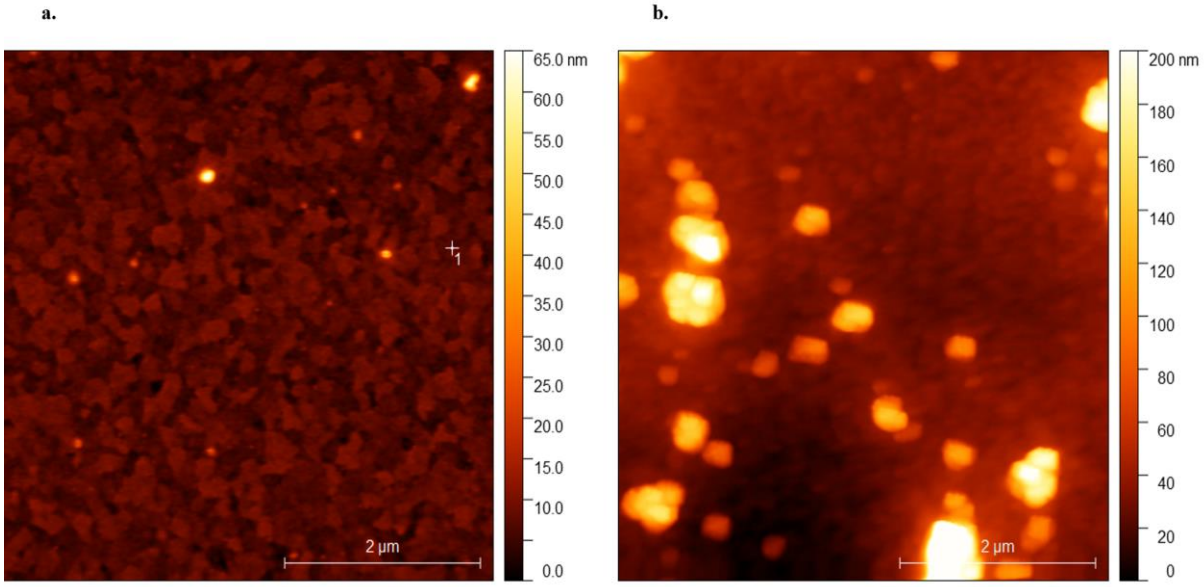

Figure 4.6 AFM image of a. P3HT-Cu_2(CuTCPP) layer and b. P3HT-Zn-Pd-TCPP layer.

Figure 4.7 presents the Raman spectra of pristine P3HT and P3HT–MON composite films (P3HT–Cu_2(CuTCPP) and P3HT–Zn–Pd–TCPP) on ITO glass substrates, recorded with a 532 nm excitation laser. All films exhibit two characteristic peaks at approximately 1380 and 1446 cm^{-1}, assigned to the C–C inter-ring stretching and C=C symmetric stretching modes of the thiophene backbone in P3HT, respectively. Upon MON incorporation, no discernible shifts in these peak positions are observed, confirming that the presence of Cu_2(CuTCPP) and Zn–Pd–TCPP MONs does not disrupt the conjugation length or molecular conformation of P3HT. This structural integrity is essential for maintaining the hole-transport functionality of the P3HT layer. Notably, slight variations in the absolute intensities of these characteristic peaks are observed among the films; however, as no internal standard was employed for intensity normalization, these differences should be interpreted with caution and are discussed only qualitatively. Nevertheless, the unchanged peak positions and lineshapes provide unambiguous evidence that the MONs do not degrade the polymer backbone, ensuring that any improvement in device performance can be attributed to the positive contributions of the MONs rather than to structural alteration of the P3HT matrix.

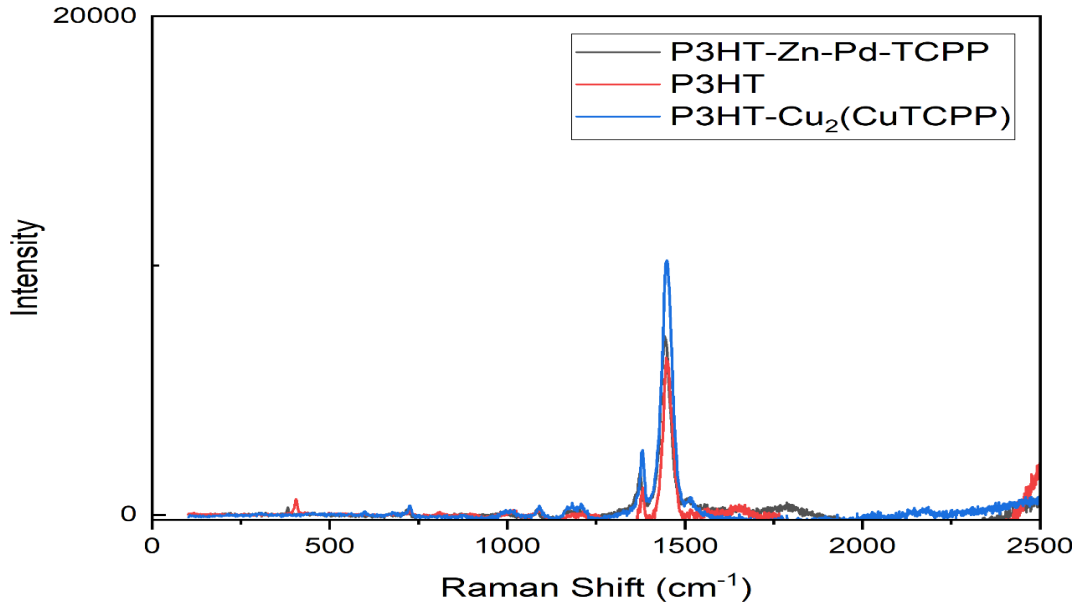

Figure 4.7. Raman Spectra of P3HT only and P3HT-Cu2(CuTCPP) and P3HT-Zn-Pd-TCPP MONs (5mg ml^{-1}) in ITO glasses

To further evaluate the interfacial charge transfer behavior, solid-state photoluminescence (PL) spectra of pristine P3HT and composite films incorporating Cu_2(CuTCPP) and Zn–Pd–TCPP MONs were recorded under the same conditions for device fabrication, as shown in Figure 4.8 The pristine P3HT film displays a strong and broad emission peak centered at approximately 670 nm, which corresponds to radiative recombination of photo-generated excitons within the polymer matrix.

Upon incorporation of MONs, the PL intensity was significantly quenched across the entire spectral range for both composite films. Notably, the P3HT-Cu_2(CuTCPP) film exhibited a more pronounced quenching effect compared to its Cu-based counterpart. This observation indicates more efficient charge separation and hole extraction in the Zn–Pd–TCPP system, likely due to better energetic alignment and interfacial contact with the P3HT matrix. In contrast, the partial quenching observed in the P3HT-Zn-Pd-TCPP film suggests relatively weaker interfacial interaction and less effective charge transfer.

Overall, the observed PL quenching behavior supports the hypothesis that MON incorporation facilitates photoinduced charge transfer and suppresses exciton recombination within the HTL. These results are consistent with the improved device performance observed in the J–V and EQE measurements, reinforcing the role of Zn–Pd–TCPP and Cu_2(CuTCPP). effective hole-extracting and transport-enhancing additives.

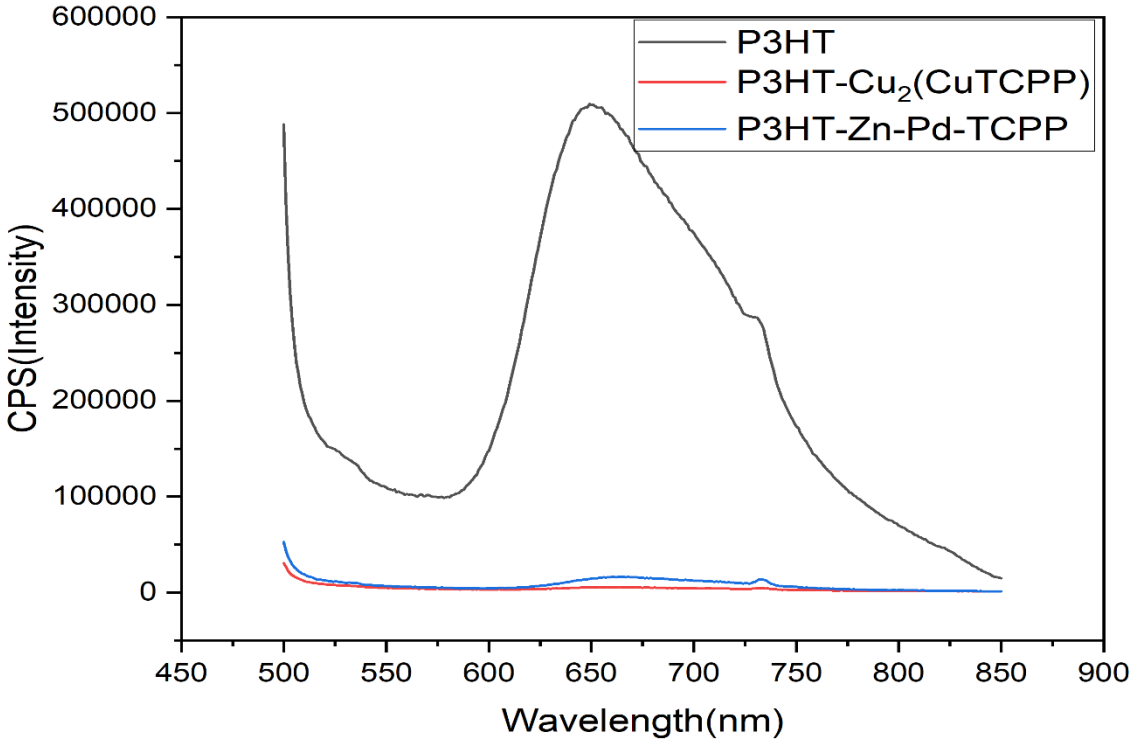

Figure 4.8 Photoluminescence (PL) spectra of thin films of pristine P3HT and P3HT-Cu_2(CuTCPP) and P3HT-Zn-Pd-TCPP composite. Excited in 488nm.

To elucidate the effect of metalloporphyrin-based MON incorporation on the molecular packing behavior of P3HT films, grazing-incidence wide-angle X-ray scattering (GIWAXS) measurements were conducted in both out-of-plane and in-plane geometries, as shown in Figure 9. The out-of-plane profiles (Figure 9a) reveal clear diffraction peaks corresponding to (100) lamellar stacking ($Q \approx 0.39$ $Å^{-1}$) and π–π stacking ($Q \approx 1.47$ $Å^{-1}$), indicative of the semi-crystalline nature of P3HT. Upon blending with Cu_2(CuTCPP), the (100) peak intensity significantly increased, suggesting enhanced long-range ordering of alkyl side chains perpendicular to the substrate. Notably, the π–π stacking peak intensity also rose substantially, surpassing that of pristine P3HT and P3HT-Zn-Pd-TCPP blends. This suggests that Cu-based MONs promote stronger face-on orientation and tighter π–π stacking of the P3HT backbone, which is favorable for vertical charge transport across the HTL. By contrast, while the Zn–Pd blended film also exhibited π–π stacking features, the diffraction peaks were broader and less intense, implying more disordered or loosely packed domains.

The in-plane GIWAXS profiles (Figure 9b) further confirm these trends. The P3HT–Cu_2(CuTCPP) film displayed a pronounced peak at Q ≈ 0.53 $Å^{-1}$, attributable to enhanced in-plane lamellar ordering of P3HT chains. This may be driven by the templating effect or steric interaction of the 2D MON sheets, which guide the self-assembly of polymer domains. However, the corresponding π–π stacking peaks remained weak in the in-plane direction across all samples, indicating a dominant face-on molecular orientation, as expected for efficient vertical charge extraction in PSCs.

Taken together, the GIWAXS results demonstrate that incorporation of Cu_2(CuTCPP) MONs leads to significantly improved molecular ordering in both lamellar and π–π stacking directions, especially in the out-of-plane orientation. This enhanced structural ordering is anticipated to facilitate hole mobility by providing continuous charge transport pathways, which corroborates the improved photovoltaic performance observed in J–V.

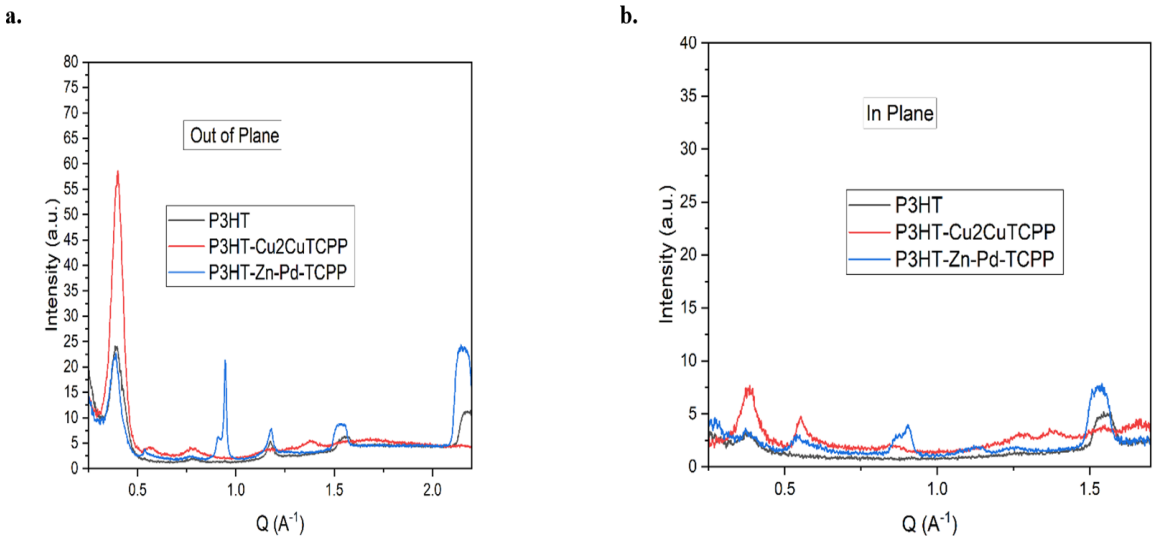

Figure 4.9 a. Out of plane GIWAXS patterns of pristine P3HT and P3HT-Zn-Pd-TCPP composite films in ITO glasses, b. In plane GIWAXS patterns of pristine P3HT and P3HT-Zn-Pd-TCPP composite films in ITO glasses

To investigate the impact of Cu_2(CuTCPP) and Zn-Pd-TCPP MONs doping on the electronic structure of the HTL, ultraviolet photoelectron spectroscopy (UPS) was

carried out on P3HT films doping with different MONs. All samples were spin-coated on pre-cleaned ITO substrates under the same conditions used in device fabrication to ensure consistency and reliability of the energy level measurements. The UPS results are summarized in Figure 10. Figure 10a shows the wide-range spectra, while Figure 10b and 10c focus on the high and low binding energy regions, respectively, which are used to determine the HOMO onset and the secondary electron cutoff.

$$E_{HOMO}=h\nu-(E_{cutoff}-E_{onset})$$

where $h\nu$ is the photon energy (21.22 eV for the Helium plasma source), E_{cutoff} is the secondary electron cutoff, and E_{onset} is the HOMO onset derived from the low binding energy region.

Table 3 the HOMO energy levels of different thin films

Thin film	HOMO energy level
P3HT	-10.52eV
P3HT-Cu_2(CuTCPP)	-8.73eV
P3HT-Zn-Pd-TCPP	-8.34eV

These results indicate a significant upward shift in the HOMO level upon doping P3HT with either type of MONs, narrowing the energy offset between the HTL and the perovskite layer (whose HOMO is typically around –5.45 eV). Although the absolute HOMO values appear deeper due to referencing to the vacuum level, the relative trend is consistent: the incorporation of MONs results in shallower HOMO levels (i.e., closer to vacuum) compared to pristine P3HT.

This improved energy alignment at the HTL/perovskite interface is expected to facilitate more efficient hole extraction and reduce energy losses during charge transfer. The stronger effect observed in the Zn–Pd–TCPP doped film suggests that the coordination environment and electronic delocalization in the bimetallic porphyrin

framework may further promote favorable interfacial energetics.

Together with the enhanced charge separation observed in PL quenching and the improved current density in J–V characteristics, the UPS results confirm that MON doping plays a critical role not only in modulating the morphological and optical properties of the HTL, but also in optimizing its electronic structure, thereby contributing to the overall enhancement in device performance.

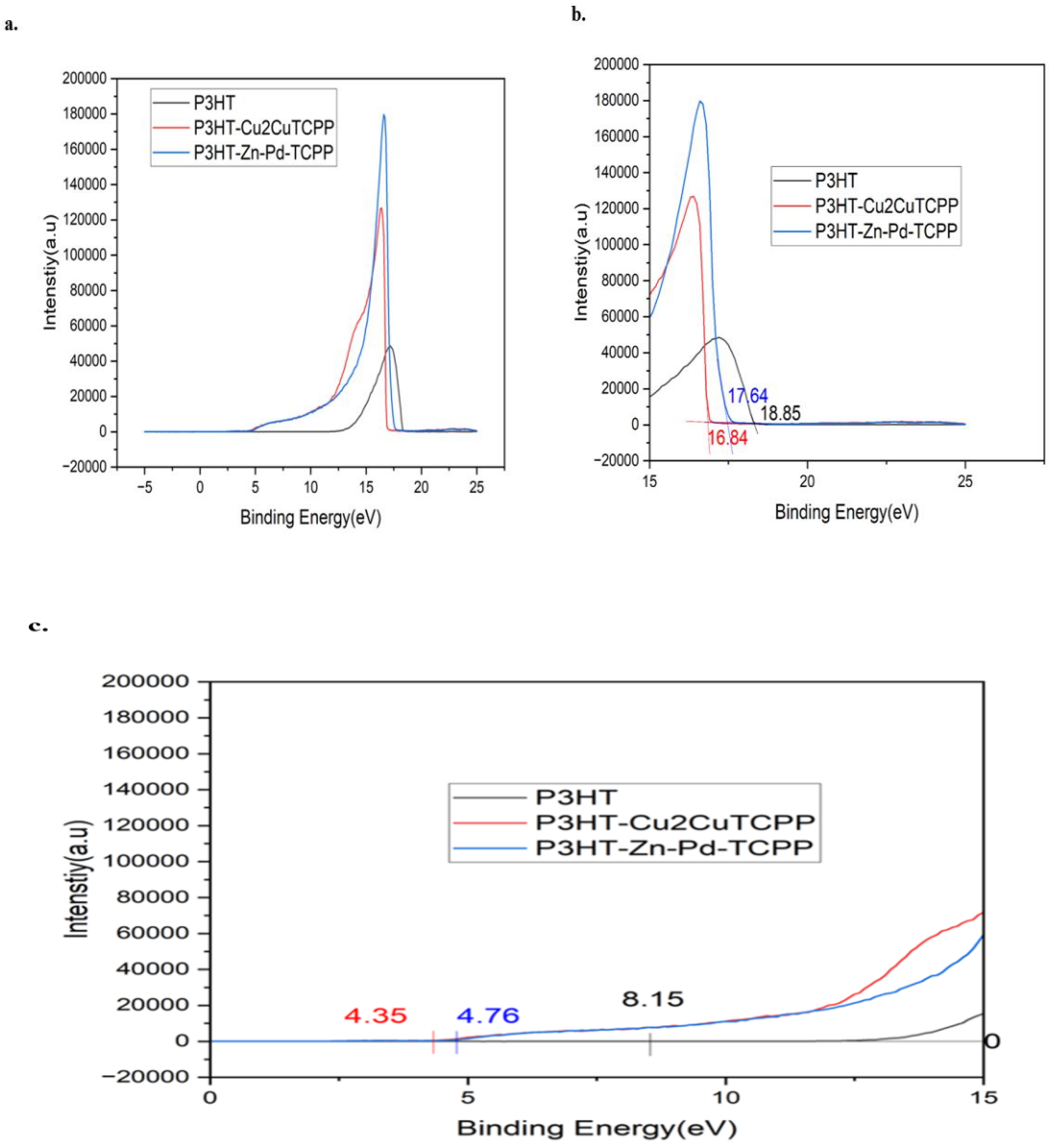

Figure 4.10 a.full UPS and high binding energy area for P3HT, P3HT-Cu_2(CuTCPP) and P3HT-Zn-Pd-TCPP MONs, b. low binding energy area forP3HT, P3HT-

Cu_2(CuTCPP) and P3HT-Zn-Pd-TCPP MONs c. high binding energy area forP3HT, P3HT-Cu_2(CuTCPP) and P3HT-Zn-Pd-TCPP MONs

4.3 Discussion

The incorporation of Cu_2(CuTCPP) and Zn–Pd–TCPP MONs into the P3HT-based HTL markedly improves the photovoltaic performance of PSCs, as demonstrated through comprehensive morphological, structural, and optoelectronic characterizations.

AFM analysis reveals that the pristine P3HT film exhibits a surface with large granular domains and significant height fluctuations, with nanodomain heights exceeding 4 nm and width variation in the range of 400–700 nm. In contrast, the addition of MONs results in a smoother and more compact film morphology. Particularly, the Cu_2(CuTCPP)-doped P3HT film displays isolated nanosheets with reduced vertical protrusions and relatively uniform lateral dispersion, while the Zn–Pd–TCPP-modified film shows even better surface uniformity and fewer aggregated domains.These improvements correlate with the observed increases in open-circuit voltage (Voc), fill factor (FF), and power conversion efficiency (PCE) in the devices incorporating MONs.

The optoelectronic properties of the MONs themselves also contribute significantly to performance enhancement. UV-vis absorption spectra indicate that Cu_2(CuTCPP) MONs exhibit a strong Soret band centered around 438 nm and Q bands near 565 and 603 nm, while Zn–Pd–TCPP MONs show absorption features at 435 and 532 nm.When incorporated into the P3HT matrix, these absorption features are retained and reflected in the external quantum efficiency (EQE) spectra. Notably, the EQE curves of the MON-doped devices exhibit a substantial enhancement in the 400–650 nm region relative to pristine P3HT, with the Zn–Pd–TCPP-based HTL showing the highest EQE response. This suggests that the MONs not only promote better film morphology but also participate actively in light harvesting, contributing to increased photocurrent density (Jsc). These findings are consistent with the measured Jsc values of 15.52 mA/cm² and 16.97 mA/cm² for Cu_2(CuTCPP) and Zn–Pd–TCPP, respectively,

compared to 17.03 mA/cm² for pristine P3HT.

Structural ordering within the HTL was further evaluated by grazing incidence wide-angle X-ray scattering (GIWAXS). In the out-of-plane direction, the (100) lamellar stacking peak of P3HT shifts and intensifies upon MON incorporation. Specifically, Cu_2(CuTCPP)-modified P3HT shows a significantly stronger lamellar stacking peak at $Q \approx 0.38$ Å^{-1}, indicating enhanced vertical ordering beneficial for out-of-plane hole transport. In contrast, Zn–Pd–TCPP incorporation also increases peak intensity but to a lesser extent, suggesting improved but comparatively less pronounced structural alignment. The in-plane scattering profiles reveal enhanced π–π stacking ($Q \approx 1.65$ Å^{-1}) in both MON-doped films, with Zn–Pd–TCPP yielding the most intense diffraction signal. These structural modifications suggest that MONs can act as nucleating agents, facilitating molecular self-organization and enhancing carrier mobility in P3HT HTL.

Photoluminescence (PL) quenching provides additional evidence for improved charge transfer dynamics. Compared to pristine P3HT, both MON-modified films exhibit significantly reduced PL intensity, with the Zn–Pd–TCPP-doped sample showing the strongest quenching. This suppression of radiative recombination indicates more efficient exciton dissociation and hole extraction at the HTL/perovskite interface. These observations are consistent with the superior Voc and FF values in the Zn–Pd–TCPP device, which reached 0.92 V and 53.2%, respectively, leading to a PCE of 8.99%.

UPS analysis provides direct evidence of energy-level modulation induced by MON doping. The incorporation of Cu_2(CuTCPP) and Zn–Pd–TCPP leads to a pronounced upward shift in the HOMO level relative to pristine P3HT, narrowing the energy offset between the HTL and the perovskite absorber. This shallower HOMO position facilitates hole extraction and minimizes energy loss during charge transfer. The larger shift observed for Zn–Pd–TCPP can be attributed to its bimetallic coordination and enhanced π-delocalization, which likely strengthen electronic coupling at the interface.

Together, these results suggest that Cu_2(CuTCPP) and Zn–Pd–TCPP MONs serve as

multifunctional dopants that enhance film morphology, improve molecular ordering, extend light absorption, and facilitate interfacial charge separation. Their integration into the P3HT HTL yields simultaneous improvements in Voc, Jsc, FF, and PCE, with Zn–Pd–TCPP showing the greatest overall enhancement, underscoring its potential as a promising additive for future perovskite solar cell architectures.

4.4 Conclusion

In summary, these results demonstrate that both Cu_2(CuTCPP) and Zn–Pd–TCPP MONs act as effective additives for enhancing the performance of polymeric P3HT-based HTLs. Their incorporation leads to substantial improvements in film morphology, molecular ordering, light absorption, and interfacial energy level alignment. These combined effects significantly enhance charge extraction and transport resulting in marked improvement in device performance. The power conversion efficiency (PCE) increasing from 4.76% (pristine P3HT) to 7.36% in Cu_2(CuTCPP)-modified devices and further to 8.99% in Zn–Pd–TCPP-modified devices. This is attributed to the synergistic effects of enhanced molecular ordering, improved film morphology, and most importantly the favorable realignment of the HOMO energy level induced by the specific metal centers, which collectively facilitate more efficient hole extraction and suppressed interfacial recombination. These results highlight that the decisive factor governing performance enhancement is the modulation of interfacial energetics through metal-ion selection, with Zn–Pd–TCPP demonstrating the strongest effect due to its superior charge transfer capability. This finding not only establishes a clear design principle for engineering 2D MON-based HTLs in perovskite devices but also suggests promising directions for future optimization, including the exploration of alternative metal centers such as Ni^{2+}, Co^{2+}, or Pt^{2+} that could further fine-tune energy-level alignment. Beyond PSCs, such nanosheets hold potential for broader application in other high-performing optoelectronic devices, including organic solar cells, light-emitting diodes, and photodetectors, where interfacial charge management is equally critical.

These findings underscore the potential of 2D porphyrin-based MONs as promising HTL dopants for advancing the efficiency and stability of next-generation perovskite solar cell architectures.

4.5 Materials and Methods Precursor materials preparation

Materials and analysed according to methods outlined in chapter 3

Zinc nitrate and Cu nitrate were both obtained from Thermo Scientific

Synthesis and physical characterization of Cu_2(CuTCPP) and Zn-Pd-TCPP MONs

Cu_2(CuTCPP) MONs were synthesized via a modified method based on work by Sasitharan et al.[15]. H_2TCPP (23.7 mg, 0.03 mmol), $Cu(NO_3)_2 \cdot 3H_2O$ (21.6 mg, 0.03 mmol), DMF (4.5 mL), and ethanol (1.5 mL) were mixed and heated at 80 °C for 24 h. The resulting purple crystals were collected by centrifugation at 4500 rpm for 10 min and washed with ethanol until the supernatant was clear)

To exfoliate Cu_2(CuTCPP) MOF into 2D MONs, 20 mg of the MOF was dispersed in 4 mL of ethanol using a vortex mixer for 30 s. The mixture was sonicated for 60 min in a Fisherbrand Elmasonic P 30H bath (80 kHz, 100% power, 16–20 °C) using sweep mode, while continuously stirred with an overhead stirrer. The suspension was then centrifuged at 1500 rpm for 10 min to remove unexfoliated materials.

Zn-Pd-TCPP was prepared by a two-solution approach. In vial A, $Zn(NO_3)_2 \cdot 3H_2O$(2.4mg, polyvinylpyrrolidone (PVP 10mg), and trifluoroacetic acid (TFA 1.0 M, 40 μL) were dissolved in a mixed solvent of DMF (9 mL) and ethanol (3 mL). Separately, in vial B, palladium (II) meso-tetra(4-carboxyphenyl) porphyrin (Pd-TCPP 4.4mg) was dissolved in a mixture of DMF (3 mL) and ethanol (1 mL). The solution in vial B was added into vial A under stirring. The resulting mixture was sonicated for 10 minutes and then heated at 80 °C for 24 hours. The resulting precipitate

was washed by centrifuge twice at 9,500 rpm with ethanol and then dried at 60 °C.

Fabrication of PSCs according to methods outlined in chapter 3

Reference

1. J. Nicks, K. Sasitharan, R. R. Prasad, D. J. Ashworth and J. A. Foster, *Adv. Funct. Mater.*, 2021, *31*, 2103723.

2. M. Wang, R. Dong and X. Feng, *Chem. Soc. Rev.*, 2021, *50*, 2764–2793.
3. D. J. Ashworth and J. A. Foster, *J. Mater. Chem. A*, 2018, *6*, 16292–16307.
4. H. Tan, Y. Zhou, S. Z. Qiao and H. J. Fan, *Mater. Today*, 2021, *48*, 270–284.
5. J. Wang, Z. Song, M. He, Y. Qian, D. Wang, Z. Cui, Y. Feng, S. Li, B. Huang, X. Kong and J. Han, *Nat. Commun.*, 2024, *15*, 2125.
6. A. Uscategui-Linares, H. Szalad, J. Albero and H. García, *Nanoscale Adv.*, 2024, *6*, 5971–5977.
7. F. Y. Liang, H. W. Huang, Y. C. Chen and P. J. Huang, *Energy Fuels*, 2025, *39*, 6533–6548.
8. R. Saha and C. J. G. García, *Chem. Soc. Rev.*, 2024, **53**, 11659–11694.
9. M. Nie, Z. H. Xue, H. Sun, J. M. Liao, F. J. Xue and X. X. Wang, *Int. J. Hydrogen Energy*, 2020, 45, 28870–28875.
10. H. Veisi, M. Abrifam, S. A. Kamangar, M. Pirhayati, S. G. Saremi, M. Noroozi, T. Tamoradi and B. Karmakar, *Sci. Rep.*, 2021, 11, 21883.
11. Z. A. Sandhu, M. A. Raza, N. S. Awwad, H. A. Ibrahium, U. Farwa, S. Ashraf, A. Dildar, E. Fatima, S. Ashraf and F. Ali, *Mater. Adv.*, 2024, 5, 30–50.
12. E. Miguel-Casan, M. D. Darawsheh, V. Fariña-Torres, I. J. Vitórica-Yrezábal, E. Andres-Garcia, M. Fañanás-Mastral and G. M. Espallargas, *Chem. Sci.*, 2023, 14, 179–185.
13. Y. Hidalgo-Rosa, M. Saavedra-Torres, B. D. Koivisto, M. A. Treto-Suárez, D. Páez-Hernández, X. Zarate and E. Schott, *Inorg. Chem. Commun.*, 2025, *172*, 113635.
14. J. H. Kim, S. Wu, L. Zdrazil, N. Denisov and P. Schmuki, *Angew. Chem., Int. Ed.*, 2024, 63, e202319255.
15. B. Le Ouay, H. Takaya and T. Uemura, *J. Am. Chem. Soc.*, 2019, **141**, 14549–14553.
16. K. Sasitharan, J. Frisch, J. Kuliček, A. Iraqi, D. G. Lidzey, M. Bär, B. Rezek and J. A. Foster, *Sci. Rep.*, 2024, 14, 29559.

17. F. Cheng, R. He, S. Nie, C. Zhang, J. Yin, J. Li, N. Zheng and B. Wu, *J. Am. Chem. Soc.*, 2021, 143, 5855–5866.

Chapter 5: Conductive 2D metal-organic nanosheets to enhance hole transport within perovskite solar cells.

5.1 Introduction

Two-dimensional conductive metal-organic Nanosheets (2D cMONs), characterized by extended π–d conjugated planar structures, represent a promising class of materials for next-generation optoelectronic applications due to their intrinsic electrical conductivity. These 2D cMONs are typically constructed from transition metals such as Ni, Cu, Co, and Fe, whose unfilled d-orbitals can conjugate with the π-electron systems of organic ligands to form delocalized electron domains, thereby facilitating charge delocalization and transport.[1]

The choice of metal centre significantly influences the conductivity of the resulting MOFs. For instance, the electrical conductivities of Ni-HITP, Cu-HITP, and Co-HITP (where HITP is2,3,6,7,10,11-hexaaminotriphenylenevary) greatly, with values of 55.4, 0.75, and 0.024 S cm^{-1}, respectively.[2] This suggests that by carefully tuning the metal core, the electronic properties of 2D cMONs can be optimized for specific device applications.

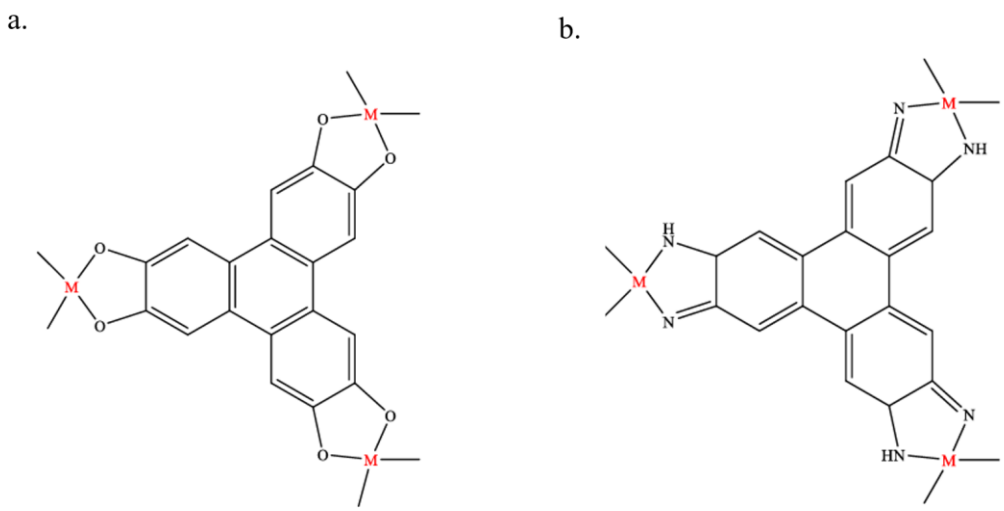

Figure 5.1 Structure of a.M-HHTP and b.M-HITP

Equally important is the role of the organic linker, often composed of π-conjugated aromatic compounds such as 2,3,6,7,10,11-hexahydroxytriphenylene (HHTP), HITP, or 2,3,7,8,12,13-hexahydroxytricycloquinazoline (HHTT). These linkers provide extended conjugation across the 2D lattice, enabling effective π–π stacking and facilitating in-plane charge transport.[3] Recent developments have demonstrated that structural modification of the organic ligands can further enhance the conductivity of the frameworks. For example, Cu-HHTC and Cu-EP MOFs, constructed with newly designed HHTT and EP ligands, achieved conductivities of 3.0×10^{-3} S cm-1 and 1.0×10^{-3} S cm-1, respectively.[4]

Importantly, unlike conventional MOFs, which are typically insulating, 2D cMONs exhibit narrow bandgaps (~1 eV) and extended conjugation, enabling both light absorption in the visible range and efficient charge separation.[5,6] These properties make them ideal candidates for integration into optoelectronic devices, such as field-effect transistors (FETs), photodetectors, and especially PSCs.

Recent studies have demonstrated the potential of 2D cMONs as HTL in PSCs. Wang et al.[7] successfully employed $Ni_3(HITP)_2$ MONs as a dopant-free HTL in an ITO/$Ni_3(HITP)_2$/$CH_3NH_3PbI_3$/PCBM/Ag device architecture, achieving a power conversion efficiency (PCE) of 10.3%.

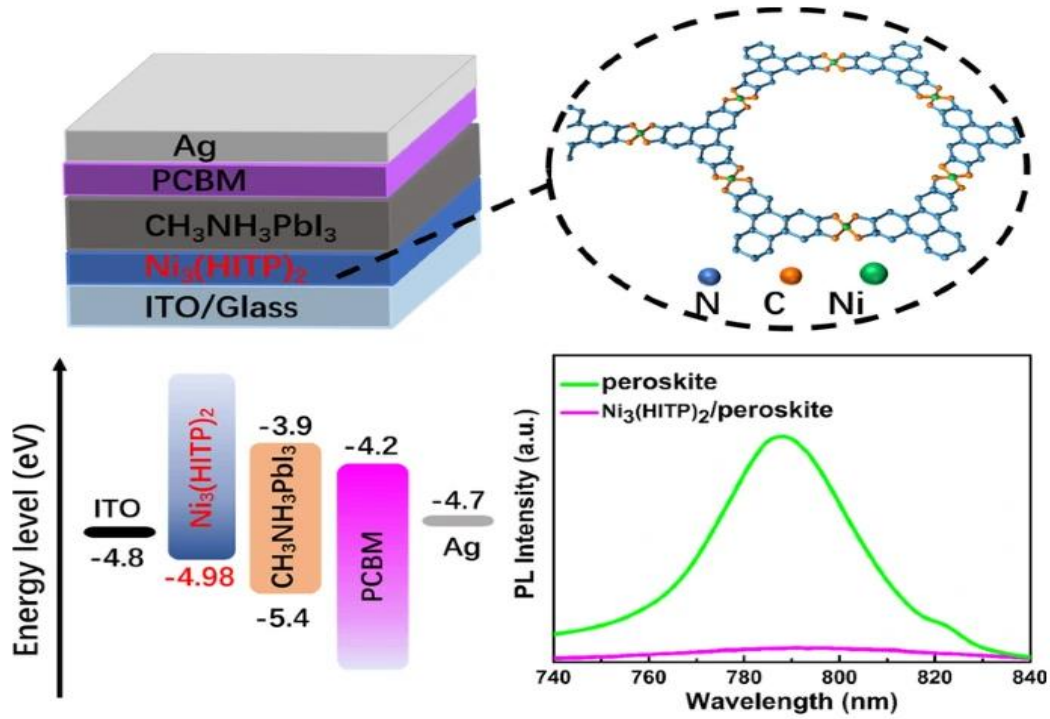

Figure 5.2. The structure of solar cells and Ni3(HITP)2 2D cMONs, energy level of the solar cells and the PL test of the devices (Wang et al[7])

Similarly, $Cu_3(HHTT)_2$ Metal organic nanosheets (MONs) were integrated into inverted PSCs (ITO/HTL/perovskite/PCBM/BCP/Ag) and demonstrated improved efficiency (20%) compared to conventional NiOx-based devices (18%).[8] These results underline the ability of 2D cMONs to not only replace traditional HTL materials but also enhance device performance. Enhance both power conversion efficiency and long-term device stability, paving the way for more efficient and cost-effective photovoltaic technologies.

Building on the findings from Chapters 3 and 4, which demonstrated that porphyrin-based nanosheets can enhance the crystallinity of P3HT and modulate its band gap—thereby improving solar cell performance—we propose that incorporating two-dimensional (2D) conductive metal-organic frameworks could further enhance device efficiency by directly improving hole mobility. Given their extended π-conjugated structures and intrinsic electrical conductivity, 2D conductive MONs offer a promising pathway to facilitate faster and more efficient charge transport within HTL.

In this study, we selected two representative families of 2D cMONs: M–HHTP and M–HITP. These materials were chosen due to their high reported hole mobilities and the strong π–d orbital interactions between the metal centres and organic ligands, which support efficient charge delocalization. By integrating these MONs with P3HT, we aim to combine the favourable morphological and electronic properties of both components, thereby achieving improved hole transport and enhanced power conversion efficiency in PSCs.

5.2 Results

5.2.1 Synthesis and characterization of the HHTP group and HITP group 2D cMONs

MHHTP nanosheets were synthesized according to the previous method by Liu et al. [9] Briefly, MHHTP was heated with nickel acetate, copper acetate, and cobalt acetate in a DMF: water mixture at 85 °C for 24 h to produce 2D MONs as black microcrystalline powder. X-ray powder diffraction (XRPD), verifying the structural integrity of the synthesized 2D MONs. Elemental analysis established the molecular composition as $C_{36}H_{12}O_{12}X_3$(where X= Ni, Cu, Co), hereafter referred to as M-HHTP (where M= Ni, Cu, Co) MONs. UV–Visible (UV-Vis) absorption spectroscopy was used to characterize the electronic transitions of the framework, while Fourier-transform infrared (FT-IR) spectroscopy provided complementary information on functional groups and coordination modes. Together, these techniques confirmed the successful and reproducible synthesis of the desired 2D MONs.

M-HITP (where M = Ni and Cu) MONs was synthesized following the same procedure reported by Liu et al. [9] Typically, M-HITP MONs were prepared by mixing nickel acetate, copper sulfate, and 2,3,6,7,10,11-hexaaminotriphenylene (HATP·6HCl) in a preheated solvent mixture of DMF and DMA at 65 °C. Subsequently, an aqueous solution of sodium acetate (NaOAc, 2 mol dm^{-3}) and water was added, and the resulting mixture was further heated at 65 °C for 2 hours to complete the synthesis.

To confirm the successful formation and reproducibility of M-HiTP MONs, the same characterization techniques used for M-HHTP were employed. XRPD verified the structural integrity of the synthesized nanosheets. The molecular formula $C_{24}H_{30}N_6X_3$ (where X = Ni or Cu), as determined by elemental analysis, confirmed the expected composition of the synthesized material. UV–Visible (UV-Vis) absorption spectroscopy and Fourier-transform infrared (FT-IR) spectroscopy were conducted to characterize the electronic transitions and functional groups, respectively. These analyses collectively confirmed the successful synthesis of the target 2D MONs.

AFM analysis revealed notable differences in morphology among the three M-HHTP MON systems. Ni-HHTP nanosheets displayed relatively uniform lateral dimensions in the range of 75–200 nm, with measured thicknesses between 5–7 nm, indicating the presence of few-layer structures rather than bulk aggregates. In contrast, Co-HHTP MONs exhibited significantly greater thickness, reaching up to ~45 nm, with lateral sizes exceeding 1 μm in some cases, consistent with less effective exfoliation and stronger interactions. Cu-HHTP nanosheets showed a broader height distribution (2–9 nm) and lateral dimensions ranging from 100 to 300 nm, suggesting a mixed population of monolayer and multilayer domains. These morphological variations likely reflect differences in metal-ligand coordination strength and interlayer packing across the series. Despite differences in thickness, the aspect ratios across all samples remained in the approximate range of 10–20, supporting their classification as 2D nanosheet systems suitable for thin-film integration.

a.

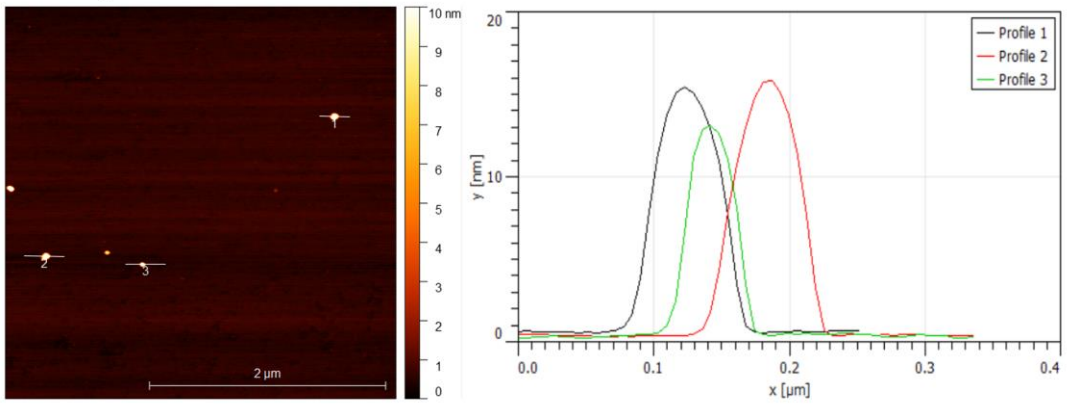

b.

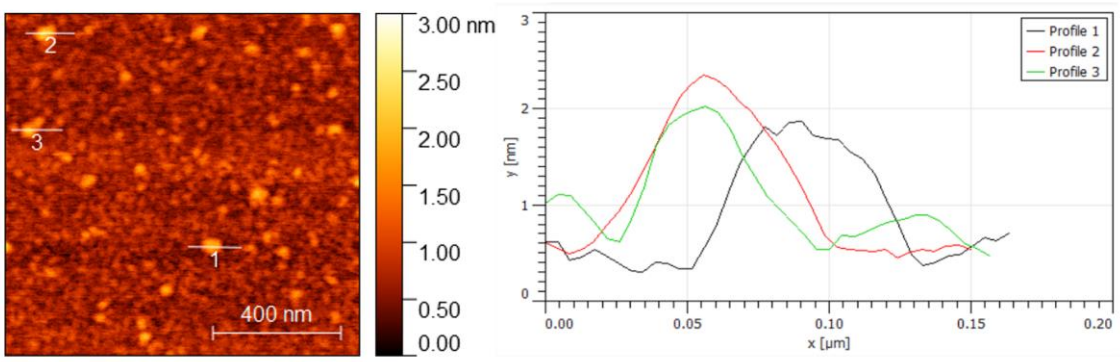

c.

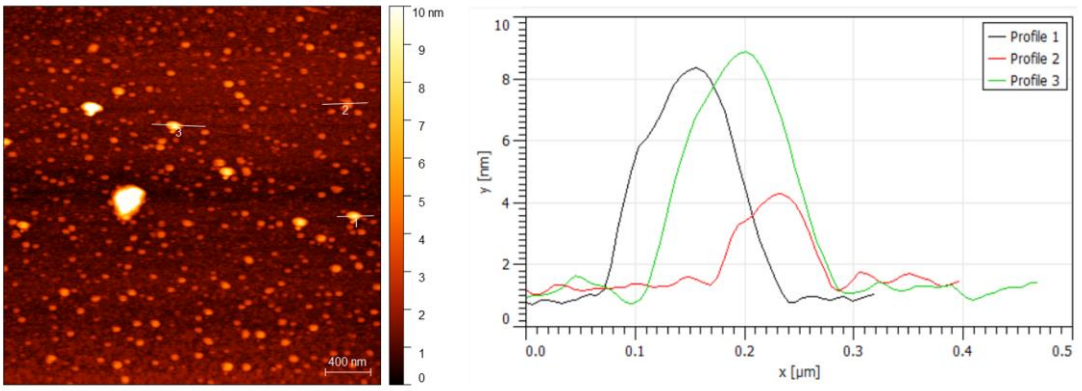

Figure 5.3. AFM of synthesised a. Ni-HHTP, b. Co-HHTP, c. Cu-HHTP 2D cMONs

a.

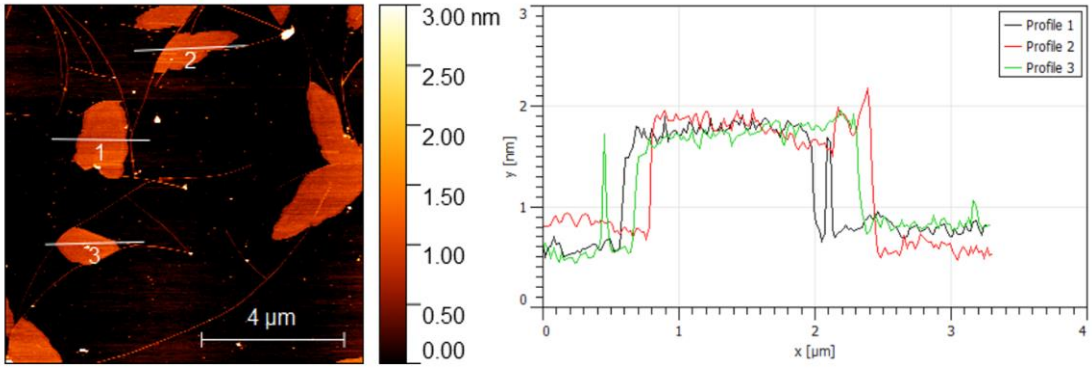

b.

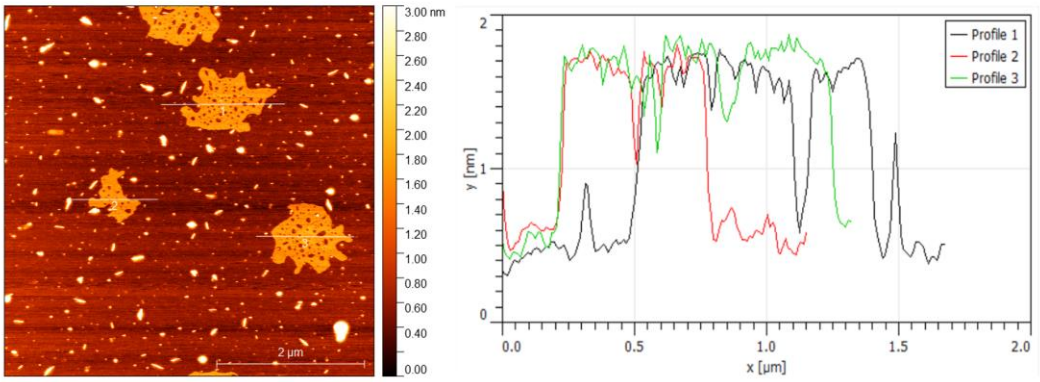

Figure 5.4. AFM of synthesised a. Ni-HITP, b. Cu-HITP 2DcMONs

AFM analysis was further conducted to examine the morphology of the HITP-based 2D cMONs. Ni-HiTP nanosheets exhibited well-defined thicknesses in the range of 1–2 nm, with lateral dimensions around100-200 nm, as evidenced by the sharp and symmetric height profiles. This suggests the successful formation of few-layer 2D structures with high uniformity and minimal surface aggregation. Cu-HITP nanosheets displayed significantly thinner profiles as well, with heights ranging from approximately 1 to 2 nm. The lateral dimensions extended up to 200 nm, indicating the presence of ultrathin monolayer or bilayer sheets with relatively large lateral spreading. The narrow height distribution and flat surface morphology observed in both systems suggest that the synthetic and washing processes effectively preserved the 2D architecture of the MONs, making them promising candidates for applications requiring atomic-level thickness control, such as nanoelectronics or interfacial transport layers in optoelectronic devices.

Elemental analysis was employed to further verify the structural integrity and elemental composition of the synthesized M-HHTP and M-HiTP MONs. For the M-HHTP group, the theoretical carbon content of $C_{36}H_{12}O_{12}M_3$ (M = Ni, Co, Cu) ranges from 52.28% to 53.21%, with no nitrogen content expected. The experimental results showed good agreement, with carbon values of 53.12%, 52.18%, and 50.42% for the Ni-, Co-, and Cu-HHTP samples, respectively. Minor deviations in hydrogen content (rising from

~1.5% theoretical to ~2.0% experimental) may be attributed to residual solvent molecules or adsorbed moisture, while the trace nitrogen signals (~0.01%) are likely from surface contamination or instrumental noise.

In the case of M-HiTP MONs, the expected elemental composition of $C_{24}H_{30}N_6M_3$ includes ~49% C, ~5% H, and ~14% N. The measured nitrogen contents were 13.50% for Ni-HiTP and 12.47% for Cu-HiTP, closely matching the theoretical values and confirming the successful incorporation of the triazine-based ligand. Slight reductions in carbon and nitrogen percentages may reflect incomplete ligand coordination or partial oxidation during synthesis. Overall, the elemental profiles confirm that the target molecular structures were preserved, and no significant decomposition or framework disruption occurred during synthesis and purification.

Table 1 Element analysis results of the M-HHTP and M-HiTP groups.

Sample	C	H	N
Theoretical Ni-HHTP ($C_{36}H_{12}O_{12}Ni_3$)	53.21%	1.49%	0%
Synthesized Ni-HHTP MONs	53.12%	2.05%	0.01%
Theoretical Co-HHTP ($C_{36}H_{12}O_{12}Co_3$)	53.17%	1.49%	0%
Synthesized Co-HHTP MONs	52.18%	2.16%	0.01%
Theoretical value for Cu-HHTP ($C_{36}H_{12}O_{12}Cui_3$)	52.28%	1.46%	0%
Synthesized Cu-HHTP	50.42%	1.76%	0.01%

MONs			
Theoretical Ni-HiTP MONs ($C_{24}H_{30}N_6Ni_3$)	49.82%	5.23%	14.52%
Synthesized Cu-HiTP MONs	46.06 %	5.17%	13.50%
Theoretical value for Cu-HiTP MONs ($C_{24}H_{30}N_6Cu_3$)	48.60%	5.10%	14.17%

To verify the crystalline structure of the synthesized 2D cMONs, XRD analysis was performed on Ni-HHTP, Co-HHTP, and Cu-HHTP samples. As shown in Figure 3, the experimental XRD patterns are overlaid with the simulated diffraction profile generated from the reported single-crystal structure of M-HHTP (CCDC No. 2031852). Approximately 10 mg of dried sample was used for each measurement.

The experimental patterns of all three M-HHTP samples show strong agreement with the simulated data, particularly in the low-angle region. Distinct diffraction peaks at 2θ ≈ 4.7°, 9.5°, and 13.6° are clearly observed across all samples, corresponding to the (100), (200), and (210) planes of the layered framework, respectively. These reflections confirm the presence of long-range in-plane ordering and retention of the 2D structure after synthesis. While the intensity of higher-angle peaks above 20° is relatively lower and some peaks appear broadened—likely due to the nanoscale domain size and partial loss of crystallinity, the overall consistency with the simulated pattern confirms the structural fidelity of the materials.

In summary, the XRD results confirm that the synthesized M-HHTP nanosheets retain the expected 2D crystalline framework, as evidenced by the clear agreement between experimental and simulated diffraction patterns.

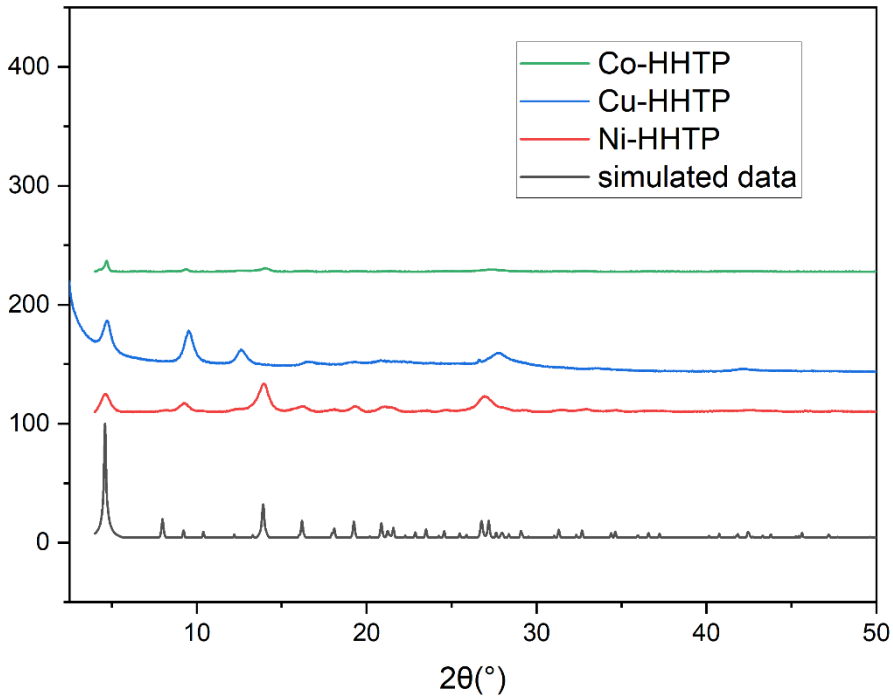

Figure 5.5. Physical characterization of XRD for M-HHTP group 2D cMONs

The optical properties of the MONs in suspension with ethanol were investigated using UV-visible spectroscopic measurements. A common feature observed across all three spectra is that the absorbance baselines do not return to zero in the longer-wavelength region. This is most likely attributed to light scattering by the suspended M-HHTP nanosheets. Due to the intrinsic poor dispersibility of M-HHTP in ethanol. Unlike molecular solutions, these 2D MON suspensions contain finely dispersed particles that scatter incident radiation, reducing the detected transmittance and giving rise to a finite apparent absorbance across the entire spectral range. Importantly, this scattering background does not compromise the assignment of the characteristic peaks, as all absorption bands remain well-resolved and reproducible relative to their local baselines.

The spectra for M-HHTP nanosheets are all characterized by metal-to-ligand charge transfer (MLCT) transitions at longer wavelengths—670 nm for Cu-HHTP (Figure 5.6b) and 600 nm for Ni-HHTP (Figure 5.6c)—which are typically associated with charge transfer from the metal centers to the conjugated ligand system. In the case of Co-HHTP (Figure 4a), the MLCT transition is not explicitly visible, but it is likely masked by the

high-intensity π–π* bands dominating the 230–400 nm region.

All three samples also show strong π–π* absorption bands, attributed to the aromatic ligand framework, appearing at ~375 nm for Co-HHTP, ~390 nm for Cu-HHTP, and ~360 nm for Ni-HHTP. These values are consistent with previous reports on 2D conductive MONs[9], indicating that the coordination environment and conjugated structure of the ligands are preserved across different metal centers. Additional high-energy peaks below 300 nm may arise from n–π* or intrigant transitions.

The reproducibility and clarity of these spectral features across the series confirm the structural consistency of the MONs in ethanol and suggest that the nanosheets retain their electronic integrity and extended π-conjugation, which is important for their application in optoelectronic or sensing systems.

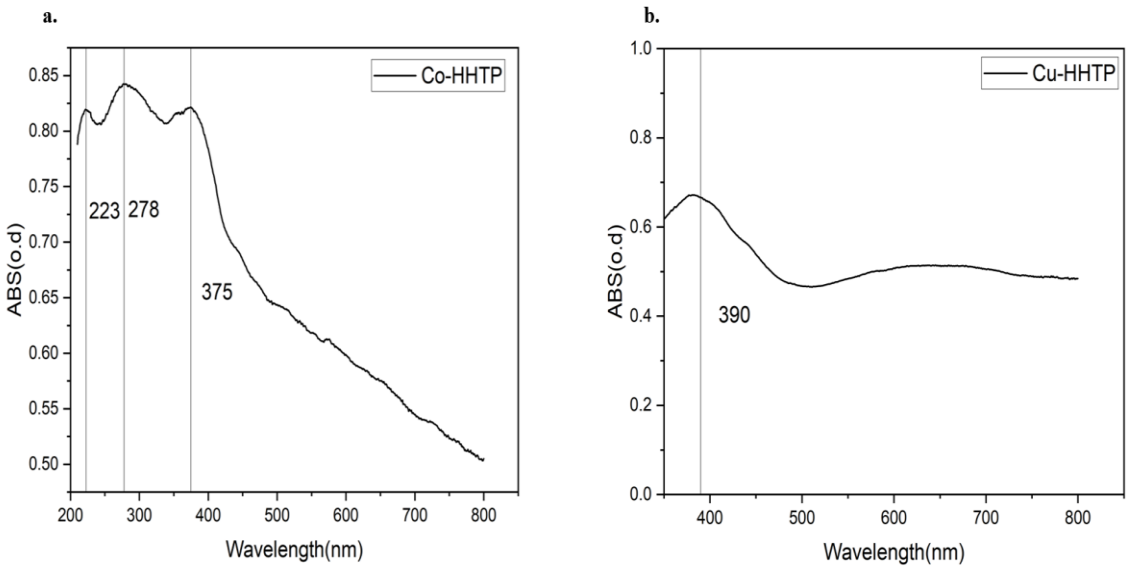

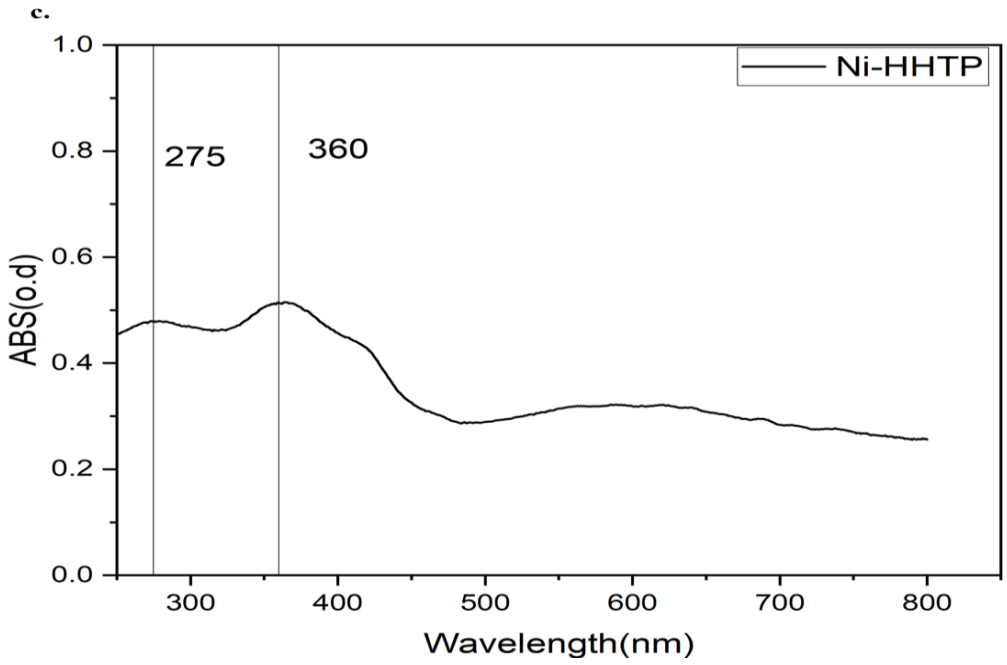

Figure 5.6. Uv-Vis spectra recorded for M-HHTP group a. Co-HHTP, b. Cu-HHTP, c.Ni-HHTP redispersed in ethanol

FT-IR analysis of the as-synthesized powders provided further confirmation that the correct products had been formed. Approximately 3 mg of each sample was used per measurement. All M-HHTP samples display a weak peak around 1730 cm^{-1}, previously attributed to an aromatic C–H overtone, as well as a broad signal between 1600–1630 cm^{-1}, which may also be related to C–H overtones or possibly aromatic C=C stretching. In addition, a series of well-defined peaks appear in the region between 1500 cm^{-1} and 1200 cm^{-1} in all metal-containing samples. These bands are assigned to in-plane C–C stretching vibrations of the aromatic ring system.

Compared to the free HHTP ligand, these peaks are shifted to slightly lower wavenumbers in the metal-coordinated materials, which we attribute to the delocalization of electron density across the 2D nanosheet plane. This reduction in vibrational frequency is consistent with extended conjugation and reduced bond order upon formation of the framework. Furthermore, the broad O–H stretching band around 3400–3000 cm^{-1} observed in all samples is likely due to adsorbed water, either from ambient moisture or residual solvent trapped within the pores. The preservation of key

ligand-based vibrational features, alongside metal-induced shifts in the fingerprint region, confirms successful coordination between the HHTP ligands and metal nodes, and supports the formation of the desired 2D M-HHTP framework.

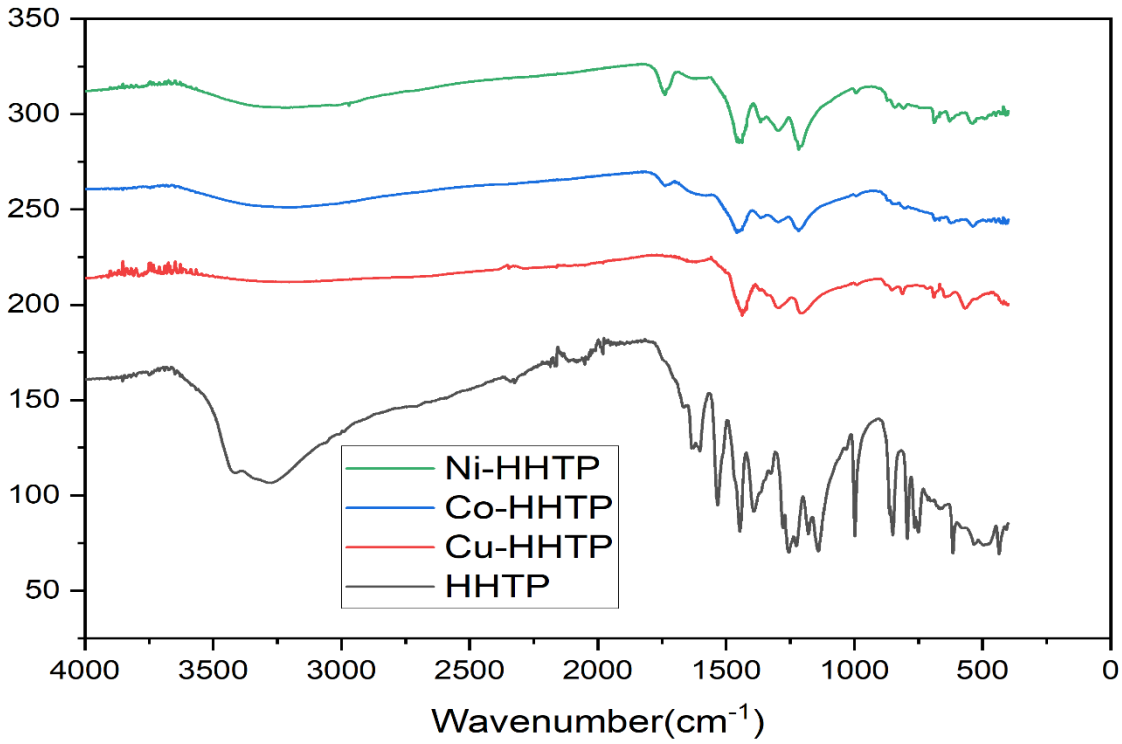

Figure 5.7 FT-IR for M-HHTP MONs and HHTP powder.

Figure 5.8 presents the structural and optical characterizations of Ni-HITP and Cu-HITP nanosheets, confirming both the successful synthesis and the distinct optical properties of the two materials.

Figure 5.8a shows the XRD patterns of Ni-HITP and Cu-HITP. The major diffraction peaks located at approximately 4.75°, 9.46°, 12.47°, 16.2°, and 27.8° are in excellent agreement with the literature data [10], indicating that both materials crystallized in the expected phase with good purity and crystallinity. The similarity in peak positions suggests that the metal center variation does not significantly alter the overall framework topology, highlighting the structural robustness of the HITP motif across different metal coordination environments.

Figure 5.8b displays the FT-IR spectra of HATP, Cu-HITP, and Ni-HITP. Upon nanosheet formation, the N–H stretching bands (2500–3500 cm^{-1}), indicative of protonated amine groups in the HATP monomer, disappear, replaced by a broad O–H absorption features likely due to adsorbed water. This spectral shift confirms substantial chemical environment changes around the nitrogen atoms during coordination. The aromatic overtone at 1730 cm^{-1} remains present in the MONs spectra, confirming the retention of the conjugated ligand backbone. For Ni-HITP, three distinct peaks appear at 1547 cm^{-1}, 1464 cm^{-1}, and 1364 cm^{-1}, assigned to in-plane C=C stretching vibrations of the aromatic rings, red-shifted relative to the monomer, likely due to extended conjugation in the 2D framework.

Figures 5.8c and 5.8d show the UV-Vis absorption spectra of Ni-HITP and Cu-HITP, respectively. Both exhibit broad absorption features below 400 nm with distinguishable plateaus around 360 nm (Ni-HITP) and 370 nm (Cu-HITP), which can be attributed to $\pi \rightarrow \pi^*$ transitions of the aromatic linker. Higher-energy features are likely associated with $\sigma \rightarrow \sigma^*$ transitions, while any possible metal-to-ligand charge transfer (MLCT) peaks at lower energies are probably obscured by the broad visible absorption tails. The overall strong visible-light absorption in both materials suggests their suitability as hole transport materials (HTMs) in optoelectronic applications.

In summary, the combined XRD, FT-IR, and UV-Vis results confirm the correct phase formation and provide insight into the distinct optical behaviors of Ni-HITP and Cu-HITP, supporting their application in device-level studies.

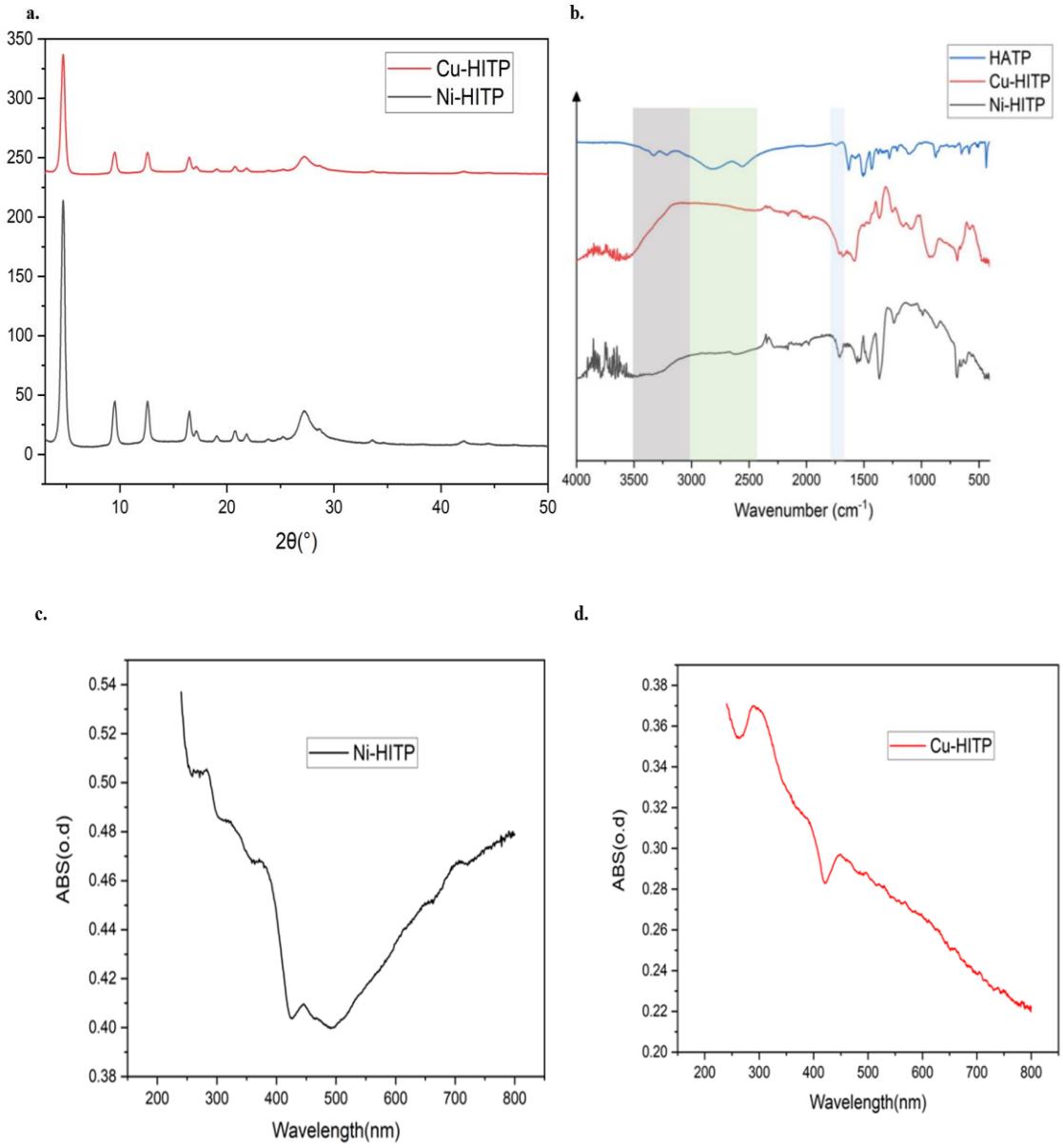

Figure 5.8. Physical characterization of a.XRD for M-HiTP, b. FT-IR for M-HiTP MONs c. Uv-Vis spectra recorded for Ni-HiTP dissolved in ethanol and d.Uv-Vis spectra recorded for Cu-HiTP dissolved in ethanol.

5.2.2 Device fabrication, optimization, and performance

Based on these findings and previous research, we incorporated 2D cMONs into the HTL to enhance hole mobility and improve charge transport efficiency in PSCs.

The device structure consists of an ITO/SnO_2/CSFAPbICl/P3HT:M-HHTP or P3HT:M-

HITP/Au configuration, where different types of 2D cMONs (M-HHTP and M-HITP) are incorporated into the P3HT layer as the HTL.

Building upon the device optimization results from Chapter 3, in which a 50 wt% loading of Zn_2(ZnTCPP) nanosheets yielded the best photovoltaic performance, we adopted this loading ratio as a baseline for evaluating other 2D cMONs. Specifically, a series of M–HHTP (M = Ni, Co, Cu) nanosheets and Ni-HITP were incorporated into HTL to fabricate corresponding perovskite solar cell devices.

The photovoltaic performance of these devices was measured under standard AM 1.5G illumination using a calibrated solar simulator, and the extracted parameters are summarized in Table 2. Compared to the pristine P3HT-based device, which exhibited a baseline power conversion efficiency (PCE) of 6.55%, all MON-containing devices demonstrated substantial performance enhancements. Among the tested materials, the device incorporating Ni–HITP achieved the highest PCE of 10.49%, demonstrating a remarkable improvement over both the control and other MON-modified devices. The device containing Ni–HHTP also showed a significant increase, reaching a PCE of 7.88%. In comparison, devices blended with Cu–HHTP and Co–HHTP exhibited moderate performance gains, with PCE values of 6.85% and 6.42%, respectively. These results clearly indicate that the integration of 2D cMONs, particularly Ni–HITP and Ni–HHTP, can significantly enhance the efficiency of PSCs. The superior performance observed for Ni–HITP may be attributed to its lower optical bandgap, enhanced molecular ordering, and improved charge transport characteristics at the HTL interface, leading to more efficient hole extraction and reduced recombination losses

Table 2 Comparative device performance using P3HT-based HTLs with and without organic linker,HHTP and HITP based 2D CMONs

No.	HTL	J_{SC} (mA/cm^2)	V_{OC}(V)	FF (%)	PCE (%)
1	P3HT±0.386	17.83±0.386	0.85±0.159	40.12±1.57	6.55±0.16
2	P3HT-HHTP	13.28±1.59	0.81±0.185	44.82±1.12	5.12±0.09
3	P3HT-HITP	14.84±0.95	1.05±0.046	68.20±1.19	9.80±0.60
4	P3HT-Ni-HHTP	18.36±1.25	0.85±0.017	47.51±0.36	7.88±0.77
5	P3HT-Co-HHTP	18.06±0.24	0.92±0.258	50.7±0.87	8.01±0.69
6	P3HT-Cu-HHTP	18.21±0.319	0.85±0.325	48.2±0.37	7.45±0.11
7	P3HT-Ni-HiTP	19.35 ±0.411	0.96±0.309	59.65±0.18	10.49±0.286
8	P3HT-Cu-HiTP	19.32±0.32	0.95±0.022	57.76±0.41	10.15±0.103

Table 2 summarizes the photovoltaic parameters of devices fabricated with pristine P3HT and various P3HT–2D cMONs composites. Devices incorporating HHTP-based nanosheets (Ni–HHTP, Co–HHTP, and Cu–HHTP) exhibited moderate improvements in PCE compared to the pristine P3HT device. Specifically, the P3HT–Ni–HHTP device achieved a PCE of 7.88%, with a Jsc of 18.36 mA cm^{-2}, Voc of 0.85 V, and FF of 47.51%. Similarly, the P3HT–Co–HHTP and P3HT–Cu–HHTP devices delivered PCEs of 8.01% and 7.45%, respectively, both surpassing the baseline PCE of 6.55% obtained from the unmodified P3HT device. These improvements are largely attributed to increases in both Jsc and FF, indicating that the incorporation of HHTP-based MONs promotes enhanced light absorption and moderately improved charge extraction. However, the relatively limited enhancement in FF suggests that charge transport within HTL is still somewhat restricted in HHTP-based systems.

In contrast, HITP-based nanosheets (Ni–HITP and Cu–HITP) led to substantially

higher device performance. The P3HT–Ni–HITP device achieved the highest PCE of 10.49%, with a Jsc of 19.35 mA cm^{-2}, Voc of 0.96 V, and an FF of 59.65%. The P3HT–Cu–HITP device also performed well, with a PCE of 10.15%. Compared to the HHTP series, the HITP-based composites exhibited more pronounced improvements across all photovoltaic parameters, particularly in FF, suggesting more efficient carrier transport and reduced internal resistance. These performance gains are further supported by optical and structural characterizations. These results collectively demonstrate that while both HHTP and HITP-based MONs can improve solar cell performance, HITP derivatives—particularly Ni–HITP—are more effective in facilitating charge transport and improving overall device efficiency.

Figure 8c displays the J–V characteristics of the champion devices based on pristine P3HT and HITP-derived composite HTLs. The pristine P3HT device delivered a PCE of 8.27% (J_{sc} = 18.32 mA cm^{-2}, V_{oc} = 0.92 V, FF = 58.61%), serving as the performance baseline. Upon incorporating HITP-based 2D cMONs, a substantial enhancement in photovoltaic behavior was achieved. The Ni–HITP–modified device exhibited a PCE of 11.13%, with Jsc= 20.02 mA cm^{-2}, Voc= 0.93 V, and FF = 59.76%, whereas the Cu–HITP–based device reached the highest efficiency of 11.73% (Jsc= 19.50 mA cm^{-2}, Voc = 0.96 V, FF = 62.15%). These results demonstrate that the incorporation of 2D HITP nanosheets into the P3HT matrix markedly enhances hole transport and charge extraction at the HTL/perovskite interface. The improved Jsc and FF, coupled with a slight increase in Voc, indicate reduced interfacial recombination losses and more balanced carrier dynamics, collectively contributing to the superior performance of the HITP-based champion devices.

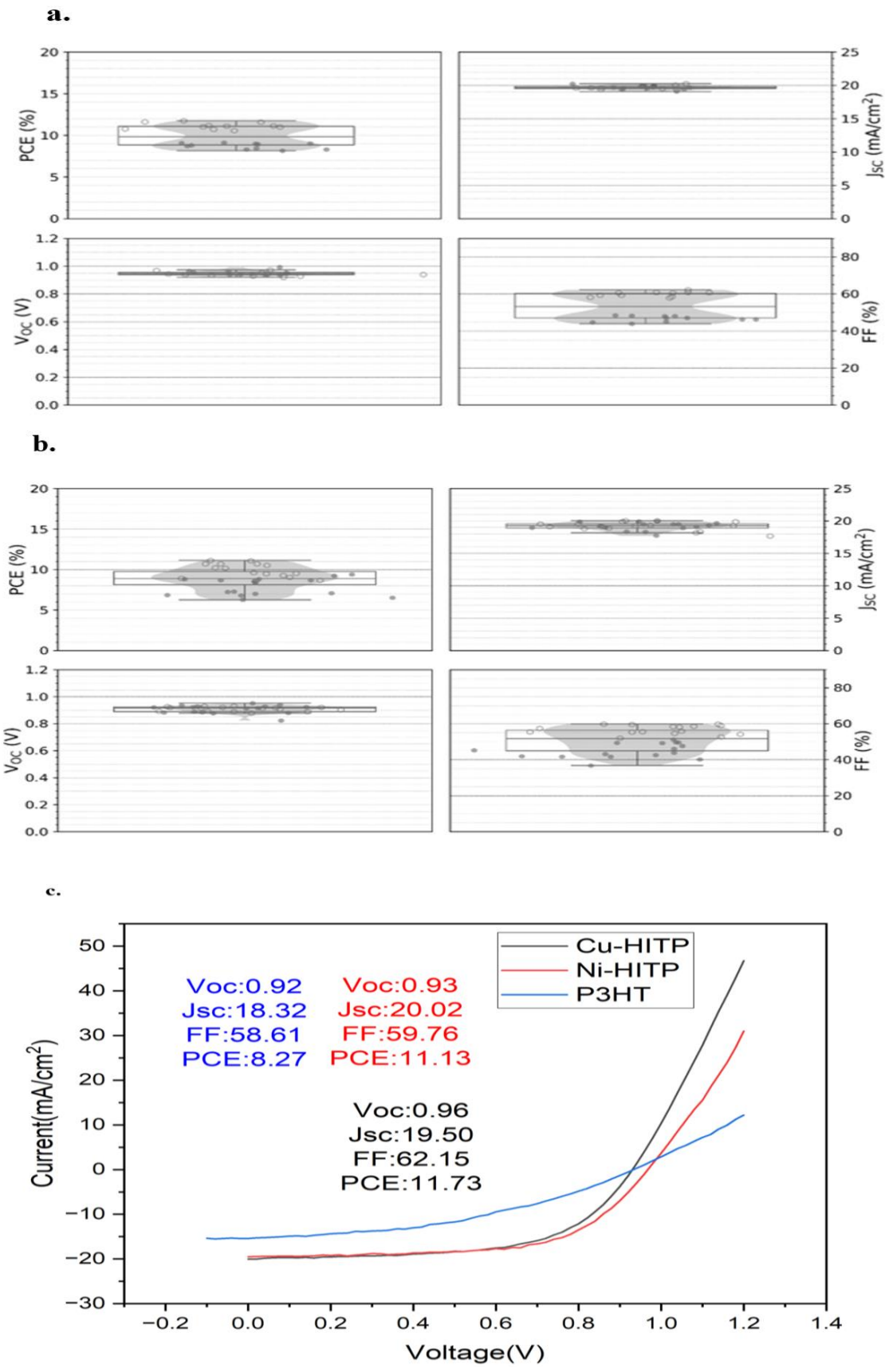

Figure 5.9. Performance of a. P3HT-Cu-HiTP devices and b. P3HT-Ni-HiTP devices

and champion devices of c. P3HT, P3HT-Ni-HTP and P3HT-Cu-HITP devices.

Given that the HHTP-based composites demonstrated relatively lower device performance compared to their HITP counterparts and showed limited advantages in J–V measurements, the EQE analysis in this study focuses primarily on the HiTP-based systems (Ni-HITP and Cu-HITP).

To further evaluate the photoresponse behavior of the devices, External Quantum Efficiency (EQE) spectra were measured and are shown in Figure 5.10. The pristine P3HT-based device displays a broad and high EQE response across the visible spectrum, with a peak approaching 80%, consistent with its strong light absorption and efficient charge collection.

Interestingly, both the P3HT–Ni-HITP and P3HT–Cu-HITP composite devices exhibit slightly reduced EQE values across most of the spectral range, despite demonstrating significant improvements in PCE, V_{oc}, and fill factor FF. This apparent discrepancy suggests that while overall charge extraction and device performance are enhanced, the quantum efficiency for converting incident photons into collected charge carriers at each wavelength has decreased.

This reduction in EQE can be attributed to several contributing factors. First, the incorporation of MONs may alter the optical properties of the active layer—such as its refractive index, absorption profile, or thickness—thus changing the optical interference conditions and photon distribution within the device. Second, although photoluminescence measurements indicate improved exciton dissociation, it is possible that the introduced MONs create localized trap states or morphological irregularities that increase non-radiative recombination in certain regions, particularly near the interface. Third, the spatial distribution and vertical connectivity of the MOF domains may influence the transport path of charge carriers, leading to suboptimal collection efficiency at specific wavelengths.

Therefore, the slight decrease in EQE should not be interpreted as a contradiction to the

improved photovoltaic performance. Instead, it highlights the complex interplay between light absorption, charge separation, and carrier transport within the composite films. The enhanced J_{sc}, V_{oc}, and FF observed in J–V measurements are likely a result of improved bulk transport and reduced recombination, which are not fully captured by EQE measurements alone.

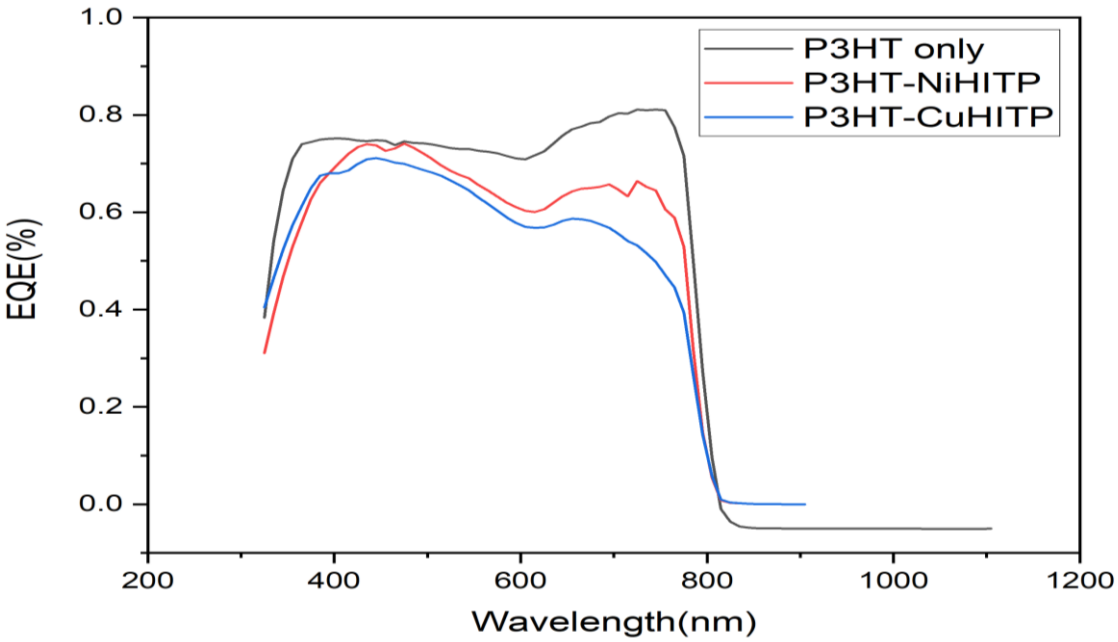

Figure 5.10 EQE of P3HT, P3HT–Ni-HITP, and P3HT–Cu-HITP Devices

5.2.3 Discussions the role of MONs addition into the P3HT Hole transport layer

Figure 5.11a presents the photoluminescence (PL) spectra of pristine P3HT and P3HT composites incorporating various M-HHTP MONs (M = Ni, Co, Cu). The measurements were conducted to investigate the influence of different nanosheet additives on exciton dynamics and interfacial charge transfer behavior in HTL.

The pristine P3HT film exhibits a strong emission peak centered around 660 nm, characteristic of its intrinsic excitonic recombination. Upon incorporating Ni-HHTP MONs, a significant enhancement in PL intensity is observed, particularly around the

main emission region. This increase in radiative recombination suggests that Ni-HHTP may inhibit efficient charge extraction, potentially due to energy level mismatch or interfacial barriers, leading to exciton accumulation and reduced quenching.

In contrast, the PL intensities of the Co-HHTP and Cu-HHTP composites are markedly quenched compared to both P3HT and the Ni-HHTP composite. This quenching behavior is indicative of improved exciton dissociation and more efficient hole extraction at the P3HT/M-HHTP interface. Among them, Cu-HHTP shows the most pronounced PL suppression, implying the most effective charge transfer interaction with the P3HT matrix.

Figure 5.11b shows the PL spectra of pristine P3HT and its composites with Ni-HITP and Cu-HITP MONs, measured under 488 nm excitation. The aim was to explore the effect of these MONs-based additives on exciton recombination and interfacial charge transfer processes in the P3HT matrix.

The pristine P3HT film displays a dominant emission peak centered around 660 nm, which is characteristic of excitonic radiative recombination in conjugated polymers. Upon blending with CuHiTP, the PL intensity is significantly quenched, although a clear emission feature remains. This partial quenching implies enhanced exciton dissociation and moderate charge transfer from P3HT to CuHiTP, suggesting improved—but not complete—hole extraction efficiency at the interface.

Remarkably, the incorporation of NiHiTP results in almost completely quenching of the PL signal across the entire spectrum. This dramatic reduction in emission intensity indicates highly efficient non-radiative decay pathways, likely due to ultrafast charge transfer between P3HT and the NiHiTP framework. Such strong PL suppression reflects the excellent ability of NiHiTP to extract holes from the P3HT layer, potentially due to favorable energy level alignment and strong electronic coupling at the heterojunction.

Overall, the PL intensity trend (P3HT > P3HT–CuHiTP ≫ P3HT–NiHiTP) highlights the superior interfacial charge transfer capability of NiHiTP among the two tested

MONs additives. These findings align with the expected improvements in charge transport and device performance in P3HT-based optoelectronic systems incorporating conductive 2D MONs

Overall, these findings underscore the dual role of metal center identity and ligand coordination environment in governing interfacial charge transfer processes. While Cu-HHTP and Ni-HITP each demonstrate strong PL quenching and favorable charge extraction behavior, their mechanisms may differ: Cu-HHTP likely benefits from optimal energetic offset, while Ni-HITP may leverage its intrinsic electronic conductivity and planar structure for efficient charge delocalization. These insights provide a rational basis for tailoring MONs-based HTL materials to optimize optoelectronic performance in hybrid photovoltaic devices.

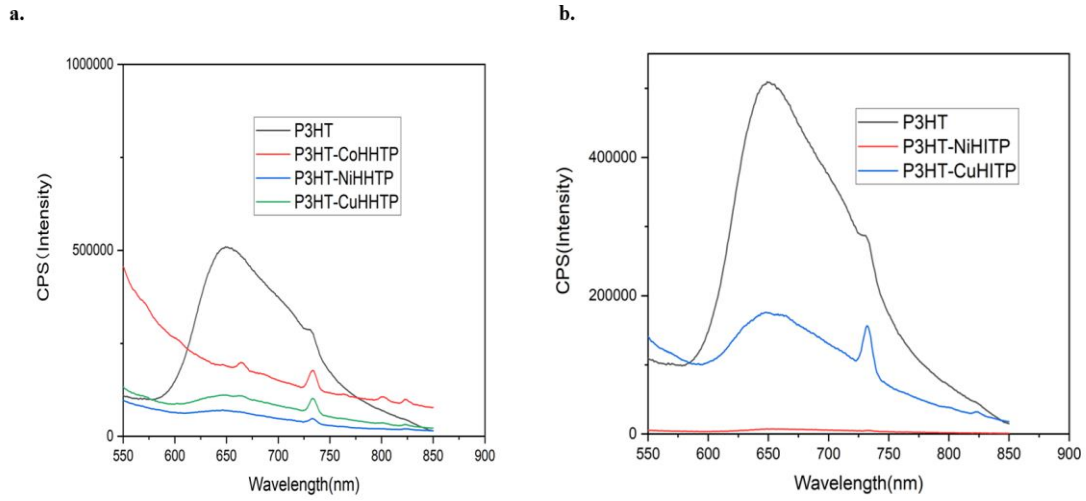

Figure 5.11 a. PL spectra of thin films of pristine P3HT and P3HT-M-HHTP composite, and b. PL spectra of thin films of pristine P3HT and P3HT-M-HITPcomposite.

In highly crystalline materials, characteristic peaks in the Raman spectrum are typically narrower and more intense. Therefore, by comparing the Raman spectra of P3HT and P3HT–MON composite films, valuable insights into the crystallinity of P3HT can be obtained. P3HT and P3HT–MON thin films were prepared under identical spin-coating conditions and characterized using Raman spectroscopy, with a 532 nm laser source at

10% laser intensity.

As shown in Figure 5.12, the pristine P3HT film exhibits prominent vibrational bands at approximately 1446 cm^{-1} and 1380 cm^{-1}, corresponding to C═C and C–C stretching modes within the thiophene rings, respectively [11]—features predominantly associated with in-plane skeletal vibrations of the conjugated backbone.

Upon incorporation of HHTP-based 2D cMONs, all characteristic Raman peaks of P3HT became sharper and more intense, indicating enhanced molecular ordering and improved crystallinity. Among the tested MONs, Co–HHTP demonstrated the most pronounced enhancement in Raman peak sharpness and intensity, followed by Cu–HHTP and then Ni–HHTP.

This trend is consistent with the previously observed device performance, particularly the fill factor (FF) values obtained from solar cell measurements. Devices incorporating Co–HHTP exhibited the highest FF (50.7%), while Cu–HHTP and Ni–HHTP achieved slightly lower FF values of 48.2% and 47.6%, respectively. These results suggest a strong correlation between the degree of molecular ordering, as reflected in Raman spectroscopy, and the charge transport efficiency of the corresponding solar cells.

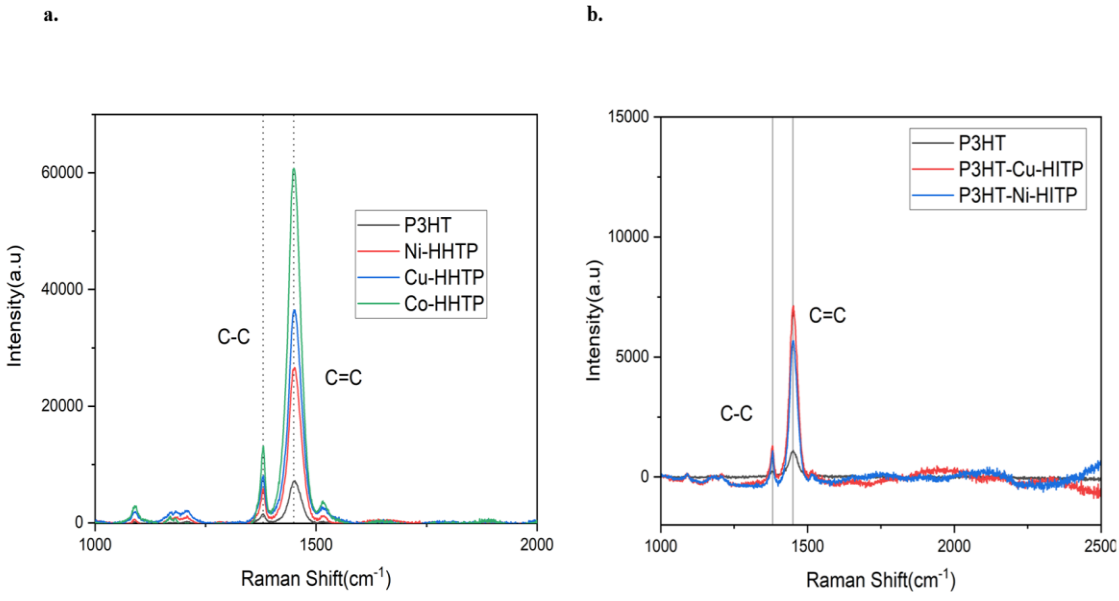

Figure 5.12 a. Raman Spectra of P3HT only and P3HT-M-HHTP MONs (5mg ml^{-1}) in

ITO glasses and b. Raman Spectra of P3HT only and P3HT-M-HITP MONs (5mg ml^{-1}) in ITO glasses using 532nm laser source and 10% intensity

To investigate the influence of 2D cMONs on the crystallization behaviour of conjugated polymers, grazing incidence wide-angle X-ray scattering (GIWAXS) was conducted on thin films to obtain structural information in both the out-of-plane and in-plane directions (Figure 5.13 a and b).

In the out-of-plane GIWAXS profiles (Figure 8a), all P3HT–MON composite films exhibit a prominent diffraction peak at Q ≈ 0.38–0.40 $Å^{-1}$, corresponding to the (100) lamellar stacking of P3HT side chains. This peak reflects the regular arrangement of alkyl chains perpendicular to the substrate, which is crucial for establishing long-range order in semicrystalline polymer systems. Among all samples, the P3HT–NiHITP composite film shows the most intense (100) diffraction peak, indicating a significant enhancement in lamellar ordering compared to pristine P3HT. This suggests that NiHITP nanosheets act as an effective structural modulator, promoting higher degrees of molecular organization.

The P3HT–CoHHTP and P3HT–CuHHTP composites also show slightly increased (100) peak intensities relative to pristine P3HT, suggesting moderate improvement in side-chain ordering. However, the enhancement is not as pronounced as that observed in the NiHITP composite, implying a weaker interaction or less templating effect from these specific MONs. In contrast, the P3HT–NiHHTP composite exhibits minimal change in (100) peak intensity compared to pristine P3HT, indicating limited influence on polymer chain alignment along the out-of-plane direction.

At higher Q values (~1.52 $Å^{-1}$), a broad peak associated with π–π stacking interactions among conjugated P3HT backbones is visible in all samples, except for Co-HHTP. Supporting the notion of enhanced ordering not only in sidechain packing but also in backbone alignment. The predominance of this π–π stacking in the out-of-plane profile, further confirms that the P3HT chains adopt a face-on orientation relative to the

substrate—a favourable configuration for vertical hole transport in photovoltaic devices.

In the in-plane GIWAXS figure (Figure 8b), a significant diffraction peak appears at Q ≈ 0.38 $Å^{-1}$ in all samples, corresponding to the (100) lamellar stacking of P3HT side chains aligned parallel to the substrate. Among them, the P3HT–NiHITP composite film exhibits a dramatically intensified (100) peak, much higher than that of pristine P3HT or other MON-blended films. This indicates that the incorporation of NiHITP nanosheets strongly promotes in-plane ordering of the P3HT chains, potentially through a templating or self-assembly effect driven by the planar geometry and π-conjugated structure of the 2D MONs. The enhanced in-plane lamellar ordering suggests improved molecular packing and better film morphology, which are beneficial for lateral charge percolation and uniform film coverage. However, like the out-of-plane observations, the π–π stacking peak at Q ≈ 1.52 $Å^{-1}$ is either weak or negligible in the in-plane direction for all samples. This implies that the π–π interactions among conjugated backbones are not aligned within the substrate plane, but rather oriented in the vertical direction, confirming a predominant face-on orientation of P3HT chains. Notably, other MON-blended samples (Co-HHTP, Cu-HHTP, Ni-HHTP) show only moderate or negligible increases in (100) peak intensity compared to pristine P3HT, indicating that the degree of in-plane ordering enhancement is strongly dependent on the specific metal centre and organic ligand structure of the incorporated MONs. The superior effect of Ni-HITP highlights its potential as a structural modulator for improving the crystalline and orientation of P3HT within the HTL. Together with the out-of-plane GIWAXS results, these in-plane observations confirm that Ni-HITP incorporation not only promotes lamellar stacking in multiple directions but also induces a favourable face-on alignment that supports vertical hole transport, a key factor in achieving high-efficiency PSCs.

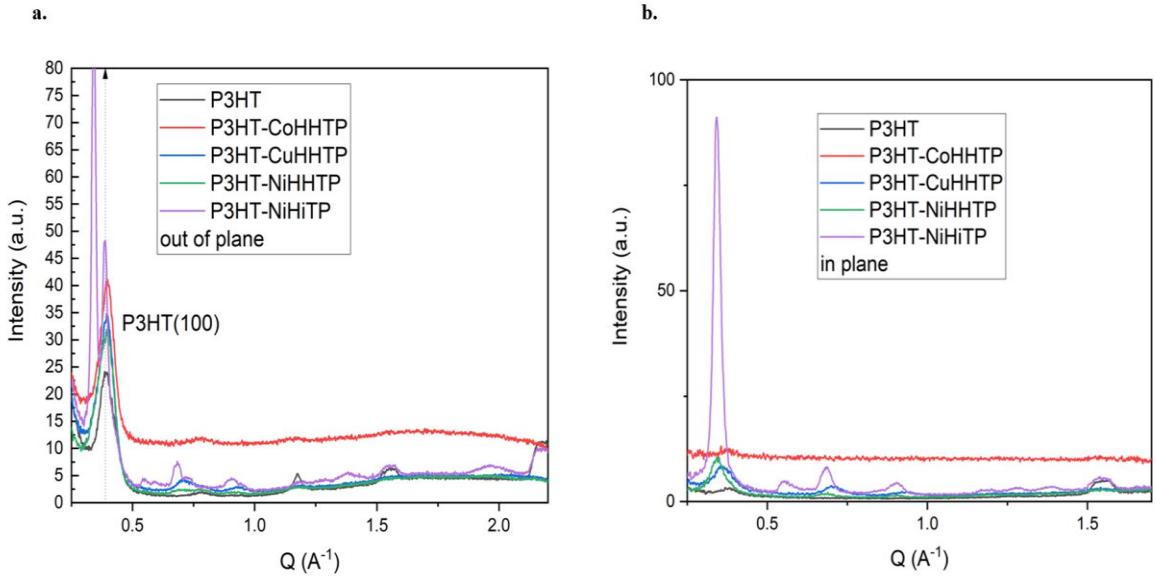

Figure 5.13 GIWAXS profiles of P3HT and P3HT–MON composite films. a,Out-of-plane GIWAXS profiles of P3HT and P3HT–MON composite films, b.In-plane GIWAXS profiles of P3HT and P3HT–MON composite films

Figure 13 shows the atomic force microscopy (AFM) height images of the thin films: a. P3HT–Ni-HITP, b.P3HT–Cu-HITP, and c. pristine P3HT. All images were collected over a 5 μm × 5 μm area.

The pristine P3HT film (Figure 5.14c) exhibits a relatively smooth and uniform surface morphology, with an average surface roughness below ~20 nm. This uniformity is characteristic of well-formed P3HT films and is beneficial for efficient interface contact and carrier transport.

In contrast, the P3HT–Ni-HITP composite (Figure 5.14a) shows increased surface roughness with several prominent aggregates and vertical features reaching heights up to ~100 nm. This suggests that Ni-HITP nanosheets are partially protruding or clustered within the polymer matrix, leading to a less uniform surface. The higher roughness may introduce interfacial barriers or local electric field variations, which can partly explain the slight reduction in EQE despite improved device performance in terms of J–V parameters.

Similarly, the P3HT–Cu-HITP film (Figure 5.14b) exhibits a moderate increase in roughness compared to pristine P3HT, with isolated bright features and clusters distributed across the surface. The height scale reaches ~80 nm, indicating that Cu-HITP also introduces notable topographical variation.

Overall, the incorporation of conductive MONs (Ni-HITP and Cu-HITP) leads to a rougher surface morphology, possibly due to phase separation or aggregation during film formation. While this does not appear to hinder overall charge extraction—given the improved J_{sc} and FF—it may contribute to non-uniform charge collection or light scattering, which could partially reduce EQE values across the spectral range.

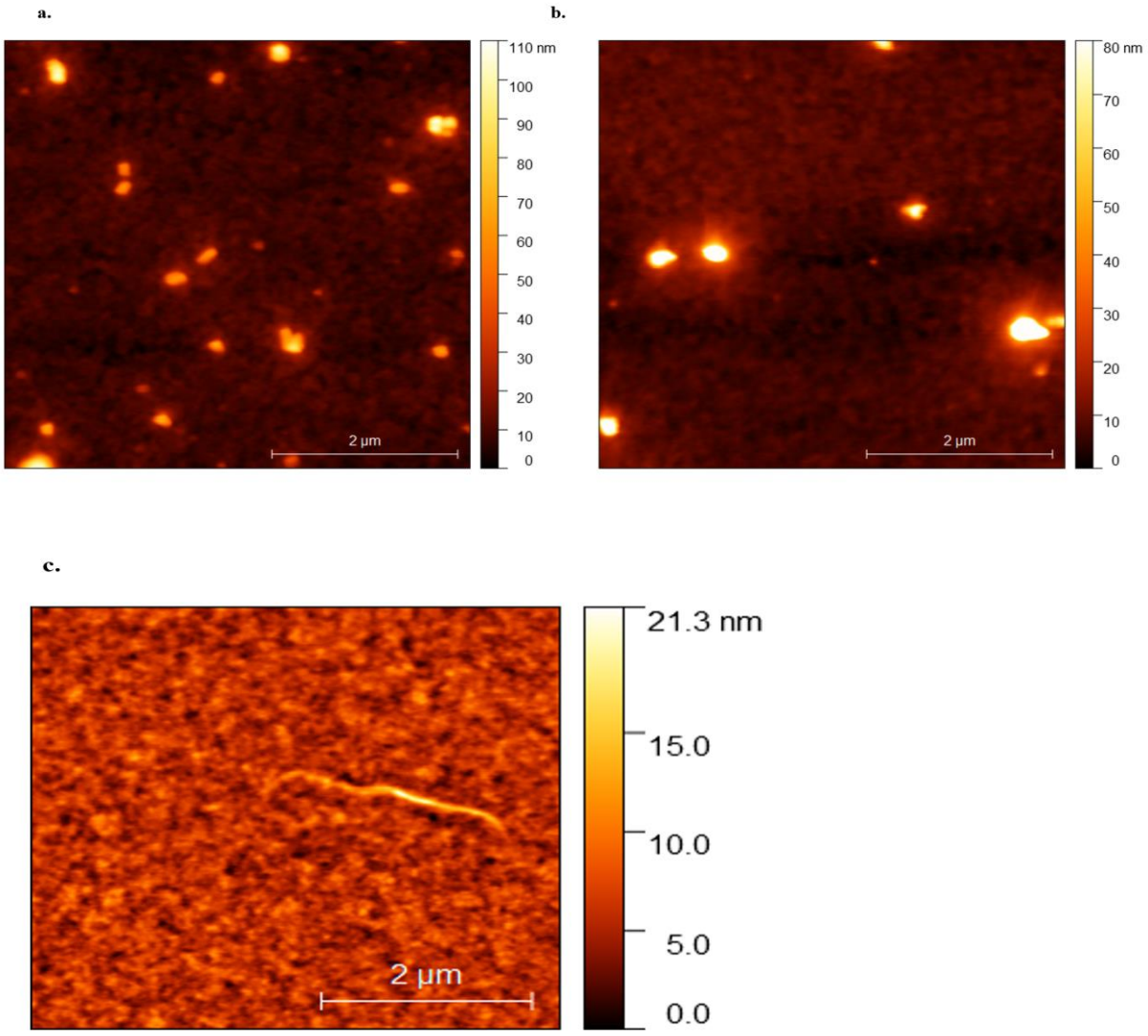

Figure 5.14 AFM of a. P3HT-Ni-HiTP, b. P3HT-CuHiTP and c. P3HT only

To investigate the impact of M-HHTP and M-HITP MON doping on the electronic structure of the HTL, ultraviolet photoelectron spectroscopy (UPS) was conducted on three different thin films: P3HT doped with M-HHTP. All films were spin-coated onto pre-cleaned ITO glass substrates using the same deposition conditions as those employed in the fabrication of photovoltaic devices, ensuring consistency and relevance of the measured electronic properties. Figure 14 presents the UPS spectra and corresponding energy level analysis. Figure 14a shows the full-range spectra for M-HHTP group, while Figure 14b and 14c highlights the low and high binding energy region used to determine the secondary electron cutoff. Figure 14d shows the full-range spectra for Ni-HITP, while Figure 14b and 14c highlights the low and high binding energy region used to determine the secondary electron cutoff. Based on these cutoff values, the HOMO levels were calculated.

$$E_{HOMO}=h\nu-(E_{cutoff}-E_{onset})$$

where $h\nu$ is the photon energy (21.22 eV for the Helium plasma source), E_{cutoff} is the secondary electron cutoff, and E_{onset} is the HOMO onset derived from the low binding energy region.

The secondary electron cutoff positions for the three films are clearly distinct. In the case of P3HT and P3HT–MONs, the onset points were accurately extracted by linear extrapolation through the steepest region of the curve. The values of the work function and HOMO levels were derived as follows:

Table 3 the HOMO energy levels of different thin films

Thin film	HOMO energy level
P3HT-NiHHTP	-6.13eV
P3HT-CuHHTP	-9.75 eV
P3HT-CoHHTP	-10.52eV

P3HT-NiHITP	-5.16eV

The HOMO energy level for P3HT–NiHHTP is calculated to be 6.13 eV, which is the closest to the Fermi level of the perovskite layer. This suggests that NiHHTP doping provides the most favorable energy alignment with the perovskite layer, facilitating efficient hole extraction at the HTL/perovskite interface.For P3HT–CuHHTP, the HOMO level is 9.75 eV, which is higher than that of NiHHTP. This implies a less favorable alignment with the perovskite layer, potentially leading to higher energy barriers for hole extraction and lower device performance. P3HT–CoHHTP (Black Curve), the HOMO energy level of P3HT–CoHHTP is calculated to be 10.52 eV, the highest among the three. This suggests that CoHHTP induces a larger energetic offset at the HTL/perovskite interface, likely hindering efficient hole extraction and leading to the lowest device efficiency.

In contrast, the P3HT–NiHITP composite exhibits a HOMO energy level of **5.16 eV**, the most optimal among all tested films. This value aligns closely with the valence band of the perovskite absorber, minimizing the interfacial energy barrier and enabling faster hole extraction and transport across HTL. Such favorable energy alignment explains the markedly improved Jsc and FF observed in NiHITP-based devices. Collectively, these results highlight that while metal–ligand combinations influence the interfacial energetics of P3HT-based composites, NiHITP provides the most efficient energy-level matching for charge transport and represents the most promising HTL configuration for high-performance PSCs.

a.

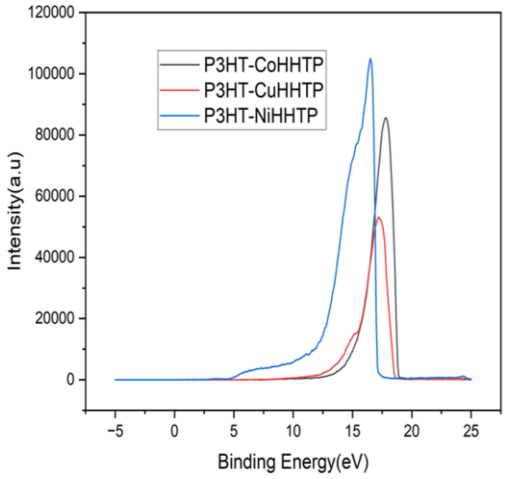
P3HT-CoHHTP
P3HT-CuHHTP
P3HT-NiHHTP
Intensity(a.u)
Binding Energy(eV)

b.

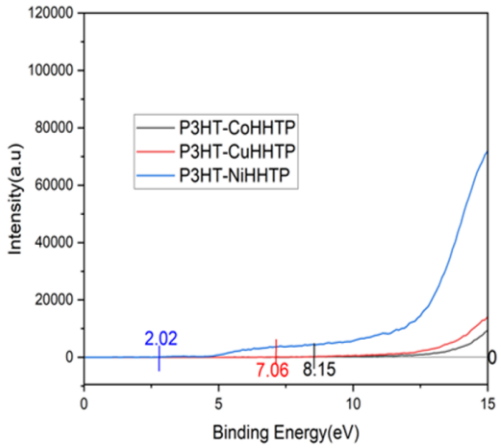
P3HT-CoHHTP
P3HT-CuHHTP
P3HT-NiHHTP
Intensity(a.u)
2.02
7.06
8.15
Binding Energy(eV)

c.

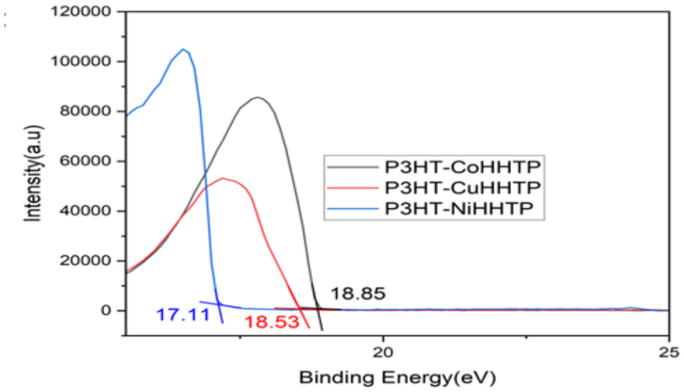
P3HT-CoHHTP
P3HT-CuHHTP
P3HT-NiHHTP
Intensity(a.u)
17.11
18.53
18.85
Binding Energy(eV)

d.

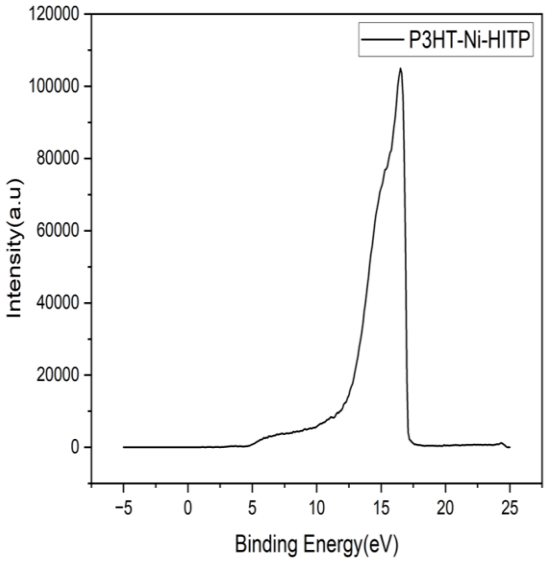
P3HT-Ni-HITP
Intensity(a.u)
Binding Energy(eV)

e.

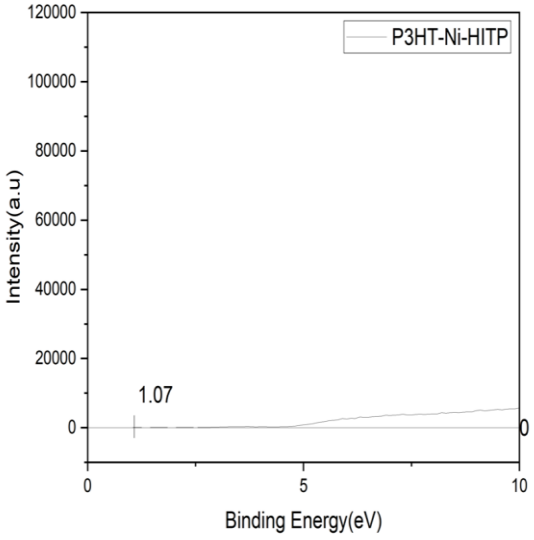
P3HT-Ni-HITP
Intensity(a.u)
1.07
Binding Energy(eV)

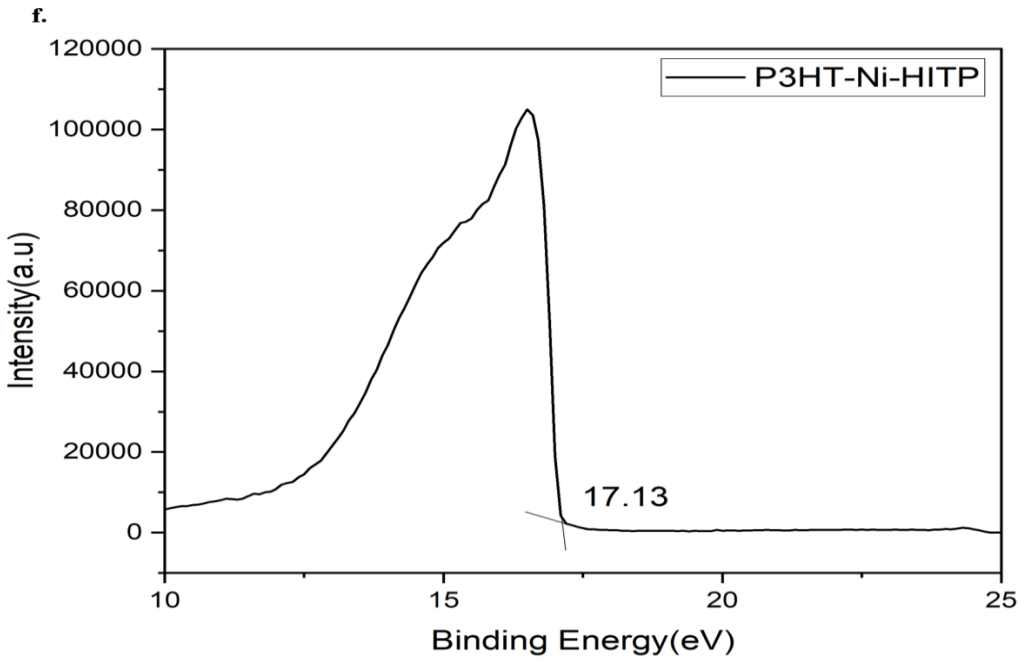

Figure 5.15 a.full UPS for P3HT-M-HHTP MONs, b.high binding energy area for P3HT-M-HHTP MONs, c. low binding energy area for P3HT-M-HHTP MONs, d.full UPS for P3HT-Ni-HITP MONs, e. high binding energy area for P3HT-Ni-HITP MONs, f. low binding energy area for P3HT-Ni-HITP MONs.

5.3 Discussion

The incorporation of 2D cMONs into the P3HT matrix has revealed a complex, yet coherent, structure–property–performance relationship in the context of HTL design for PSCs. Through a combination of optical spectroscopy, morphological characterization, and photovoltaic performance analysis, this study demonstrates that both the choice of metal center and the ligand structure within MONs play critical roles in determining interfacial behavior and overall device functionality.

PL spectroscopy clearly indicated that the inclusion of Ni–HITP led to the most pronounced quenching of P3HT emission, suggesting highly efficient exciton dissociation and interfacial charge transfer. However, the corresponding EQE spectra showed a modest reduction compared to pristine P3HT, revealing an important caveat:

PL quenching alone does not fully capture the complexity of carrier collection dynamics.

UPS measurements further clarify the role of MONs in modulating HTL energy levels. The HOMO levels of P3HT–NiHHTP (–6.13 eV) and P3HT–NiHITP (–5.16 eV) are notably shallower than those of CuHHTP (–9.75 eV) and CoHHTP (–10.52 eV), indicating that Ni-based frameworks provide the most favorable energy alignment with the perovskite valence band. This optimized alignment minimizes the interfacial barrier for hole extraction, explaining the superior Voc, FF, and overall PCE of Ni–HITP devices.

AFM imaging offers a plausible explanation, as the Ni–HITP and Cu–HITP composites both exhibited increased surface roughness, with local protrusions and morphological non-uniformity potentially inducing optical interference effects and spatially variable electric fields, which can reduce charge collection efficiency at certain wavelengths.

GIWAXS analysis provided strong evidence for enhanced molecular ordering upon MON incorporation, particularly with Ni–HITP. These composites exhibited intensified (100) lamellar peaks in both in-plane and out-of-plane directions, indicating improved vertical and lateral molecular alignment. Such ordering is widely associated with enhanced hole mobility and suppressed recombination losses, which is reflected in the significantly increased fill factor (FF) and short-circuit current density (Jsc) of the corresponding devices.

Notably, although Co–HHTP exhibited the strongest Raman-induced crystallinity improvement, its overall device performance remained inferior to Ni–HITP. This suggests that crystalline enhancement alone is insufficient; rather, optimal energy level alignment, transport channel continuity, and surface morphology must act synergistically to support effective charge extraction. The superior power conversion efficiency (PCE) of 11.25% achieved with Ni–HITP is therefore a result of finely balanced improvements across multiple domains: optical absorption, structural organization, charge transfer, and interfacial integrity.

These findings highlight the need for holistic HTL material design. While introducing highly conjugated, conductive 2D frameworks such as HITP-based MONs can indeed enhance structural order and interfacial charge separation, considerations such as nanosheet dispersion, film roughness, and vertical connectivity must also be addressed. Future efforts could further explore post-deposition treatments or interfacial modifiers to mitigate the morphological drawbacks while preserving the electronic benefits conferred by MONs.

5.4 Conclusion

This chapter demonstrates that the incorporation of 2D cMONs into the P3HT matrix represents an effective strategy to enhance hole transport and overall photovoltaic performance in PSCs. Through systematic synthesis, structural characterization, and device optimization, two families of cMONs—M–HHTP and M–HITP—were successfully synthesized and integrated as composite HTLs.

Comparative analyses revealed that HHTP-based nanosheets (Ni–, Co–, and Cu–HHTP) moderately improved device performance, primarily through enhanced molecular ordering and improved charge extraction. However, the extent of improvement remained limited by interfacial transport resistance and incomplete energetic alignment. In contrast, HITP-based nanosheets (Ni–HITP and Cu–HITP) delivered markedly superior photovoltaic parameters, achieving power conversion efficiencies exceeding 11% in champion devices. This performance enhancement arises from the synergistic effects of enhanced hole mobility, optimized energy level alignment, and increased structural order within the P3HT framework, as confirmed by PL, GIWAXS, and AFM analyses.

Mechanistically, Ni–HITP demonstrated the strongest influence on film morphology and molecular orientation, promoting both lamellar stacking and face-on alignment of P3HT chains—configurations known to facilitate vertical charge transport and minimize recombination losses. The pronounced PL quenching and improved fill factor

further underscore the efficiency of interfacial charge transfer in HITP-based systems. Nevertheless, AFM observations suggest that the increased surface roughness induced by MON incorporation could partially offset optical gains, emphasizing the need for morphological control in future device engineering.

Overall, these findings establish HITP-based 2D cMONs, particularly Ni–HITP, as highly promising candidates for next-generation dopant-free HTLs in perovskite photovoltaics. Beyond their role as conductive additives, these nanosheets act as structural modulators that simultaneously improve charge transport, crystalline, and interfacial coupling. Future research should focus on optimizing nanosheet dispersion and interfacial engineering to fully exploit the intrinsic conductivity and tunable chemistry of 2D cMONs, thereby advancing their integration into scalable, high-efficiency perovskite solar cell architectures.

5.5 Materials and Methods Precursor materials preparation

Materials and analysed according to methods outlined in chapter 3

Hexa-hydroxytriphenylene(HHTP) Hexaiminotriphenylene(HITP) were both got from fisher UK. M (where M=Ni, Co, and Cu) acetate was obtained from Sigma-Aldrich. Sodium acetate (NaOAC) was got from sigma-Aldrich.

Synthesis and physical characterization of M-HHTP and M-HITP MONs

Synthesis of HHTP group MONs

M-HHTP (where M=Ni, Co, and Cu) nanosheets were synthesized using a method adapted from song et al. [9]

A solid mixture of M (where M=Ni, Co, and Cu) acetate (16 mg) and HHTP (13 mg) were mixed in 2 mL water/N, N-dimethylformamide (DMF) (v/v = 1:1) and sonicated

for 5 min. Then, the vial was sealed and heated at 85 °C in an oven for 24 h, followed by natural cooling to room temperature. The solid product was centrifuged at 10000 RPM for one hour. Washed with water and acetone three times respectively. The solid materials were then dried with air follow overnight.

Synthesis of HITP group MONs

M-HITP (where M=Ni, Cu) nanosheets were synthesized using a method adapted from Song et al as well.[9]A solid mixture of M (where M=Ni, and Cu) acetate (42 mg) and HITP•6HCl (where HITP= 2,3,6,7,10,11-hexaaminotriphenylene) (60 mg) in 72 ml DMF/DMA (v/v = 1:1) was preheated to 65℃. Followed by the addition of 48 ml of NaOAC (2 mol/mL) and 18 ml of H_2O. The reaction mixture was then heated at 65 °C while stirring for 24 hours under reflux. The resulting solution was centrifuged (4500 rpm for 10 minutes), and the supernatant was discarded. Washing of the resulting solid pellet followed using ethanol (x3 10 ml)

Fabrication of PSCS according to methods outlined in chapter 3

Reference

1. M. Wang, R. Dong and X. Feng, *Chem. Soc. Rev.*, 2021, 50, 2764–2793.
2. M. G. Campbell, D. Sheberla, S. F. Liu, T. M. Swager and M. Dincă, *Angew. Chem., Int. Ed.*, 2015, 54, 4349–4352.
3. L. S. Xie, G. Skorupskii and M. Dincă, *Chem. Rev.*, 2020, 120, 8536–8580.
4. H. T. Pham, J. Y. Choi, X. Fang, A. Claman, S. Huang, S. Coates, L. Wayment, W. Zhang and J. Park, *Chem.*, 2024, 10, 199–210.
5. H. Yang, Y. Liu, M. Wang, Z. Zhang, Y. C. Zheng, X. B. Li, L. Z. Wu, X. Feng and H. Wang, *Angew. Chem., Int. Ed.*, 2025, 64, e202422382.
6. J. Liu, Y. Chen, X. Feng and R. Dong, *Small Struct.*, 2022, 3, 2100210.
7. R. Wang, W. Yu, C. Sun, K. Chiranjeevulu, S. Deng, J. Wu, F. Yan, C. Peng, Y. Lou, G. Xu and G. Zou, *Nanoscale Res. Lett.*, 2022, 17, 6
8. J. Cao, C. K. Liu, V. Piradi, H. L. Loi, T. Wang, H. Cheng, X. Zhu and F. Yan, *ACS Energy Lett.*, 2022, **7**, 3362–3369.
9. X. Song, X. Wang, Y. Li, C. Zheng, B. Zhang, C. A. Di, F. Li, C. Jin, W. Mi, L. Chen and W. Hu, *Angew. Chem., Int. Ed.*, 2020, 59, 1118–1123.
10. M. G. Campbell, D. Sheberla, S. F. Liu, T. M. Swager and M. Dincă, *Angew. Chem., Int. Ed.*, 2015, 54, 4349–4352.
11. F. Cheng, R. He, S. Nie, C. Zhang, J. Yin, J. Li, N. Zheng and B. Wu, *J. Am. Chem. Soc.*, 2021, 143, 5855–5866

Supporting information

To evaluate the impact of metal core and organic linker on the hole transport properties of (PSCs, devices were fabricated using P3HT blended with HHTP and HITP organic linker as the HTL. Two blend weight ratios were investigated: 1:0.5(P3HT: Organic linker).

Statistical Device Performance

Figures S5.1 and S5.2 show the statistical distribution of the main PV parameters for P3HT-Organic linker devices.

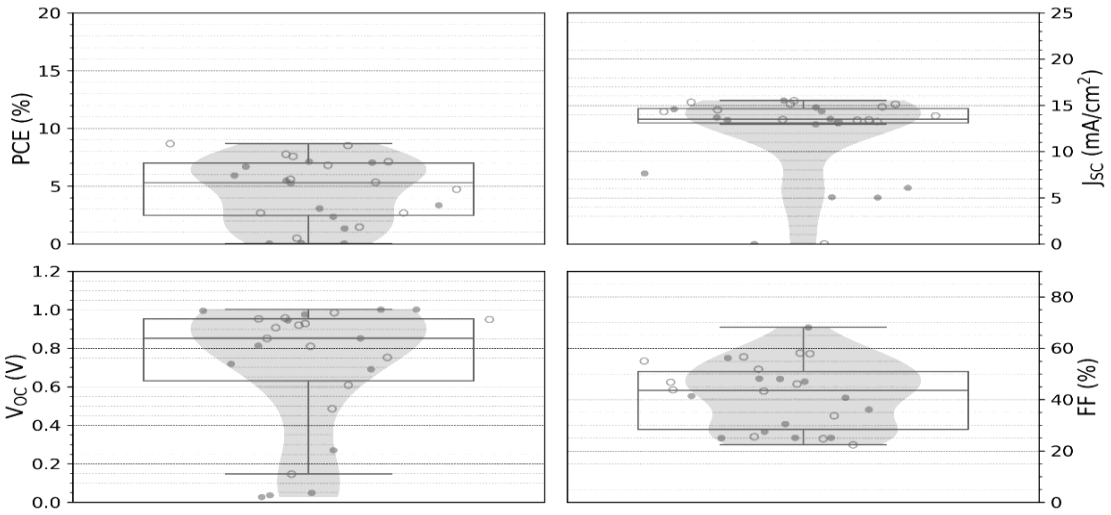

Figure S5.1 PV parameters of P3HT-HHTP Devices

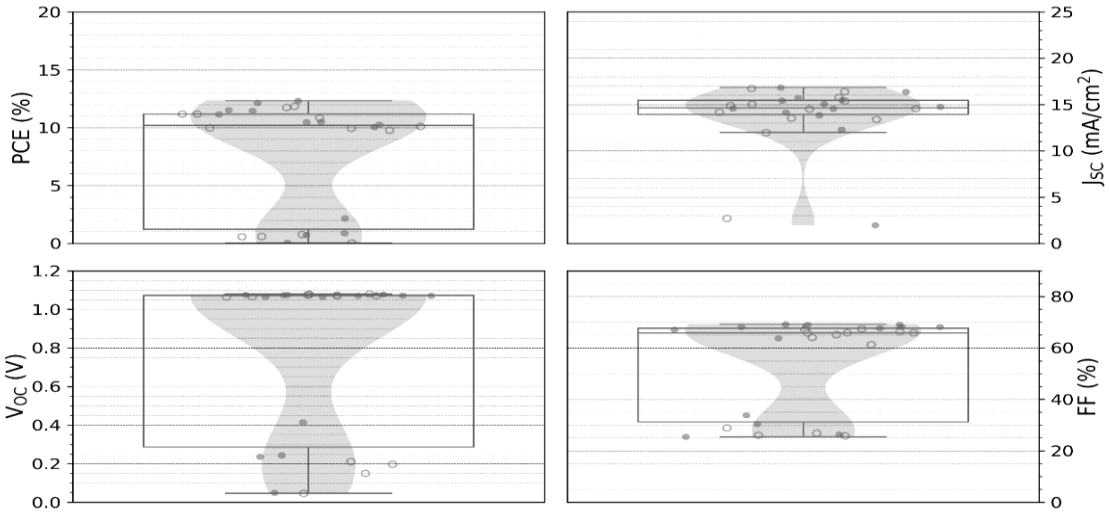

Figure S5.2 PV parameters of P3HT-HiTP Devices

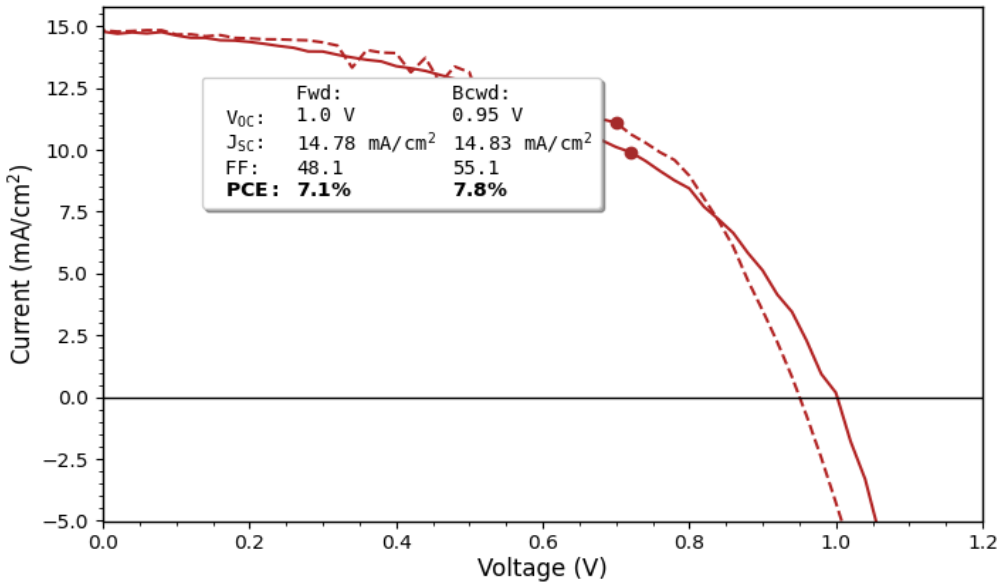

Figure S5.3 PV parameters of P3HT-HHTP Devices

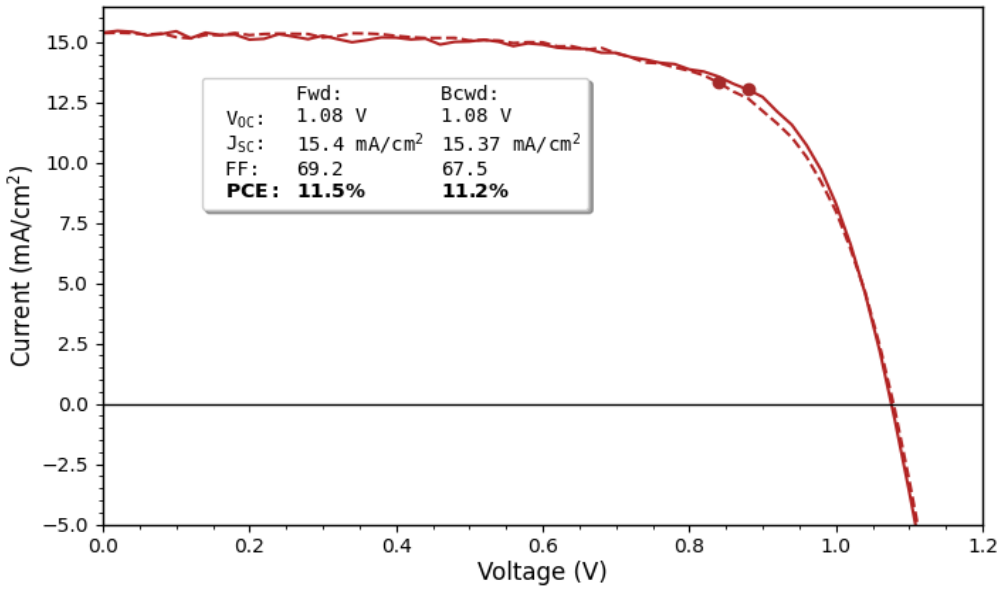

Figure S5.4 Champion Device of P3HT-HITP Devices

Chapter 6 Conclusion and Further works

The application of metal–organic nanosheets (MONs) in perovskite solar cells (PSCs) has been systematically investigated in this thesis, focusing on their role as modifiers within the hole transport layers (HTLs). By combining structural, optical, electronic, and photovoltaic characterizations, this work demonstrates that MONs are versatile interfacial materials capable of simultaneously enhancing film morphology, tuning energy-level alignment, and facilitating charge extraction. The major contributions of each chapter are summarized below.

Chapter 3 investigates the incorporation of Zn_2(ZnTCPP) MONs into P3HT thin films, providing the first systematic analysis of their contributions as HTLs in PSCs. Optical absorption spectroscopy revealed the emergence of additional absorption features derived from the porphyrin ligand, expanding the effective light-harvesting window of the films. Photoluminescence (PL) spectroscopy showed pronounced quenching of the P3HT emission, indicative of strong electronic interactions between the nanosheets and the polymer, as well as the opening of new non-radiative decay pathways that favor charge transfer.

Morphological analyses using AFM and SEM revealed that the incorporation of Zn_2(ZnTCPP) reduced surface roughness and promoted the formation of more uniform films. GIWAXS studies further confirmed enhanced crystallinity and preferential molecular orientation of P3HT chains, suggesting that Zn_2(ZnTCPP) acted as a structural template, guiding polymer packing and reducing energetic disorder. These changes translated into improved charge extraction and transport, resulting in? enhanced photovoltaic device efficiency. Overall, the results of Chapter 3 indicate that Zn_2(ZnTCPP) MONs can serve as effective HTL modifiers, where their incorporation into P3HT composites extends short-wavelength absorption, promotes exciton dissociation, and improves film morphology and molecular ordering.

This chapter therefore provides the first systematic demonstration of employing

MONs as HTL additives in PSCs.

Chapter 4 extended the study by investigating the role of metal nodes within MONs through the synthesis of Cu_2(CuTCPP) and Zn–Pd(TCPP) nanosheets. The rationale was to exploit the modularity of MONs, where substituting metal centers could tune crystalline, morphology, and energy-level alignment. AFM and SEM analyses demonstrated that these MONs significantly altered surface morphology, with Cu_2(CuTCPP) producing smoother films, while Zn–Pd(TCPP) yielded films with more heterogeneous grain structures.

GIWAXS studies revealed pronounced differences in molecular packing, with Cu_2(CuTCPP) enhancing π–π stacking interactions relative to Zn–Pd-TCPP, which showed more disordered orientation. UPS measurements confirmed that while the changes in ionization energy across these MONs were relatively modest, variations in hole injection barriers and interface energetics were sufficient to influence device-level charge transfer processes. Importantly, Photovoltaic testing indicated that nanosheet crystalline and ordering significantly influenced PCE, with more crystalline nanosheets facilitating efficient charge transport, while less ordered ones hindered interfacial contact.

This chapter demonstrated that careful selection of metal nodes within MONs directly affects the nanoscale ordering and charge dynamics in hybrid films, underlining the structural dependence of charge transport pathways. These findings highlight the flexibility of MONs as a platform where structural chemistry can be tailored for targeted photovoltaic functions.

Chapter 5 explored conductive 2D conductive metal–organic frameworks (cMONs) as an alternative to conventional MONs. Unlike porphyrin MONs, which primarily contribute to absorption and templating, cMONs feature intrinsic electrical conductivity due to extended π–d conjugation and delocalized charge transport pathways. UPS measurements confirmed favorable HOMO alignment with P3HT,

reducing the energetic barrier for hole injection.

Electrical characterizations through J–V curves and EQE spectra revealed that devices incorporating cMONs exhibited higher short-circuit currents and fill factors, attributable to enhanced hole mobility and suppressed recombination. Morphological analyses further demonstrated that cMONs were more compatible with P3HT matrices, leading to uniform film formation and reduced trap density. Collectively, these results suggest that cMONs not only alleviate transport bottlenecks but also represent a promising route toward more efficient charge extraction layers in PSCs.

This work highlights that conductive MON-like frameworks can serve as intermediates between semi-crystalline polymer layers and high-mobility inorganic transport materials, thereby offering new opportunities for HTL design. By integrating structural templating, favorable energy-level alignment, and intrinsic conductivity, cMONs provide a promising pathway toward the rational optimization of interlayers in PSCs.

Future Work and Outlook

While this thesis has demonstrated the potential of porphyrin-based MONs and conductive 2D frameworks as effective additives for polymeric HTLs in PSCs, several important research directions remain to be explored to consolidate and extend these findings.

Device operational stability

One of the most critical challenges for PSCs lies in their long-term operational stability. Although the incorporation of MONs into HTLs has been shown here to improve structural ordering and charge transport, their influence on degradation pathways under realistic conditions remains unclear. Prolonged exposure to continuous illumination, thermal stress, and humidity often leads to ion migration, interfacial reactions, and the growth of trap states, all of which limit device lifetimes.[1] Future work should therefore investigate whether MON-based HTLs can mitigate or

exacerbate such effects. Accelerated aging tests under standard International Summit on Organic Photovoltaic Stability (ISOS) protocols,[2] combined with in situ characterization techniques such as TRPL, which can probe carrier lifetimes and interfacial charge-transfer dynamics, and Kelvin probe microscopy, which can map surface potentials and energy-level alignment, these studies could provide valuable insights into how MONs influence bulk morphology evolution and interfacial energetics over time. Establishing a clear correlation between MON-induced ordering and long-term device reliability will be crucial for assessing their suitability in commercial applications.

Design of next-generation MONs

The modular nature of MONs provides an attractive platform for tailoring their properties beyond the porphyrin-based systems studied in this work. While Zn_2(ZnTCPP), Cu_2(CuTCPP), and Zn–Pd-TCPP have revealed the structural and electronic tunability of this class of materials, further optimization is needed to achieve broader spectral absorption, improved charge mobility, and better energy-level alignment with perovskite absorbers. For example, phthalocyanine-based MONs could extend absorption into the near-infrared region, thereby harvesting a larger fraction of the solar spectrum.[3] Similarly, thiolate-bridged conductive MONs may provide intrinsically higher hole mobility due to extended π–d conjugation.[4] Future studies should also consider systematic variation of metal nodes, mixed-metal strategies, and chemical functionalization of ligands to optimize solubility, crystallinity, and interfacial compatibility. While computational screening in combination with experimental validation could, in principle, accelerate the discovery of high-performing MON architectures for HTLs, accurately modeling solubility, crystallinity, and interfacial compatibility remains challenging and would require substantial methodological development.

Integration into advanced PSC architectures.

The present study employed P3HT as a model polymer to establish fundamental

insights into MON–polymer interactions. While this represents a limitation compared with the high-performance HTLs used in state-of-the-art PSCs, preliminary tests with PTAA and Spiro-OMeTAD confirmed that MONs did not provide noticeable improvements in these systems. This contrast highlights that the beneficial effects of MONs are closely associated with the semi-crystalline nature of P3HT, where molecular ordering and morphology can be more effectively modulated. Accordingly, P3HT served as a suitable model system for elucidating the underlying structure–property relationships, providing design principles that may inform the development of next-generation HTLs.

Looking ahead, it would be important to evaluate the efficacy of MONs in more advanced HTL systems to validate their broader relevance. In tandem solar cells, for example, MON-based materials could potentially function as intermediate recombination layers, where their balance of charge selectivity and optical compatibility may offer advantages.[5] Likewise, in 2D/3D perovskite heterostructures, ultrathin MONs may serve as templates to guide perovskite crystallization and lattice orientation, thereby reducing defect densities and extending carrier lifetimes. Furthermore, exploring scalable deposition methods such as slot-die coating, blade coating, or inkjet printing remains a key step toward assessing the compatibility of MONs with large-area fabrication.

Application expansion

Beyond PSCs, the insights gained from this thesis open opportunities for applying MONs in other organic and hybrid optoelectronic devices. The ability of MONs to enhance crystallinity and charge transport in semi-crystalline polymers suggests that they could be beneficial in organic field-effect transistors (OFETs) and organic light-emitting diodes (OLEDs), where efficient charge injection and transport are equally critical.[6] In OFETs, MONs may promote polymer alignment and improve field-effect mobility, while in OLEDs, they could assist in balancing charge injection and suppressing non-radiative recombination pathways. [7,8]Exploring such cross-device

applications would not only broaden the technological relevance of MONs but also position them as a general class of multifunctional interfacial materials for the wider field of organic and hybrid electronics.

Overall outlook

Taken together, the future development of MON-based HTLs will hinge on three key aspects: verifying their ability to improve device stability under realistic operating conditions, expanding their structural and electronic diversity through rational molecular design, and validating their compatibility with high-efficiency PSC architectures and large-scale fabrication. By addressing these challenges, MONs and conductive cMONs could evolve from promising laboratory additives into robust, scalable, and versatile interfacial solutions for next-generation photovoltaics. Their intrinsic tunability, nanoscale thickness, and chemical flexibility also make them attractive candidates for broader applications in organic electronics, thereby ensuring that the research directions opened by this thesis will remain rich and impactful in the years to come.

Reference

1. D. Zhang, D. Li, Y. Hu, A. Mei and H. Han, *Commun. Mater.*, 2022, *3*, 58.
2. P. Holzhey and M. Saliba, *J. Mater. Chem. A*, 2018, *6*, 21794–21808.
3. M. Kato, H. Yoshizawa, M. Nakaya, Y. Kitagawa, K. Okamoto, T. Yamada, M. Yoshino, K. Tanaka and J. Onoe, *Sci. Rep.*, 2022, *12*, 8810.
4. E. M. Johnson, S. Ilic and A. J. Morris, *ACS Cent. Sci.*, 2021, *7*, 445–453.
5. Y. Lin, W. Yang, H. Gu, F. Du, J. Liao, D. Yu, J. Xia, H. Wang, S. Yang, G. Fang and C. Liang, *Adv. Mater.*, 2024, *36*, 2405684.
6. W. Zhao, J. Peng, W. Wang, S. Liu, Q. Zhao and W. Huang, *Coord. Chem. Rev.*, 2018, *377*, 44–63.
7. D. Khim, A. Luzio, G. E. Bonacchini, G. Pace, M. J. Lee, Y. Y. Noh and M. Caironi, *Adv. Mater.*, 2018, *30*, 1705463.
8. C. Kaiyasuan, V. Somjit, B. Boekfa, D. Packwood, P. Chasing, T. Sudyoadsuk, K. Kongpatpanich and V. Promarak, *Angew. Chem., Int. Ed.*, 2022, *61*, e202117608.